

**THIN-FILM PIEZOELECTRIC-ON-SUBSTRATE RESONATORS  
AND NARROWBAND FILTERS**

A Thesis  
Presented to  
The Academic Faculty

by

Reza Abdolvand

In Partial Fulfillment  
of the Requirements for the Degree  
of Doctor of Philosophy in the  
School of Electrical and Computer Engineering

Georgia Institute of Technology  
April 2008

**THIN-FILM PIEZOELECTRIC-ON-SUBSTRATE RESONATORS  
AND NARROWBAND FILTERS**

Approved by:

Dr. Farrokh Ayazi, Advisor  
School of Electrical and Computer  
Engineering  
*Georgia Institute of Technology*

Dr. Oliver Brand  
School of Electrical and Computer  
Engineering  
*Georgia Institute of Technology*

Dr. John D. Cressler  
School of Electrical and Computer  
Engineering  
*Georgia Institute of Technology*

Dr. James D. Meindl  
School of Electrical and Computer  
Engineering  
*Georgia Institute of Technology*

Dr. Nazanin Bassiri-Gharb  
George W. Woodruff School of  
Mechanical Engineering  
*Georgia Institute of Technology*

Date Approved: Nov. 26, 2007

To my lovely wife Nazanin  
and my family

## ACKNOWLEDGEMENTS

This work closes a chapter in my life which has been a joyful learning and exploring experience. This journey would not be possible without the support, help and encouragement of so many people whom I feel indebted to forever.

First and foremost, I sincerely express my gratitude to my advisor, Professor Farrokh Ayazi. I feel very fortunate to have the opportunity of working under his supervision, and I thank him a lot for his support and guidance throughout my PhD. He has been a great mentor in my research and a role model for hard work and dedication. I learned from him what it takes to be a successful scholar and I will always look up to him and admire him for having such a passion for excellence.

I would like to extend my special thanks to Professor Oliver Brand and Professor John D. Cressler, whom I have learnt a lot from their extensive knowledge and distinctive personality. I would also like to thank my other dissertation committee members: Professor James D. Meindl, and Professor Nazanin Bassiri-Gharb for their valuable time and input in enabling successful completion of this dissertation. I thank all of these outstanding professors for their inspiration, support, and guidance on my thesis.

I have greatly benefited from the help of many of my colleagues. I wish to thank all former and present members of the Integrated MEMS laboratory whose support and cooperation has been instrumental to the progress of this work during the past 5 years. Special thank is due to Gavin K. Ho for contributing in the design and the concept development of many of devices presented in this work. Special thank is also due to Siavash Pourkamali whose genius and insight have always inspired me to look for a way to improve my work. This work would not be completed without the help and support of

all my friends specially Pejman Monajemi, Babak Vakili Amini, Houri Johari, Hossein Mirilavasani and Faisal Zaman, whom I have been privileged to work with.

I would also like to extend my gratitude to the staff at the Microelectronic Research Center, who organize a well-maintained and highly-equipped micro-fabrication facility. I wish to specially thank Gary Spinner who is continuously and enthusiastically ready to provide cleanroom users with his help and technical support.

I would like to thank my dear mom and dad, Shirin and Taghi, and my brother, Ali, who have been a great emotional support for me from miles away. They are the people who have shaped me as a person that I am, and never stopped encouraging me through ups and downs.

Last but definitely not least, I thank my dearest wife, Nazanin. She is my whole life and as graceful as can be. I owe her for every bit of success I have had from the moment that she came into my life. She is the most important motivation for me to move forward and to be a better person each day passes by. Endless thank to her and her family (mom, dad and Asal).

# TABLE OF CONTENTS

	Page
ACKNOWLEDGEMENTS .....	iv
LIST OF TABLES .....	x
LIST OF FIGURES .....	xi
SUMMARY .....	xvi
CHAPTER 1: INTRODUCTION .....	1
CHAPTER 2: BACKGROUND .....	4
2.1 Capacitive Micro-Resonators.....	5
2.2 Piezoelectric Micro-Resonators .....	6
2.2.1 Piezoelectricity: Principles and Early Application .....	7
2.2.2 Piezoelectricity: Formulation.....	8
2.2.3 Piezoelectric Resonators .....	9
2.3 Resonator Mechanical Modeling .....	11
2.4 Resonator Equivalent Electrical Model .....	12
2.4.1 One-Port Piezoelectric Resonator Electrical Model .....	13
2.4.2 Two-Port Piezoelectric Resonator Electrical Model.....	15
2.5 MEM Coupled-Resonator Filters.....	16
CHAPTER 3: THIN-FILM PIEZOELECTRIC-ON-SUBSTRATE TECHNOLOGY	19
3.1 TPoS Resonator Structure.....	19
3.1.1 Why Piezoelectric on Substrate? .....	20
3.1.2 Power Handling in Piezoelectric Resonators .....	21
3.1.3 Quality Factor in Piezoelectric Resonators.....	23
3.2 Lateral versus Thickness Resonance Modes.....	25

3.3 Lumped Element Electrical Model of Lateral-Extensional TPoS Resonators.....	26
CHAPTER 4: FABRICATION PROCESS.....	29
4.1 Process Flow on SOI.....	29
4.1.1 Bottom Metal Layer Deposition.....	30
4.1.2 ZnO Sputtering.....	32
4.1.3 Top Electrode Layer Deposition.....	36
4.1.4 Bottom Electrode Access Etching.....	37
4.1.5 Device Structure Etching.....	37
4.1.6 Back-Side Etching.....	38
4.2 Effective Coupling Factor.....	39
CHAPTER 5: THIN-FILM PIEZOELECTRIC-ON-SUBSTRATE OSCILLATORS...	41
5.1 Introduction.....	41
5.2 Resonator Design.....	43
5.2.1 High-Order Design.....	43
5.2.2 Arrayed Design.....	44
5.3 Frequency Response Measurement.....	45
5.3.1 High-Order versus Arrayed Design.....	45
5.3.2 Temperature-Stable Resonators.....	48
5.3.3 AlN-on-Silicon Resonators.....	49
5.4 Linearity Measurement.....	51
5.5 Oscillator Design.....	53
5.6 Dual mode Oscillator.....	57
5.6.1 Operation Principle.....	57
5.6.2 Implementation and Characterization.....	59
5.6.3 Oscillator Circuit.....	61

5.7 Conclusion.....	63
CHAPTER 6: THIN-FILM PIEZOELECTRIC-ON-SUBSTRATE MONOLITHIC FILTERS .....	65
6.1 Introduction .....	65
6.2 Design Principles.....	68
6.2.1 Lateral Mode .....	70
6.2.2 Thickness Mode .....	72
6.3 Equivalent Electrical Model.....	75
6.4 Implementation and Results .....	78
6.5 Conclusion.....	82
CHAPTER 7: THIN-FILM PIEZOELECTRIC-ON-DIAMOND RESONATORS AND FILTERS.....	83
7.1 Introduction .....	83
7.2 Process Development .....	86
7.2.1 Process Flow.....	86
7.2.2 ZnO Sputtering.....	87
7.3 Resonator Design and Fabrication .....	89
7.4 Effect of Oxide .....	90
7.5 TPoD Resonator Measurement Results.....	91
7.6 Monolithic TPoD Filters .....	93
7.7 ZnO-on-Diamond Resonant Mass Sensors .....	98
7.6.1 Simulation Results.....	99
7.6.2 Experimental Results.....	100
7.8 Conclusion.....	103
CHAPTER 8: CONCLUSION AND FUTURE DIRECTION.....	104
8.1 High-Frequency TPoS Resonators on SOI.....	104



8.2 Monolithic TPoS Filters .....	105
8.3 Thin-Film Piezoelectric-on-Diamond Devices .....	106
8.4 Future Research .....	106
REFERENCES .....	109
VITA .....	119

## LIST OF TABLES

	Page
Table 4.1: List of parameters that are kept constant in all experiments regarding characterization of ZnO sputtering .....	32
Table 6.1: Component values in the electrical model of Fig. 6.8b used for simulation ..	80
Table 6.2: BW of thickness-mode filters with identical resonant structure and different number of fingers.....	82
Table 7.1: Summary of the measured resonance frequency and the quality factor for TPoS and TPoD resonators with various finger pitches .....	92

## LIST OF FIGURES

	Page
Figure 2.1: A simple stack of a piezoelectric substrate and metallic electrodes.....	9
Figure 2.2: The schematic representation of the electric field and the corresponding strain field in a thickness mode piezoelectric resonator .....	10
Figure 2.3: The schematic viewgraph of a lateral-extensional mode piezoelectric resonator .....	11
Figure 2.4: A mass-spring-damper representation of a mechanical resonator.....	11
Figure 2.5: An RLC equivalent circuit for a mechanical resonator .....	13
Figure 2.6: A simple electrical model for an electromechanical piezoelectric resonator ..	14
Figure 2.7: The BVD electrical representation for a one-port piezoelectric resonator.....	14
Figure 2.8: The schematic viewgraph of a two-port piezoelectric resonator.....	15
Figure 2.9: The electrical equivalent model of a two-port piezoelectric resonator .....	15
Figure 2.10: Simplified electrical model of a two-port piezoelectric resonator .....	16
Figure 3.1: The schematic view graph of a one-port TPoS resonant structure.....	19
Figure 3.2: A frequency response plot of a resonator operating at bifurcation .....	23
Figure 3.3: The representation of the current divided between the two motional and feedthrough branches in a resonator model.....	28
Figure 4.1: The schematic process flow for fabrication of TPoS devices on SOI.....	29
Figure 4.2: XRD 2 $\theta$ curves measured from ZnO samples sputtered on different metal layers.....	34
Figure 4.3: XRD 2 $\theta$ curve measured from ZnO sample sputtered on oxide-covered Pt ...	35
Figure 4.4: XRD rocking curve measured from ZnO samples sputtered on oxide-covered Pt.....	35
Figure 4.5: XRD rocking curves measured from ZnO samples sputtered on gold and Ti-covered gold layers.....	36
Figure 4.6: Overlapped simulated (red-line) and measured (blue-line) frequency response of from 94.5MHz ZnO-on-Silicon resonator.....	40

Figure 5.1: Schematic viewgraphs of (a) a third-order and (b) a two-resonator coupled array TPoS resonator .....	44
Figure 5.2: The third-order lateral extensional resonance mode-shape of a block resonator simulated in FEMLAB .....	45
Figure 5.3: Optical viewgraphs of (a) a third-order and (b) four-resonator coupled array TPoS resonators.....	46
Figure 5.4: The frequency response plot of a third-order TPoS resonator .....	46
Figure 5.5: The wide-span (100MHz) frequency response and the SEM of a 12-resonator coupled array .....	47
Figure 5.6: Frequency response plots of 4, 6, and 12-resonator coupled arrays.....	47
Figure 5.7: The frequency response of a temperature-compensated 12-resonator coupled array .....	48
Figure 5.8: The frequency response and the SEM picture of a third-order AlN-on-silicon resonator .....	49
Figure 5.9: The frequency response of the third-order resonator in fundamental mode; a) in air b) in vacuum.....	50
Figure 5.10: The SEM and the frequency response of a 9 <sup>th</sup> -order AlN-on-silicon resonator with a 20 $\mu$ m finger pitch.....	50
Figure 5.11: The SEM and the frequency response of a high-order 500Mhz AlN-on-silicon resonator .....	51
Figure 5.12: The nonlinearity measurement for a) third-order TPoS resonator and b) 12-resonator coupled array TPoS resonator .....	52
Figure 5.13: The nonlinearity measurement for an AlN-on-silicon resonator a) before, and b) after etching the structural silicon.....	52
Figure 5.14: The schematic circuit diagram and output waveform of the single-transistor oscillator.....	54
Figure 5.15: The measured phase-noise of the coupled-array temperature-stable oscillator.....	54
Figure 5.16: The measured TCF plot of the temperature-stable TPoS oscillator .....	55
Figure 5.17: The schematic diagram of the designed CMOS TIA and the phase noise plots measured from the oscillators based on the single transistor and the CMOS amplifiers .....	56

Figure 5.18: The measured phase-noise of the 208MHz oscillator .....	56
Figure 5.19: Width-extensional resonance mode-shapes of a rectangular silicon plate simulated in FEMLAB; a) third-order b) first-order.....	58
Figure 5.20: The block diagram of the architecture used to implement the dual-frequency oscillator .....	59
Figure 5.21: The first and the third-order frequency response of the resonator shown in the SEM of Fig. 5.8.....	59
Figure 5.22: The first- and the third-order frequency response of the resonator (Fig. 5.8) in vacuum.....	60
Figure 5.23: The percentage normalized frequency change with temperature for the two resonance modes. The TCF values are $-33\text{ppm}/^\circ\text{C}$ and $-28\text{ppm}/^\circ\text{C}$ .....	60
Figure 5.24: The schematic circuit of the dual-frequency oscillator .....	61
Figure 5.25: The measured waveform and phase noise for the 35MHz oscillation frequency in air and in vacuum.....	62
Figure 5.26: The measured waveform and phase noise for the 105.7MHz oscillation frequency in air .....	63
Figure 6.1: The schematic diagram of a monolithic TPoS filter.....	68
Figure 6.2: Simulated dual fundamental width-extensional resonance mode-shapes of a $40\mu\text{m}$ wide silicon plate a) symmetric and b) asymmetric.....	71
Figure 6.3: Simulated dual third-order width extensional resonance mode-shapes of a $160\mu\text{m}$ wide silicon plate and the schematic viewgraph of the suggested electrode pattern .....	72
Figure 6.4: Simulated first-order dual thickness resonance mode-shapes of a silicon plate in 2D .....	73
Figure 6.5: The schematic viewgraph of interdigitated electrode pattern for monolithic thickness mode TPoS filters .....	73
Figure 6.6: Simulated thickness resonance mode-shapes of a silicon plate in 2D with three strain-alternating sections.....	74
Figure 6.7: The schematic equivalent electrical model for second-order mechanically-coupled resonator filters and a typical corresponding frequency response....	75
Figure 6.8: Alternative equivalent electrical models for second-order mechanically-coupled resonator filters a) with transformer b) with coupling inductor, and c) a typical corresponding frequency response.....	77

Figure 6.9: The measured frequency response and SEM picture of a lateral TPoS filter at 440MHz .....	79
Figure 6.10: The SEM picture of a lateral TPoS filters with 10 $\mu$ m finger pitch and frequency response for two devices; a) 50 $\mu$ m long and b) 35 $\mu$ m long .....	79
Figure 6.11: The optical micrograph and the frequency response of a 915MHz lateral monolithic TPoS filter .....	80
Figure 6.12: Measured frequency response plots and the SEM picture of 3.5 GHz thickness mode monolithic TPoS filters .....	81
Figure 6.13: Measured frequency response plots and optical viewgraphs of two thickness mode monolithic TPoS filters with different number of fingers...82	82
Figure 7.1: Schematic process flow for the fabrication of TPoD resonators; a) stack development b) etch and release .....	86
Figure 7.2: SEM pictures comparing the morphology of sputtered ZnO a) directly on NC diamond and b) on polished oxide coated NC diamond .....	88
Figure 7.3: XRD 2 $\theta$ plots measured from ZnO sputtered samples on different substrates with various sputtering parameters .....	89
Figure 7.4: a) The SEM of a fabricated TPoD resonator; and b) the cross-sectional view of the etched composite stack.....	90
Figure 7.5: Width-extensional resonance mode-shapes of a 5 $\mu$ m wide structure comprising a) diamond, oxide and ZnO layers; and b) diamond and ZnO layers (no oxide).....	91
Figure 7.6: The frequency response plot and the SEM picture of a third-order TPoD resonator with a 40 $\mu$ m finger pitch.....	91
Figure 7.7: The frequency response plots measured from TPoD resonator with a 20, 10 and 5 $\mu$ m finger pitch .....	92
Figure 7.8: The TCF curve for a TPoD resonator with 40 $\mu$ m finger pitch resonating at 155MHz.....	93
Figure 7.9: Simulated dual width-flexural mode-shapes in a monolithic ZnO-on-diamond micromachined filter: a) in-phase b) out-of-phase .....	94
Figure 7.10: The SEM of a 400 $\mu$ m long, 20 $\mu$ m wide ZnO-on-diamond monolithic flexural TPoD filter.....	94
Figure 7.11: The frequency response of the device shown in Figure. 7.10 terminated with a) 50 $\Omega$ and b) 500 $\Omega$ .....	94

Figure 7.12: Overlapped rocking curves measured from ZnO sputtered directly on diamond with extra fine grains and on a buffer polished oxide layer.....	95
Figure 7.13: SEM pictures comparing surface topography of the ZnO and the metal layers deposited on; a) extra fine diamond b) polished oxide-covered diamond .....	96
Figure 7.14: Frequency responses measured from a TPoD filter with the same geometries as the device in SEM picture of Fig. 6.9; a) with and b) without the polished oxide in the stack .....	97
Figure 7.15: Frequency response of a TPoD monolithic filter with the same size as the device shown in the SEM of Fig. 6.10.....	97
Figure 7.16: The piezoelectrically-transduced lateral resonant mass sensor .....	98
Figure 7.17: Length-extensional mode-shapes of a device with 70 $\mu$ m long central block and two 30 $\mu$ m long sensing platforms .....	99
Figure 7.18: The SEM of the TPoD resonant mass sensor after FIB Platinum deposition.....	101
Figure 7.19: Resonance response of a lateral-extensional resonant mass sensor, (a) before, and (b) after ~48pg platinum deposition .....	102
Figure 7.20: Comparison between the simulated and measured sensitivity of the TPoD mass sensor.....	103
Figure 7.21: The measured TCF for a ZnO-on-diamond mass sensor .....	101

## SUMMARY

The purpose of this dissertation is to introduce a new class of micromachined devices called thin-film piezoelectric-on-substrate (TPoS) resonators and to study the performance of these devices in RF and sensor applications. TPoS resonators benefit from high electromechanical coupling of piezoelectric transduction mechanism and superior acoustic properties of a substrate such as single crystal silicon. Therefore, the motional impedance of these resonators are significantly smaller compared to typical capacitively-transduced counterparts while they exhibit relatively high quality factor and power handling, and can be operated in air. The combination of all these features suggests TPoS resonators as a viable alternative for current acoustic devices.

In this thesis, design and fabrication methods to realize dispersed-frequency lateral-extensional TPoS resonators are discussed. TPoS devices are fabricated on both silicon-on-insulator and thin-film nanocrystalline diamond substrates. Resonators at frequencies ranging from a few tens of MHz up to a few GHz are fabricated and characterized. The performance of these resonators in simple and low-power oscillators is measured and compared.

A unique coupling technique for implementation of high frequency filters is also introduced in which dual resonance modes of a single resonant structure are coupled. The devices operating based on this technique are named monolithic TPoS filters. The measured results of this work demonstrate the functionality and usage of these filters for single-chip implementation of multiple-frequency narrow-band filters with high out-of-band rejection in a small footprint.



# CHAPTER 1

## INTRODUCTION

From early days of the electronic era, system designers have always depended on mechanically-vibrating elements (e.g., quartz crystals) for most of their frequency synthesis (oscillators) [1] and frequency selection (filters) [2] need. The unprecedented enhancement in the performance provided by these low-loss components have given them enough leverage to continue and extend their presence in electronic devices for many years.

Although the invention of the integrated circuits (IC) revolutionized the electronic industry, the need for off-chip quartz crystal and ceramic resonators has never been moderated. Integrated passives even though useful for some applications, are unacceptably lossy at higher frequencies. Therefore, demand for wireless communication devices operating at high frequencies promoted the application of discrete resonators further more. Meanwhile, piezoelectric vibrating components have evolved into new classes of devices such as surface acoustic wave (SAW) and bulk acoustic wave (BAW) resonators and filters with high operational frequencies. Novel micro-fabrication techniques developed for IC industry created opportunities for batch fabrication of these devices in smaller size and lower cost. However, they still consume far more area than the rest of the electronic circuit and can not be easily fabricated on the same substrate.

During the past several decades, the IC fabrication technology has matured to an extent that manufacturing a hand-held wireless device capable of communicating voice, image, and digital information over multiple frequency bands is practically in reach.

However, variety of resonators and filters required in these types of devices occupy a large percentage of the circuit board area and the manufacturing process is not cost-effective. Therefore, the competition has already started for launching a technology, which enables implementation of all the required frequency-selective components on a single substrate that eventually will be integrated with the electronic circuit.

In this dissertation, we introduce a new class of devices that shows a great potential for replacing the existing bulky, individually-packaged resonators and filters. The general term defining this class of devices is thin-film piezoelectric-on-substrate (TPoS). The piezoelectric and the substrate materials may vary depending on the targeted specifications. The substrate is chosen from materials with low-loss, high energy density, and high acoustic velocity such as single crystal silicon [3] and nanocrystalline diamond (NCD) [4]. Consequently, TPoS resonators exhibit low motional impedance, relatively high quality factors ( $Q$ ), and excellent linearity. Acoustically-coupled resonator filters presented in this work can be used as low-loss narrow-bandwidth (BW) filters in the radio-frequency (RF) band [5]. Oscillators made with these devices are applicable as local reference oscillators in transceiver circuits and also as very precise mass sensors to measure absorbed mass changes in the order of pico-grams in air [6].

This dissertation is prepared in 8 chapters. Chapter 1 is an introduction to the work accomplished and presented in this document. Chapter 2 is a review of the progress and the evolution of acoustic resonant devices. Different types of micromachined resonators are briefly overviewed and compared. In chapter 3 the thin-film piezoelectric-on-substrate devices are introduced as our approach to enable high-performance micromechanical resonators. The advantages of using a piezoelectric-on-substrate

structure are discussed and simple lumped element equivalent electrical models are developed for these devices. In chapter 4 the details of processes developed for fabrication of TPoS resonators on silicon-on-insulator (SOI) are presented. The focus of chapter 5 is on the application of variety of fabricated TPoS resonators in oscillator circuits. Simple sustaining circuits are employed in the oscillation loop and the output characteristics are measured and discussed. The focus of chapter 6 is on the concept of monolithic TPoS filters. The operation principle and the design guidelines for both lateral and thickness mode filters are studied. The measured frequency plots from fabricated monolithic TPoS filters are presented and discussed. Techniques to design for the filter BW in both lateral and thickness modes are also introduced and tested in practice. Chapter 7 is on TPoS resonators and filters fabricated on nanocrystalline diamond substrate. Diamond is used to extend the operation frequency of TPoS devices. Preliminary results are presented and compared with similar devices fabricated on silicon. Finally in chapter 8 the accomplishments in this dissertation are briefly summarized and some future research directions are pointed out.

## **CHAPTER 2**

### **BACKGROUND**

Despite all the technological advancements in micro-fabrication and IC electronics, off-chip frequency-selective piezoelectric components such as quartz crystals and SAW devices are widely used in wireless transceiver architectures [7,8]. These components gain their popularity partly from their low-impedance characteristics, which is a result of high electromechanical coupling of the piezoelectric transduction mechanism. This low impedance translates into low insertion loss (IL) in filters and low power consumption in oscillators. The quality factor value in quartz resonators is also exceptionally high which promotes their application. High resonator  $Q$  improves the selectivity in filters [9] and phase-noise in oscillators [10,11]. These very unique qualities are the reason for which finding a replacement for these devices has been unsuccessful for decades, even though they suffer from their large size and fail to be integrated with the electronics.

The concept of micro-electro-mechanical (MEM) resonators was introduced for the first time in the 60's [12] and upon advancement in the material, design, and processing of polysilicon micro-resonators in the 80's [13], MEM resonators were proposed as candidates to substitute conventional piezoelectric vibrating components. The reduced size, IC compatible fabrication process, and potentially reduced manufacturing cost of a MEM resonator have attracted a lot of attention during the past few decades. These devices inherently have a high quality factor and their performance

benefits justify additional fabrication processes, which are required to enable a resonant structure on an electronic chip.

MEM resonators have grown immensely during the past decade to a state in which they can competitively meet the requirements imposed by the market. Many studies have been conducted to understand their characteristics and limitations [14,15], and some of the earlier efforts such as film bulk acoustic resonators (FBAR) have already matured enough to find their way into commercial products [16].

Micromachined resonators can be classified into two general categories: capacitive and piezoelectric. The characteristics of each device type will be further discussed in the following sections.

## **2.1 Capacitive Micro-Resonators**

In this class of MEM resonators, capacitive transduction mechanism is employed to excite the resonance mode of a micromechanical structure and also to detect the vibration amplitude. Narrow gaps are designed between the highly conductive resonator body and the conductive electrodes. A polarization voltage is applied between the electrodes and the resonator to create the required electric field for excitation and detection. These devices, if fabricated from low acoustic loss material, such as polysilicon and single crystal silicon, usually exhibit very high quality factors in the range of a few hundred thousands in vacuum [17,18]. These values are equivalent to what is achievable from quartz crystals. The motional impedance of capacitive devices is inversely proportional to the capacitive gap size to the fourth power [19]. Therefore, in order to realize reasonably small impedances at high frequencies very small gap sizes are required, which are challenging to fabricate. Some other techniques have been proposed

to increase the actuation area rather than reducing the gap size in order to increase the electromechanical coupling [20,21]. High frequency, high  $Q$  resonators are attained with relatively low motional impedances using these methods [22]. However, in spite of all the advancement, the main limitation with capacitive resonators will remain to be the large motional impedance which tends to escalate as the frequency increases.

Another alternative capacitive transduction technique proposed recently is to fill the gap with a high permittivity dielectric material [23,24]. This method is very attractive since it simplifies the fabrication process and eliminates the need for very small capacitive air gaps. Moreover, the electric field is stronger in the dielectric compared to the air or vacuum and therefore very large electromechanical coupling values are expected. However, in practice the motional impedance is not improved as expected and also the quality factor of the fabricated devices using this technique are lower compared to the devices operating with air gaps [25]. Moreover, the stray capacitance between the electrode and the resonant body will be significantly large as a result of the high permittivity of the material filling the gap. Consequently, unless the parasitic capacitance is de-embedded, limitations will be imposed on the termination impedances that can be interfaced with the device.

## **2.2 Piezoelectric Micro-Resonators**

Micromachined piezoelectric resonators are descendants of discrete piezoelectric vibrating components which are fabricated using techniques adopted from micro-fabrication technology. The two most important classes of these devices are bulk acoustic wave (BAW) [26] and surface acoustic wave (SAW) [27] devices. The electromechanical coupling of piezoelectric transduction is much larger than capacitive

transduction. Therefore, the motional impedance of piezoelectric resonators is inherently lower compared to their capacitive counterparts, especially at higher frequencies where the capacitive transduction loses efficiency.

The resonant structure in thin-film piezoelectric resonators (e.g., FBAR) is not made of a single crystal material, and it usually consists of a stack of multiple layers (including metal electrodes). In addition, thin-film piezoelectric materials such as lead zirconium titanate (PZT) are not low-loss [28] and are usually anchored on top of a substrate that acts like an energy-sink increasing the acoustic energy dissipation in the system. Therefore, quality factors reported from these devices are not as high as the values obtained from capacitive devices. Despite this deficiency, piezoelectric resonators have outperformed capacitive resonators at high frequencies particularly in applications such as filters where very high  $Q$  values are not required. Since the focus of this thesis is on one type of thin-film piezoelectric resonators, in the following sections the operation principle of these devices will be reviewed in more details.

### **2.2.1 Piezoelectricity: Principles and Early Application**

Piezoelectric effect is a bidirectional electro-mechanical transduction mechanism discovered for the first time by Curie brothers in 1880. Almost all non-centrosymmetric crystal materials (unit-cell has no centre of symmetry) exhibit piezoelectricity. Electrical charge is developed in a piezoelectric crystal under mechanical stress. The amount of charge is proportional to the applied stress and this phenomenon is called direct piezoelectric effect. Also, an electrical field induced in a piezoelectric material causes a mechanical strain in the structure which is called the reverse piezoelectric effect.

The first practical application of piezoelectric devices appeared a few decades after the discovery of the effect and dates back to 1910 when piezoelectric transducers were utilized in sonar submarine detectors. From that point on piezoelectric sensors and actuators are studied vigorously and have found numerous applications such as sensitive gravimetric chemical and biological sensors [29], atomic force microscopy [30], frequency generating components [31], etc.

### 2.2.2 Piezoelectricity: Formulation

As described earlier, piezoelectricity is a coupled electrical and mechanical phenomena. The electrical behavior of materials can simply be described by:

$$D = \varepsilon E \quad (2.1)$$

where  $D$  is the electrical displacement,  $\varepsilon$  is the permittivity of the material, and  $E$  is the electrical field strength.

Similarly, Hook's law is used to express the mechanical behavior of materials:

$$S = sT \quad (2.2)$$

where  $S$  is the strain,  $s$  is the compliance, and  $T$  is the stress.

In piezoelectric crystals a new constant is defined which combines the two aforementioned equations and construct the coupled-field electro-mechanical equation set:

$$\begin{aligned} D &= \varepsilon^T E + dT \\ S &= d^t E + s^E T \end{aligned} \quad (2.3)$$



where  $d$  represents the piezoelectric constant,  $\varepsilon^T$  is the permittivity at a constant stress, and  $s^E$  is the compliance at a constant electric field. In the most general form stress, strain, and electric field are Cartesian vectors and the coefficients are tensors.

### 2.2.3 Piezoelectric Resonators

Piezoelectric resonators conventionally consist of a piezoelectric substrate suspended from the edge and covered with thin film metal electrodes, which are patterned on the two surfaces of the substrate (Fig. 2.1).

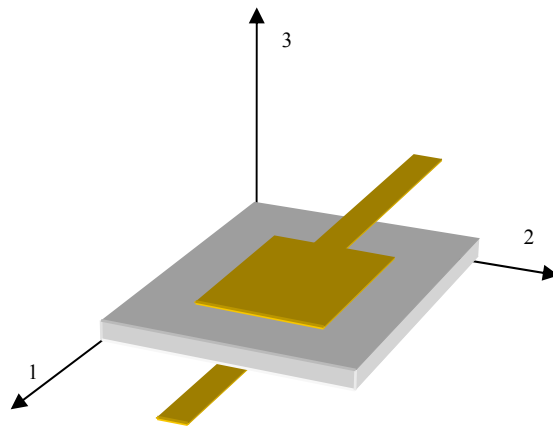


Figure 2.1: A simple stack of a piezoelectric substrate and metallic electrodes

The two conductive metallic electrodes are connected to the electronic signal lines and when the frequency of the applied signal is equal to a natural resonance frequency of the structure, that resonance mode is excited. The targeted mode-shape can be designed by alternating the electrode patterns and the location of the suspension elements.

One of the most commonly employed resonance modes in piezoelectric devices is the thickness extensional mode in which the strain field is in the same direction as the applied electrical field. For example in Fig. 2.1, applying an alternative voltage to the two

electrodes will establish a corresponding alternative electrical field in the direction of the axis number 3. Assuming that the utilized piezoelectric substrate has a non-zero  $d_{33}$  piezoelectric constant following the equation set of (2.3):

$$S_3 = d_{33}E_3 \quad (2.4)$$

a parallel alternating strain field will develop in the structure (Fig. 2.2).

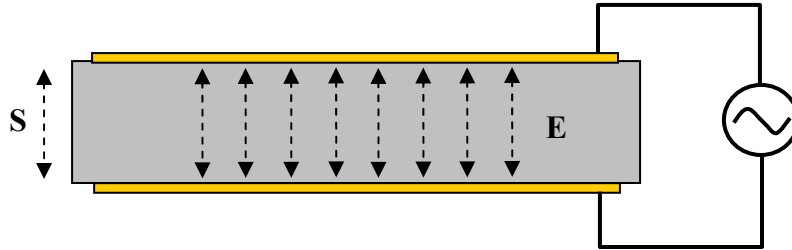


Figure 2.2: The schematic representation of the electric field and the corresponding strain field in a thickness mode piezoelectric resonator

Since  $d_{33}$  is not the only non-zero piezoelectric coefficient in the material used as the structural body of the resonator, strain field in other directions is also likely to be developed. For example in Fig. 2.1,  $d_{31}$  is responsible for generating a strain field orthogonal to the electrical field and in parallel with the axis number 1:

$$S_1 = d_{31}E_3 \quad (2.5)$$

Now depending on how the substrate is clamped, strain field ( $S_1$ ) can excite different resonance modes. For example, if the thin piezoelectric plate is clamped on the nodal points of the fundamental length-extensional resonance mode (the center of a block) the lateral mode can be excited while the electric field is developed across the thickness of the film (Fig. 2.3)

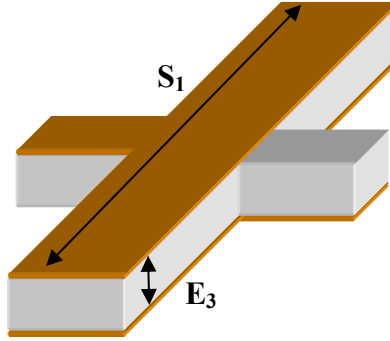


Figure 2.3: The schematic viewgraph of a lateral-extensional mode piezoelectric resonator

The displacement of each particle in the resonator is governed by a partial differential equation called wave equation [32]. Closed form solution for this equation is usually approximated after considering some simplifying assumptions such as small vibration amplitude to eliminate nonlinearities from the equations.

### 2.3 Resonator Mechanical Modeling

Every mechanical resonator can be approximated by an equivalent lumped mass-spring (-damper) system (Fig.2.4).

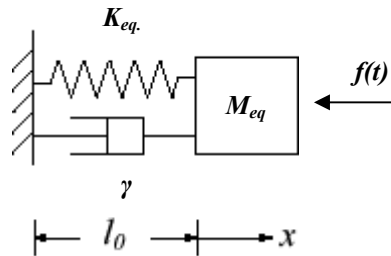


Figure 2.4: A mass-spring-damper representation of a mechanical resonator

The equivalent mass is equal to the total kinetic energy in the resonator divided by one-half the velocity (in a specified direction). Regardless of any particular resonance mode of the structure, if the material is isotropic (properties are the same in all directions), the natural resonance frequency will be in this format:

$$f = \frac{A}{B} \sqrt{\frac{E}{\rho}} = \frac{1}{2\pi} \sqrt{\frac{K_{eq.}}{M_{eq.}}} \quad (2.6)$$

where  $A$  is a unitless value (may be as simple as a constant or some complex function).  $B$  is a function having the units of length (meter).  $E$  is the Young's modulus, and  $\rho$  is density of the material. The damping coefficient ( $\gamma$ ) is a measure of energy loss in the system and can be defined based on the quality factor of the resonator:

$$\gamma = \frac{2\pi f M_{eq.}}{Q} \quad (2.7)$$

For a bar with the length of  $L$  and the cross section area of  $A$ , resonating in its extensional mode along the length of the bar (Fig. 2.3) the resonance frequency is calculated from:

$$f = \frac{n}{2L} \sqrt{\frac{E}{\rho}} \quad (2.8)$$

where  $n$  is the mode number, and the equivalent mass is simply in the form of:

$$M_{eq.} = \frac{\rho AL}{2} \quad (2.9)$$

Therefore, the equivalent stiffness is:

$$K_{eq.} = \frac{n^2 \pi^2 AE}{2L} \quad (2.10)$$

## 2.4 Resonator Equivalent Electrical Model

The differential equation governing the motion in the equivalent mechanical model of Fig. 2.4 is written as:

$$M_{eq} \frac{\partial^2 x}{\partial t^2} + \gamma \frac{\partial x}{\partial t} + K_{eq} x = f(t) \quad (2.11)$$

This equation is analogous to the equation derived for an RLC electrical circuit (Fig. 2.5):

$$L \frac{\partial i}{\partial t} + Ri + \frac{1}{C} \int idt = v(t) \quad (2.12)$$

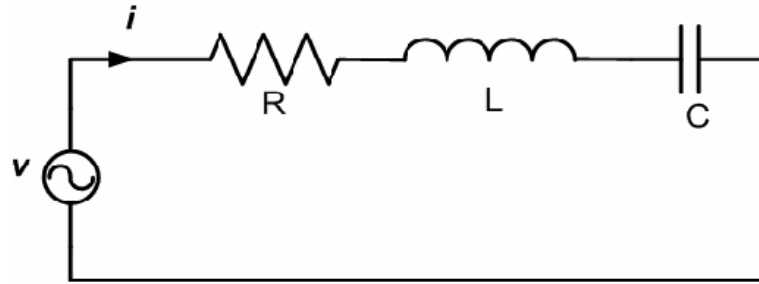


Fig. 2.5: An RLC equivalent circuit for a mechanical resonator

Therefore, any mechanical resonator can be modeled with a simple RLC circuit where:

$$R = \gamma, L = M_{eq}, C = \frac{1}{K_{eq}} \quad (2.13)$$

However, in electromechanical resonators the effect of the transduction mechanism should also be included in the model. Moreover, a feedthrough capacitance should be added in parallel with the RLC path to account for a portion of the electrical signal that is not converted to acoustic energy and passes through a physical capacitance from input directly to the output or to the ground.

#### 2.4.1 One-Port Piezoelectric Resonator Electrical Model

The piezoelectric resonator of Fig 2.2 is identified as a one-port device since there is a single pair of input/output connections to the device. In this configuration the static capacitance ( $C_0$ ) presented between the two metal electrodes is in parallel with the

motional branch in the electrical model (Fig. 2.6). The piezoelectric transduction is represented by a transformer with the turn ratio of  $1:\eta$ .

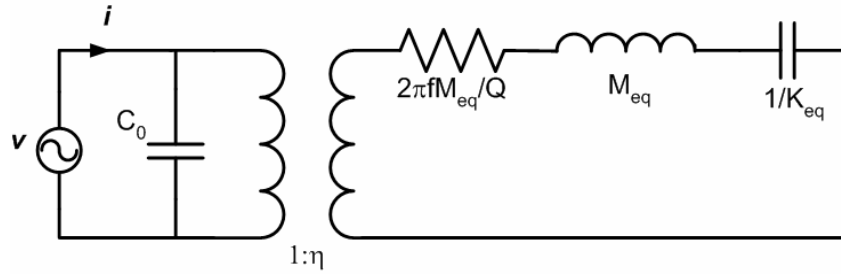


Figure 2.6: A simple electrical model for a piezoelectric resonator

$(\eta)$  is the electromechanical coupling coefficient and is defined as the ratio of the current passing through the resonator to the maximum velocity or alternatively, the ratio of total charge stored on an electrode to maximum displacement:

$$\eta = \frac{Q_{total}}{u_{max}} = \frac{i}{v_{max}} \quad (2.14)$$

It should be noted that there always exists some parasitic capacitance between the two connections to the device that is included in the parallel capacitance of  $C_0$ . However, this portion of the capacitance can not be predicted practically.

The resonator model of Fig. 2.6 can be further simplified to the lumped-element representation of Fig. 2.7. This is the same as the model known as Butterworth Van Dyke (BVD) in literature [33].

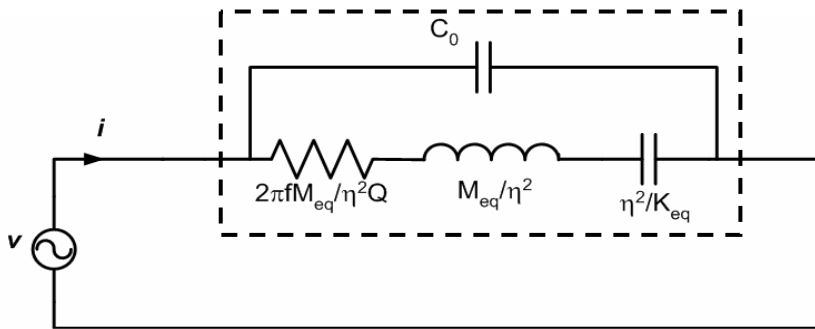


Figure 2.7: The BVD electrical representation for a one-port piezoelectric resonator

### 2.4.2 Two-Port Piezoelectric Resonator Electrical Model

In a two-port device there are two pairs of connection to the device (Fig. 2.8). The signal applied to the input port is converted to acoustic vibration in the structure and the output port converts the vibration back to an electrical signal.

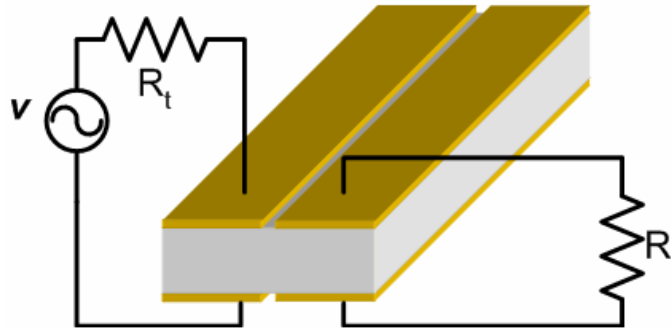


Figure 2.8: The schematic viewgraph of a two-port piezoelectric resonator

Consequently, the equivalent electrical model of the resonator should contain the transduction components for both input and output ports (Fig. 2.9)

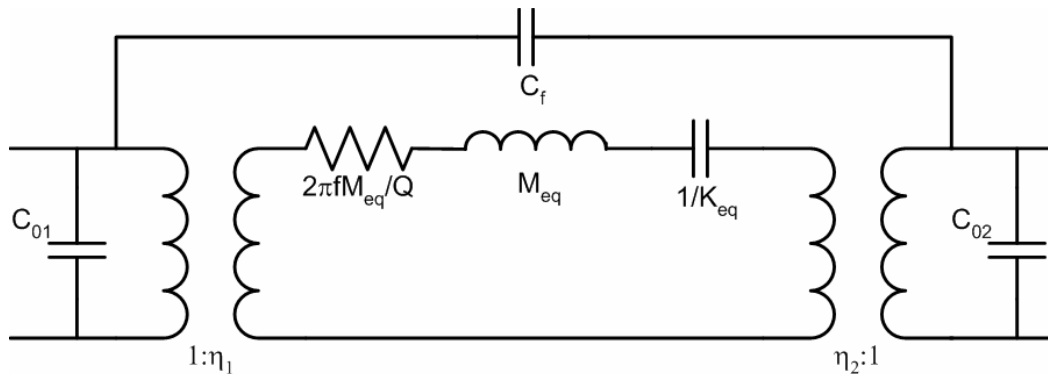


Figure 2.9: The electrical equivalent model of a two-port piezoelectric resonator

In its most general form, the input and output coupling coefficients ( $\eta_1, \eta_2$ ) as well as the static shunt capacitors can be of different values. Here,  $C_f$  represents the parasitic feedthrough capacitance that always exist between the input and output electrodes. This

feedthrough capacitance is usually small (fF range) and can only be practically measured after the fabrication of the device. Even though small, feedthrough capacitance plays a role in the frequency response of the device especially at higher frequencies.

Once again the equivalent circuit of Fig. 2.9 can be further simplified to the model shown in Fig. 2.10.

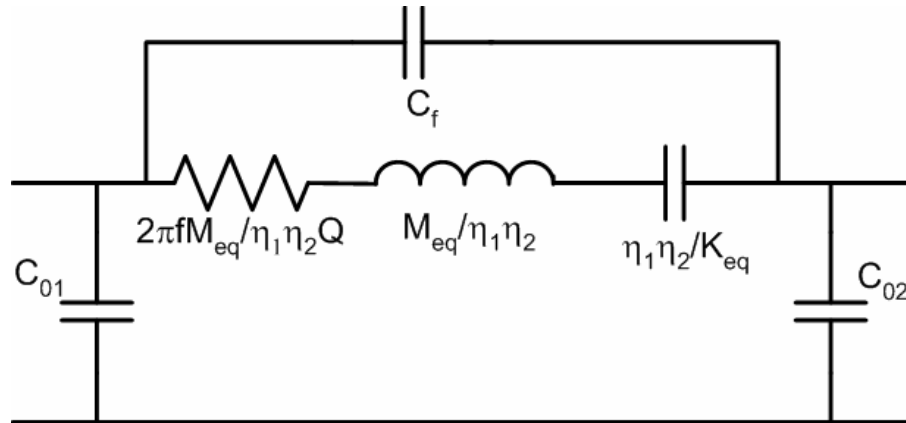


Figure 2.10: The simplified electrical model of a two-port piezoelectric resonator

It should be noted that, the above simplification is only valid if the transduction mechanism does not invert the phase of the signal or in the other word the winding direction in transformers of Fig. 2.9 are both identical.

## 2.5 MEM Coupled-Resonator Filters

Mechanically-coupled quartz crystal filters are amongst the earliest mechanical filters demonstrated. These filters ruled the IF to UHF filter market for decades and continue to have a large market-share [34,35]. The next generation of commercially available mechanical filters was based on application of surface acoustic waves (SAW). SAW filters are currently employed in communication devices. These relatively large devices are usually fabricated on a piezoelectric substrate (e.g. lithium niobate) and still



suffer from similar problems as quartz crystal filters;--they cannot be integrated with electronics [27].

FBAR filters are the latest generation of filters from the piezoelectric device family, and they are commercially available for application in wireless transceiver architectures [16]. These devices can potentially be integrated with CMOS which gives them an edge over other technologies at very high frequencies, where very small interconnects are essential [36]. The important shortcoming of these filters is that the center frequency is defined by the thickness of a thin-film piezoelectric layer, which is uniformly deposited across a single substrate. As a result, these devices fail to offer a compact and cost effective solution for emerging wireless applications where data communication may be performed on several channels at different frequencies.

Micromachined capacitive coupled-resonator filters, when proposed a decade ago, attracted a lot of attention since they promised a compact solution for implementation of arrays of filters with dispersed center frequencies on a silicon substrate [37]. They could also meet the integration requirements where most available technologies fall short. Although, many filters based on capacitive resonators have been demonstrated, none of those satisfy the frequency, insertion loss, isolation, and dynamic range requirements simultaneously [38], [39], [40]. In particular, the insertion loss of these filters is excessively large and tends to grow even larger with the increase in the center frequency.

Recently, filters based on contour-mode AlN resonators have been demonstrated at UHF frequencies [41]. These electrically-coupled (ladder) filters show reduced insertion loss values compared to the earlier reported micromachined filters for the same

frequency range. However, their ability to maintain the same level of insertion loss and isolation at higher frequencies is arguable.

The challenge is that at higher frequencies in order for the lateral piezoelectric device to offer low enough motional impedance and reasonably high absolute frequency accuracy, high-order modes of large suspended structures should be utilized [42]. These large and thin structures anchored with small support beams are prone to fracture when fabricated from a single piezoelectric layer. Moreover, filters comprising of a few number of electrically-coupled resonators in a ladder or lattice configuration can not meet the isolation requirement at high frequencies. Therefore, a low insertion-loss acoustically-coupled micromachined filter operating in RF band is an immediate need that will be investigated in this work.

A resonator technology that combines the high electromechanical coupling of piezoelectric resonators with high energy density and low-loss in substrate materials such as single crystal silicon can be a solution for the problem. The lithographically-defined operational frequency of a lateral bulk acoustic resonator design (LBAR) is also a valuable feature enabling single-chip implementation of multiple-frequency resonant devices for applications in next generation communication equipment.

## CHAPTER 3

### THIN FILM PIEZOELECTRIC-ON-SUBSTRATE TECHNOLOGY

In this chapter thin film piezoelectric-on-substrate (TPoS) technology is introduced as a platform for fabrication of resonators with operating frequencies spanning from few tens of MHz to a few GHz. These devices can be utilized in analog signal processor and gravimetric sensor applications.

#### 3.1 TPoS Resonator Structure

A TPoS resonator is comprised of a thin ( $<1\mu\text{m}$ ) piezoelectric layer sandwiched between two metallic electrodes stacked on top of a relatively thick ( $>2\mu\text{m}$ ) layer of low-acoustic-loss material (such as single crystal silicon or nanocrystalline diamond). The resonant structure is released from the rest of the substrate and it is suspended by anchors placed around the resonator edge (Fig. 3.1).

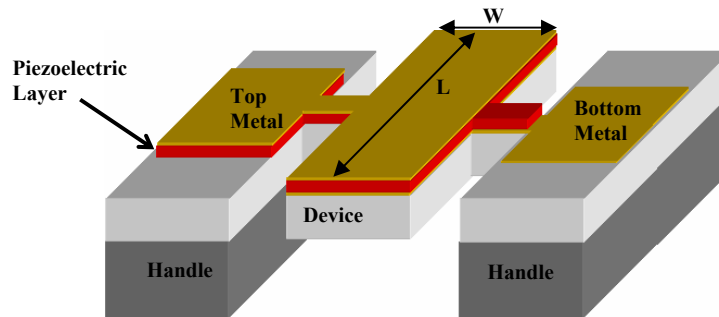


Figure 3.1: The schematic view graph of a one-port TPoS resonant structure

The typical resonator shown in Fig. 3.1 is an example of a one-port TPoS block resonator, which in principal can be represented by the same one-port electrical model introduced in Fig. 2.7.

Metal electrodes in a TPoS resonator can also be split into electrically isolated pairs to form two-port resonators. The resonator geometry and the metal electrode patterns identify the main excited resonance mode as well as the resonance frequency.

### **3.1.1 Why Piezoelectric on Substrate?**

In conventional piezoelectric resonators such as quartz crystal, ceramic, and saw devices the device is fabricated on a piezoelectric substrate which is either made of a single crystal material (quartz) or poled polycrystalline material (ceramic). The micromachining techniques developed for IC industry provide the means for scaling down the size and the cost, and increasing the operation frequency of modern piezoelectric devices. In these devices the starting substrate is usually a silicon wafer which guarantees compatibility with processing tools developed for silicon microelectronics. Since silicon is not a piezoelectric material, the piezoelectric film will be deposited on the silicon substrate and comprises the active acoustic media.

There are many different techniques developed for depositing a piezoelectric material on a substrate. The deposited piezoelectric layer in most of these techniques consists of many small crystalline grains that their axis of symmetry is aligned to a single direction. In this way the polycrystalline layer demonstrates a non-zero average piezoelectric effect. Plasma sputtering (both RF and DC) is among the most useful and frequently used methods for depositing piezoelectric layers such as ZnO and AlN [43,44].

The problem with depositing a polycrystalline piezoelectric film is two-fold. One is the thickness of the film which can not be usually more than a few microns because the deposition rate is usually small for sputtered films (e.g. AlN and ZnO) and also anisotropic etching of a thick piezoelectric film is not trivial. Second is the internal stress

in the polycrystalline film. The stress developed in the film after deposition will be specifically problematic for the relatively thin piezoelectric devices that have to be released from the substrate. The stress will cause the suspended devices to curve up or down and occasionally may cause the larger devices to fracture. A thin piezoelectric film will also limit the power handling and the linearity of the device fabricated from the film. We will study linearity in resonators in more detail in the next section.

### 3.1.2 Power Handling in Piezoelectric Resonators

The smaller size of the micromechanical resonators, despite all its advantages has an inevitable drawback when it comes to the maximum allowable stored energy or in other word power handling. Power handling is a measure of the amount of power that can be applied to or delivered by the resonator. The power handling is mostly limited by the nonlinearity mechanisms in the resonator. Since nonlinear vibration of the resonator will introduce noise and distortion in the output signal of the system the applied power to the resonator should be kept less than the nonlinear limits at all time. In order to study the power handling limits in a TPoS resonator we consider the equation of motion for a forced oscillatory system:

$$m\ddot{x} + \gamma\dot{x} + kx = F(t) \quad (3.1)$$

where  $m$  is the lumped mass,  $\gamma$  is the damping coefficient, and  $k$  is the spring coefficient. In a linear system the spring coefficient is a constant where as in a nonlinear system the coefficient can be written as:

$$k = k_0 (1 + k_1 x + k_2 x^2 + \dots) \quad (3.2)$$

where  $k_1, k_2, \dots$  are nonlinear spring constants. A nonlinear spring coefficient will cause higher harmonics of the natural resonance frequency to appear in the output:

$$x(t) = A_0 + A_1 \cos \omega_n t + A_2 \cos 2\omega_n t + \dots \quad (3.3)$$

Consequently, the resonance frequency (frequency at which the largest vibration amplitude occurs) is dependent on the vibration amplitude [45]:

$$\omega_{nonlinear} = \omega_n \left( 1 - \frac{5k_1^2}{12} A_1 + \frac{3k_2}{8} A_1 \right) \quad (3.4)$$

From the above expression it is identified that a non-zero first-order nonlinear spring coefficient ( $k_1$ ) will shift down the resonance frequency and the second-order nonlinear coefficient ( $k_2$ ) will shift the frequency either up or down depending on its sign. It is usually assumed that the limit for largest allowable vibration amplitude is the bifurcation point (the critical point after which the amplitude versus frequency plot will demonstrate hysteresis) (Fig. 3.2). Depending on which one of the two nonlinear spring coefficients are dominant, the maximum vibration amplitude can be calculated from [45]:

$$x_{c1} = 1.36 \sqrt{\frac{1}{k_1^2 Q}} \quad \text{or} \quad x_{c2} = 1.43 \sqrt{\frac{1}{|k_2| Q}} \quad (3.5)$$

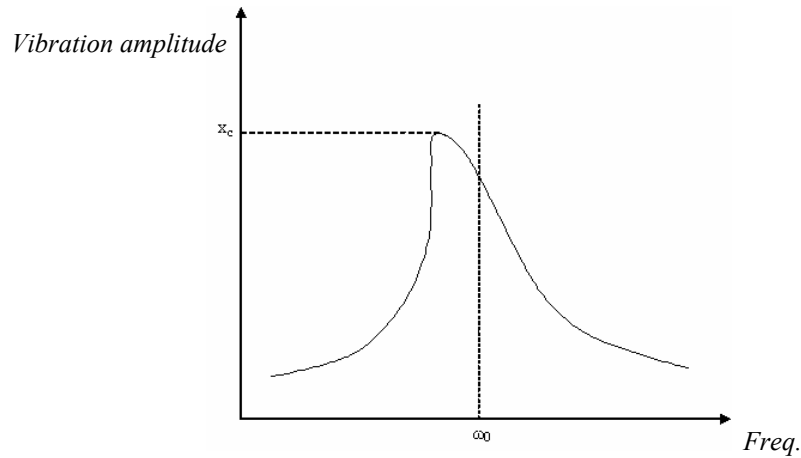


Figure 3.2: A frequency response plot of a resonator operating at bifurcation

By incorporating the maximum allowable vibration amplitude, the maximum stored energy in the resonator can be calculated from:

$$E_{\max} = \frac{1}{2} k_0 x_c^2 \quad (3.6)$$

It is clear from the above analysis that the maximum stored energy or in other word, the power handling is directly proportional to the stiffness of the resonance mode which in turn is proportional to the thickness of the device for a lateral-mode resonator (Eqn. 2.10). It is also inversely proportional to the square root of quality factor which implies that resonators with higher  $Q$  are more susceptible to nonlinearity. Needless to say, smaller nonlinear spring coefficients increase the power handling. Nonlinear spring coefficients are dictated by material properties and vary for each material of choice.

To compare the nonlinearity limitations for different material a normalized parameter called energy density is defined as the maximum allowable energy divided by the volume of the resonant structure. Silicon and Diamond exhibit orders of magnitude larger energy density than piezoelectric material such as quartz and AlN [46,47,48].

### 3.1.3 Quality Factor in Piezoelectric Resonators

The quality factor of a resonator, defined as the ratio of energy stored to the energy lost per cycle, is limited by various dissipation mechanisms and can be expressed as:

$$Q = \left( \frac{1}{Q_{\text{material}}} + \frac{1}{Q_{\text{anchor}}} + \frac{1}{Q_{\text{air}}} \right)^{-1} \quad (3.7)$$

where  $(1/Q_{\text{material}})$ ,  $(1/Q_{\text{anchor}})$ , and  $(1/Q_{\text{air}})$  are material damping, anchor loss and air damping respectively. The loss due to air damping  $(1/Q_{\text{air}})$  can be prevented by operating

the resonator in vacuum. The piezoelectric resonators are in general less susceptible to air damping compared to capacitively-transduced resonators since the required narrow capacitive gap is not present in piezoelectric resonators [49]. The narrow capacitive gap is the source of a strong damping mechanism called squeeze film damping that can considerably reduce the quality factor of capacitive resonators especially at low frequencies. The other two sources of energy loss ( $1/Q_{anchor}$  and  $1/Q_{material}$ ) are common between all types of resonators.

Anchor loss is attributed to the radiation of acoustic energy from the resonant body through the anchors, which keep the resonator in place. These anchors depending on the design of the resonator can be seen in many different forms but they contribute nevertheless to the final quality factor of the resonator in the same way. The acoustic waves are not completely confined in the resonator and rather radiate through the anchors and leak into the surroundings. The acoustic energy carried by these waves is considered lost since this energy is not conserved in the resonator. In order to reduce the anchor loss, some design guidelines are devised [50] but these rules usually lose applicability as the dimension of the resonator is reduced for high frequency devices.

The two sources of energy loss discussed so far were imposed by the environment outside of the resonator. The third loss mechanism, however, is not of the same nature. Material damping ( $Q_{material}$ ) includes all the energy loss mechanisms that are intrinsic to the resonant structure. Material loss relates to the irreversible transformation of acoustic energy to thermal energy. There are two well-known mechanisms for this energy transformation. One is called thermoelastic damping which was studied by Zener for the first time [51]. Thermoelastic loss occurs because there is a slight temperature difference



between the regions of the resonator under compression and tension and therefore heat flows between the hot and cold regions. This source of material damping is only dominant in the close vicinity of frequencies that corresponds to the thermal relaxation time constants of the resonator [52]. At other operational frequencies a different thermal-loss mechanism proposed by Akheiser is effective [53]. In the Akheiser effect a sudden applied strain disturbs the equilibrium distribution of the phonons and thermal phonons are excited in the relaxation process.

The Akheiser loss mechanism limits the absolute maximum quality factor of a resonator made of a certain material. The contribution of this loss mechanism can be quantified by a coefficient called acoustic attenuation ( $\alpha$ ). The larger this coefficient for a material is the lower the absolute maximum achievable quality factor of the resonator made of that material will be. The acoustic attenuation in diamond and silicon is lower than the attenuation in common piezoelectric materials such as PZT, AlN and ZnO used in thin-film resonators [54,55,56]. Therefore, in a TPoS resonator where a large portion of the resonant structure is made of single crystal silicon or diamond, the acoustic energy is mostly contained in a low loss material that can potentially improve the quality factor of the resonator compared to a device made of thin-film piezoelectric material only. Some experimental data supporting this claim will be presented in the next chapters.

### **3.2 Lateral versus Thickness Resonance Modes**

Electric field in TPoS resonators is orthogonal to the substrate plane. If the acoustic wave propagation direction is parallel with the electric field the resonance mode is called a thickness mode and the resonance frequency is defined primarily by the thickness of the structure. If the elastic-wave motion is transverse to the electric field, by

definition a lateral mode is excited and the resonance frequency is mostly dependent on the in-plane dimensions of the resonant structure.

The focus of this work is on lateral mode resonators. The advantage of utilizing these modes is that since the lateral dimension of the resonator is defined lithographically, the operation frequency of the devices fabricated on a single substrate can span a wide range (from few MHz to a few GHz). Where as, thickness mode resonators fabricated on a substrate, are bound to have almost the same center frequency since the device thickness is the same all over the substrate. On the other hand, the piezoelectric materials used to make TPoS resonators are sputtered polycrystalline materials which are mostly transversely isotropic. In other word, the z axis (orthogonal to the plane) has an infinite order of symmetry and it has the largest piezoelectric coefficient ( $d_{33}$ ). Therefore, compared to lateral mode resonators where ( $d_{31}$ ) is utilized to excite the resonance mode the electromechanical coupling is larger for thickness mode resonators [57]. Consequently, the motional impedance of a thickness-mode resonator is lower considering the same-size actuation (electrode) area.

### **3.3 Lumped Element Electrical Model of Lateral-Extensional TPoS Resonators**

To calculate the values of the components in the equivalent electrical model of Fig. 2.7 for the TPoS resonator of Fig. 3.1, the resonance frequency and mode-shape of the resonator are required. Mathematical expressions defining these parameters are often not readily available for complex geometries such as the composite structure of a TPoS resonator. Assuming a one-dimensional model for the TPoS block resonator shown in Fig. 3.1 resonating in its length-extensional mode (strain field in parallel with L) the mode-shape and the resonance frequency can be approximated by:

$$u_n(x) = \cos\left(\frac{n\pi x}{L}\right) \text{ for } x = [0, L]$$

$$f_n = \frac{n}{2L} \sqrt{\frac{E_{eff}}{\rho_{eff}}} \quad (3.8)$$

where  $n$  is the mode number,  $E_{eff}$  is the effective unidirectional stiffness modulus and  $\rho_{eff}$  is the effective mass density. By using the equations above the component values in the lumped element electrical model are calculated to be:

$$M_{eq} = \rho_{eff} A \int_L [u(x)]^2 dx = \frac{\rho_{eff} AL}{2}$$

$$K_{eq} = \omega_n^2 M_{eq}$$

$$\gamma = \frac{K_{eq}}{\omega_n Q} \quad (3.9)$$

$$\eta = \frac{F_{modal}}{V} = \frac{\int F(x)u(x)dx}{V} = \frac{\int T(x)A_f u(x)dx}{V} = 2d_{31}E_f W$$

where  $A_f$  is the cross section area of the piezoelectric film and  $A$  is the total cross section area of the piezoelectric film plus the substrate, normal to the direction of the acoustic propagation ( $x$ ). Using the above parameters the equivalent motional inductance, capacitance, and resistance of the electrical model can be calculated from the equation set (2.13).

Finally, we introduce a new parameter called effective coupling coefficient which is defined the same way as effective coupling coefficient in conventional bulk acoustic wave piezoelectric resonators [32]:

$$k_{eff}^2 = \frac{C_m}{C_m + C_0} \approx \frac{C_m}{C_0} \quad (3.10)$$

where  $C_0$  is the static capacitance and  $C_m$  is the motional capacitance of the resonator at resonance (Fig. 3.3). The product of  $Q$  and the effective coupling coefficient is a very

useful figure of merit that quantifies the ratio of the current passing through the motional (mechanical) branch of the electrical model to the current passing through the static capacitance at resonance (Fig. 3.3). We will see later on that this ratio can significantly affect the IL and the passband ripple of the filters comprised of these devices.

$$k_{eff}^2 \cdot Q = \frac{1}{\omega_r R_m C_0} = \frac{1/(\omega_r \cdot C_0)}{R_m} = \frac{I_m}{I_S} \quad (3.11)$$

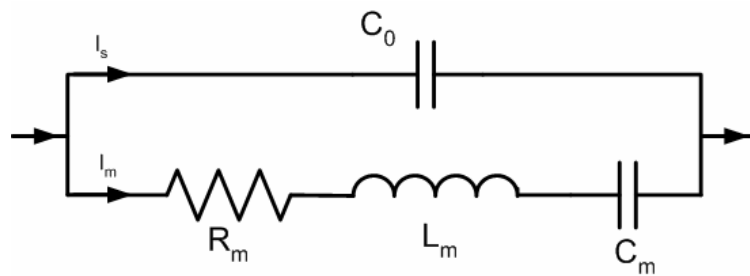


Figure 3.3: The representation of the current divided between the two motional and feedthrough branches in the resonator model

# CHAPTER 4

## FABRICATION PROCESS

In this chapter the developed process flow for fabrication of TPoS resonators on SOI is discussed. Each fabrication step is explained in detail, practical issues are pointed out and a solution for problems are proposed and applied.

### 4.1 Process Flow on SOI

The process flow for TPoS resonators fabricated on SOI is presented in Fig. 4.1. This is a five-mask low-temperature process starting with a high resistivity SOI wafer comprising a 2-10 $\mu\text{m}$  thick silicon device layer. The resistivity of the silicon layer is chosen to be as high as possible in order to minimize the parasitic capacitance associated with metallic pads used for landing a probe tip or connecting a wire-bond.

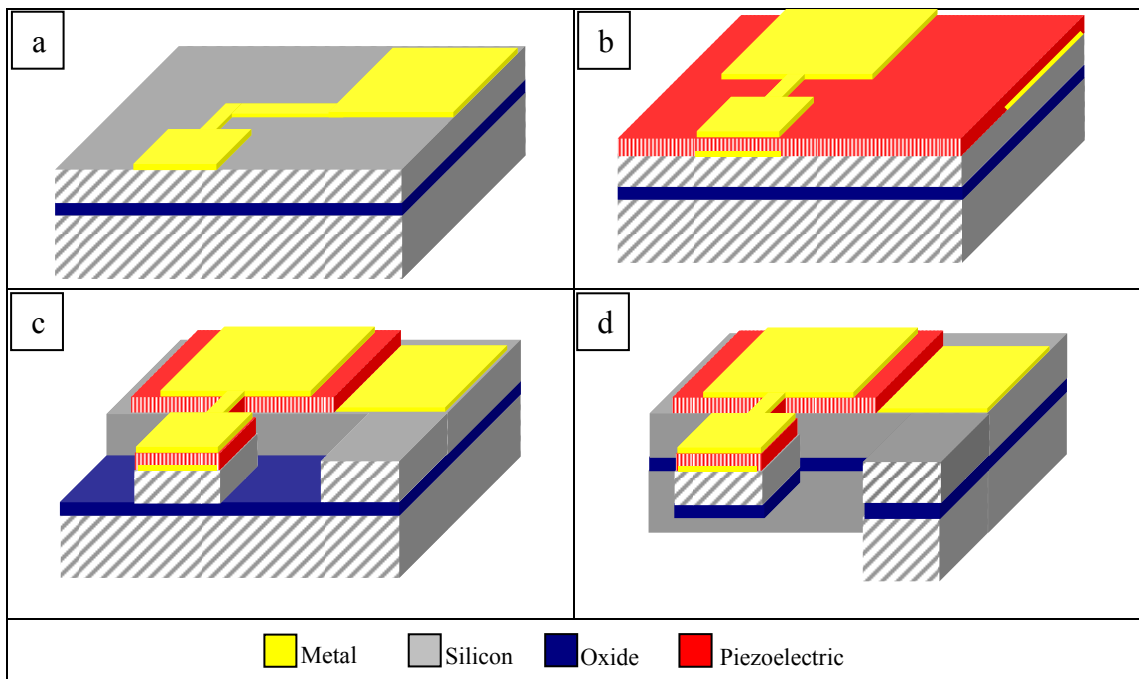


Figure 4.1: The schematic process flow for fabrication of TPoS devices on SOI

In case the resistivity of the silicon layer is not high enough a very thin insulator layer such as silicon dioxide or silicon nitride can be deposited on the substrate before starting the process. In the next few sections each processing step will be discussed.

#### **4.1.1 Bottom Metal Layer Deposition**

The first processing step is the bottom metal layer deposition and patterning (Fig. 4.1a). Lift-off process is used to pattern the metal layer and Shipley 1813 positive photoresist is used to create the bottom electrode openings on the wafer. The choice of material for this layer is delicate and depends on many parameters. Since the bottom electrode is the seed layer for the piezoelectric film, careful attention should be devoted to the crystallographic structure of the metal and the deposition condition. The two piezoelectric materials used in this thesis are ZnO and AlN. Different metallic seed layers have been studied in the literature for both AlN and ZnO films with mixed reported results which makes a conclusive decision on the advantage of one over the other hard to reach. The materials of interest in our work are gold (Au), platinum (Pt), Aluminum (Al), and Molybdenum (Mo). We will discuss the advantages and disadvantages of each metal in the following paragraphs.

Gold is a very attractive choice of metal for our application and especially for devices based on ZnO. The conductivity of gold is one of the best available which is an important parameter since the bottom layer is the ground plane in TPoS devices discussed in this dissertation. Gold is a chemically stable material which imposes minimum constraint for selecting chemical etchants used in the following process steps. However, gold is a malleable metal with large acoustic attenuation coefficient. Also, gold atoms start to diffuse into other material such as silicon and form eutectic alloys at relatively

low temperatures (300°C) [58]. To achieve a low-stress piezoelectric film, deposition temperatures higher than 300°C are usually required for ZnO [59]. Therefore, gold, even though chosen as the metal of choice in most of the devices fabricated in this work, may not be considered as the ultimate selection for TPoS devices.

Platinum (Pt) on the other hand is a very stable metal that can withstand high annealing temperatures up to 800°C. However, the conductivity of platinum is not as good as gold and the ZnO film sputtered on Pt was not observed to have the same high quality (grains are not highly c-plane oriented). Also, patterning platinum is rather problematic. Platinum etchant (aqua regia) is a very strong acid and very hard to work with [60]. Lift-off process is not a very good option for patterning platinum either, since the sample temperature is elevated during the evaporation process which causes the photoresist layer on the wafer to severely harden. Consequently, the burnt photoresist layer is very hard to remove and residues of the process are commonly left behind.

Aluminum (Al) is an attractive choice since it has a relatively low acoustic attenuation coefficient and is very easy to pattern. The only problem with Al is the reactivity with wide range of acids and bases. For example most solution used for patterning ZnO and AlN attack Al as well.

Molybdenum (Mo) is one of the best choices if the low acoustic loss and high acoustic velocity is of high concern [61]. It is also a suitable seed layer for deposition of AlN [62] and therefore, is used for all the AlN devices fabricated in this dissertation. The only disadvantage of using molybdenum is that it can get oxidized at relatively low temperature [63] and careful consideration should be devoted to the design of process

steps involving oxygen (e.g. oxygen plasma clean) after exposing the bottom molybdenum layer.

#### 4.1.2 ZnO Sputtering

Next step is piezoelectric film sputtering (Fig. 4.1b). The piezoelectric thin-film used for most of the devices in this work is ZnO. Although AlN devices are also fabricated in this work, the deposition of the AlN film was carried out by an outside supplier and no characterization on the deposition condition was performed. The ease of access to the deposition tool in Georgia Tech cleanroom was the main reason for using ZnO as primary piezoelectric film deposited.

In this work ZnO is sputtered in a PVD 75 RF magnetron sputtering tool. The sample is mounted on a heated plate which is hanging from the top of the chamber. A 99.99% pure ZnO target is used and sputtered material travels from the target located underneath the sample to hit the sample. Argon and Oxygen are used with approximately equal flow rate in the chamber and the chamber is pumped down to  $<5\mu\text{Torr}$  before opening the gas valves. Sputtering parameters which are kept constant throughout our experiments are listed in Table 4.1.

TABLE 4.1: LIST OF PARAMETERS THAT ARE KEPT CONSTANT FOR ALL EXPERIMENTS REGARDING CHARACTERIZATION OF ZnO SPUTTERING

Sputtering parameter	Pressure	Ar/O <sub>2</sub> flow	RF power	Target to sample distance
Value	6mTorr	52/58 sccm	120Watts	7-10cm

The bottom seed layer and the deposition temperature are varied in order to find the suitable bottom metal electrode that will eventually be utilized in the resonator structure. The first experiments are performed to compare the quality of ZnO sputtered on



gold, aluminum, molybdenum and platinum. The thickness of the metal film is approximately 1000Å and is deposited on a silicon wafer using e-beam evaporation. X-ray diffraction (XRD) measurement is performed on the samples after depositing ZnO to study the crystallographic structure of the thin film.

The Bragg diffraction intensity peak ( $2\theta$  scan) is monitored to determine the orientation of crystalline structure. The full width half maximum (FWHM) of the  $2\theta$  peak is a measure of grain size for a polycrystalline film. The difference in angular position of the XRD peak measured for the thin film and the powder sample is a measure of lattice stress. The x-ray rocking curve (Omega scan) is used to identify the uniformity of orientation of crystallites within a particular angular distribution. The FWHM angle measured from rocking curve is the measure of how closely the grains of a certain orientation are aligned to the substrate normal [64].

ZnO and AlN belong to the 6mm (wurtzite crystal structure) symmetry class and they both tend to grow with a c-axis normal orientation. Therefore, (002) Bragg diffraction peak is dominant in the  $2\theta$  scan. The (002) Bragg angle for ZnO is  $\sim 34.4^\circ$  (Cu  $K\alpha_1$  wavelength) [65].

$2\theta$  XRD scans measured from samples with sputtered ZnO on different bottom seed layer are overlapped in Fig. 4.2. The deposition temperature is kept constant at  $250^\circ\text{C}$  during the sputtering process and the parameters shown in Table 4.1 are employed. Results indicate that normal c-axis is the predominant orientation of the grains for the samples and the ZnO film on gold has the highest uniformity.

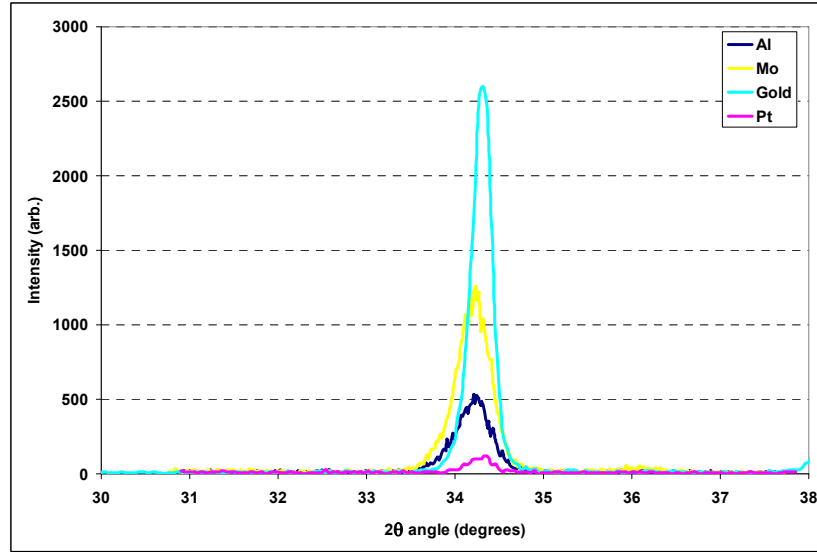


Figure 4.2: XRD  $2\theta$  curves measured from ZnO samples sputtered on different metal layers

According to the results presented in Fig. 4.2 it was concluded that gold is the preferred bottom electrode layer. However, we also found out that ZnO grows on amorphous silicon dioxide with c-axis grain orientation uniformly aligned to the substrate normal [66]. Therefore, for applications where a specific bottom electrode layer is preferred while that layer is not necessarily a suitable seed layer, depositing a very thin oxide layer (<100nm) on top of the electrode could be a practical solution. This technique was tried on Pt and the XRD measurement was repeated (Fig. 4.3). The sample temperature was increased to 350°C as it was also noticed that increasing the temperature will improve the uniformity of the (002) ZnO grains sputtered on oxide. The same trend was not observed while Pt was used as the seed layer with no buffer oxide layer.

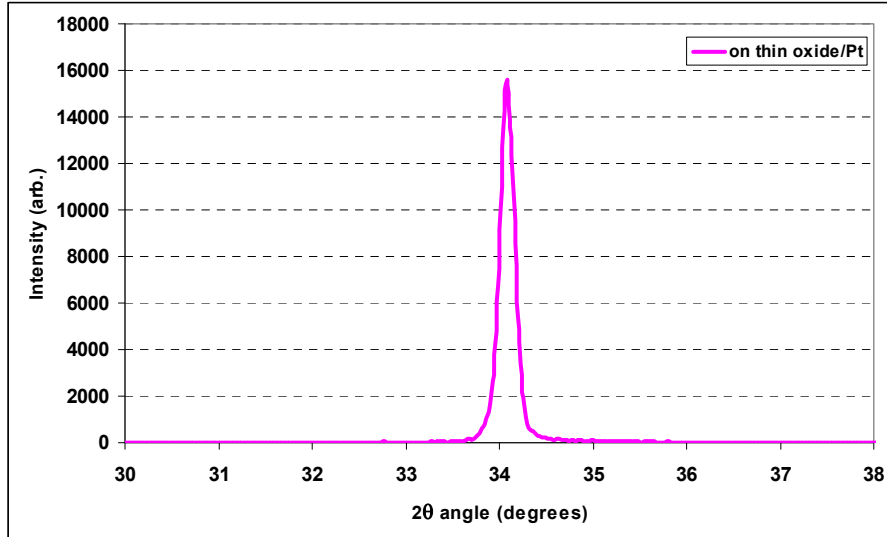


Figure 4.3: XRD  $2\theta$  curve measured from ZnO sample sputtered on oxide-covered Pt.

The peak intensity is significantly improved compared to the peak measured for the ZnO film deposited directly on Pt layer. The rocking curve measured from the ZnO film sputtered on oxide-covered Pt bottom layer is presented in Fig. 4.4. The FWHM angle is approximately 4 degrees which indicates a relatively small angular distribution of c-axis grains around the normal to the surface.

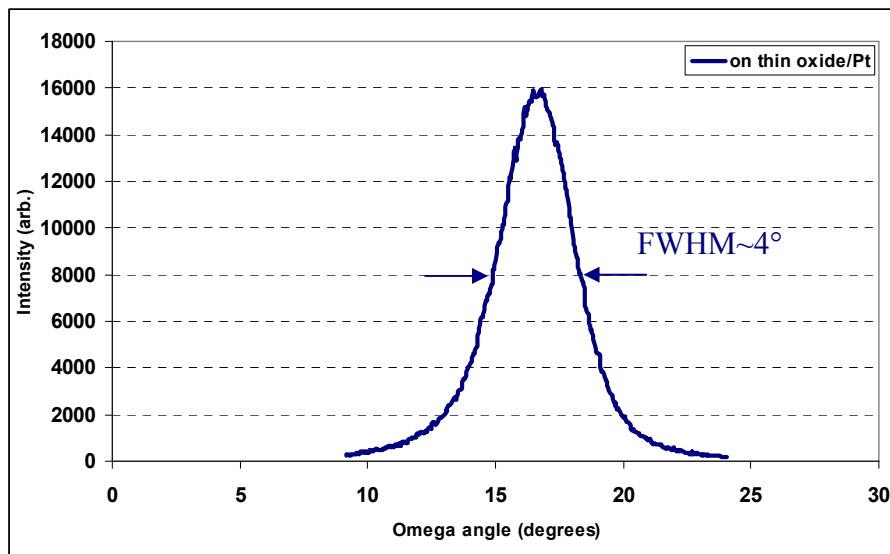


Figure 4.4: XRD rocking curve measured from ZnO samples sputtered on oxide-covered Pt

The best quality ZnO film obtained in our experiments was sputtered on a Ti-coated Gold seed layer. A very thin layer of Ti (75nm) was evaporated on gold in order to take advantage of the similarity of crystal structures in Ti and ZnO. Measured rocking curves from ZnO sputtered on gold and Ti-coated gold are shown in Fig. 4.5.

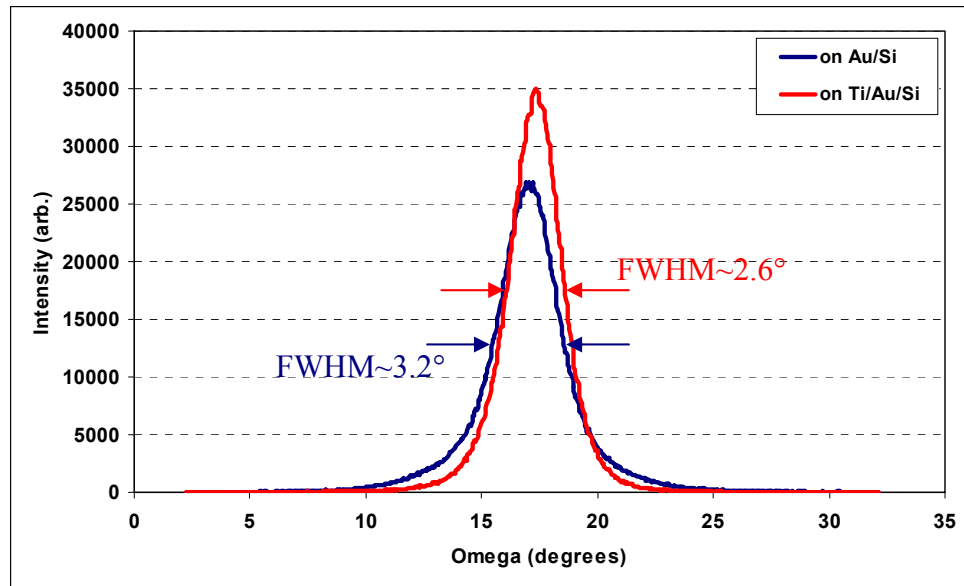


Figure 4.5: XRD rocking curves measured from ZnO samples sputtered on gold and Ti-covered gold layers

As seen, the FWHM is smaller for the sample with Ti coating and the peak intensity is higher. Ti can not be used as the bottom electrode since it has a very poor conductivity.

### 4.1.3 Top Electrode Layer Deposition

The top metal electrode is also e-beam evaporated on the wafer and patterned using lift-off process (Fig. 4.1b). Aluminum is used for all the devices fabricated in this dissertation as the top electrode. Since ZnO chemically reacts with many acidic and basic solutions extra care should be taken for the lift-off procedure. Acetone can be safely used in the ultrasonic agitator bath to perform the lift-off whereas, common photoresist

removers such as Shipley 1112A attack ZnO layer and are not recommended for the process. It should be noted that after the deposition of ZnO in all the lithography steps, utilized solutions including photoresist developers and removers should be chosen carefully.

#### **4.1.4 Bottom Electrode Access Etching**

In this step openings are chemically etched in the piezoelectric layer to access the bottom electrode pads designed for connection to the high frequency probes or wire-bonds (Fig. 4.1c). The wet etching solution is chosen based on the piezoelectric material and the bottom electrode metal. In case of ZnO sputtered on gold any of numerous ZnO acidic etchants would work fine. Diluted acetic acid solution (1:150) was usually used in our experiments. For devices in which AlN was used as the piezoelectric thin-film and Mo was used as the bottom electrode heated 1112A remover could be used to remove the AlN layer. In this case a thin oxide hard mask should be deposited and patterned before wet etching the etch pits. The oxide mask can be removed in BOE later on since BOE does not attack either AlN or Mo.

#### **4.1.5 Device Structure Etching**

Next step is to etch the stack of piezoelectric on silicon to define the resonator structure (Fig. 4.1c). A single photoresist mask will be used for etching the stack and the lithography is performed only once. After developing the photoresist (1813) a diluted acetic acid is used to chemically etch the ZnO film. This step should be accurately timed since excessive undercut may occur otherwise. In case of AlN film, dry etching in inductively-coupled plasma (ICP) etcher is preferred. Anisotropic etching of AlN is possible in low pressure (5mTorr) chlorine plasma. However, photoresist mask is not

useful for etching AlN in ICP since the mask will be eroded very quickly and the layers underneath will be exposed. Instead, an oxide hard mask should be employed for dry etching of AlN. It should be noted that the residues of the oxide hard mask can not be removed in BOE if the top metal electrode is made of Aluminum. BOE etches away Al and therefore Mo is a better alternative for these devices. If Al is preferred because of ease of use and application, then the top electrode deposition can be postponed to after AlN dry etching step (the processing steps should be reordered).

After etching the piezoelectric film the silicon device layer will be etched in SF<sub>6</sub> plasma using Bosch recipe [67]. An SOI compatible recipe is used on a STS ASE tool to prevent the notching effect on the oxide interface [68]. The buried oxide layer will be kept intact to be used as an etch stop for the back side silicon etching step performed next.

#### **4.1.6 Back-Side Etching**

The last lithography step in the process flow is performed on the back side of the SOI wafer to open release holes underneath the resonator from the backside (Fig. 4.1d). During the backside lithography and the consecutive etching the top side of the wafer can be protected by a layer of photoresist covering the surfaces of the wafer. The photoresist used for this step is SPR 220 spun at 2000 rpm which results in a mask thick enough (>8μm) for etching through the thick handle wafer. The process wafer is flipped and mounted on another oxide-covered handle wafer. STS ASE is used to etch the backside silicon and the buried oxide layer will be the etch stop for the etching process. After etching through the silicon layer the final step is to remove the oxide in order to release the device. The oxide can be removed in an inductively coupled plasma (ICP) etcher

either from the top or the bottom. By etching the oxide layer from the top the oxide layer under the resonant structure will be part of the device body and can be effective in reducing the temperature coefficient of frequency (TCF) as it will be seen later on. In this case the top side etching mask should not be removed after etching the silicon layer. This is only possible if both top and bottom patterning steps are done back to back with no processing step performed in between. After the two lithography steps are done the stack etching is performed and backside etching is done right after. Then the wafer is flipped over again and the oxide is etched in an ICP tool from the top while the top mask is still intact.

At the end the photoresist residues are etched in an oxygen plasma cleaning chamber and the devices are ready for measurement. Devices fabricated on a layer of nano-crystalline diamond deposited on silicon are also fabricated in this dissertation and the details of the fabrication process will be discussed in Chapter 7.

## 4.2 Effective Coupling Factor

In order to gauge the quality of the ZnO film sputtered in Georgia Tech. fabrication facilities, frequency response measured from a typical device is used to extract the effective coupling factor in a TPoS resonator. It should be noted that this value is correlated to the material coupling factor [69] and not equal to that.

The component values in the equivalent circuit of Fig. 2.10 are extracted by curve fitting the measured response with the simulated response (Fig. 4.6):

$$R_m = 190\Omega, \quad L_m = 786.6\mu\text{H}, \quad C_m = 3.6\text{fF}, \quad C_0 = 0.25\text{pF}, \quad C_f = 10\text{fF}$$

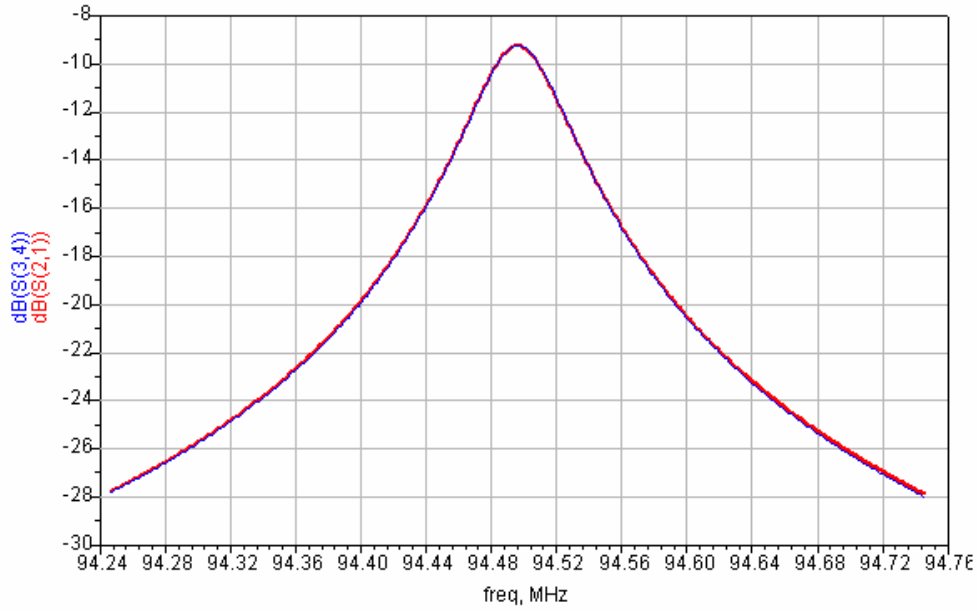


Figure 4.6: Overlapped simulated (red-line) and measured (blue-line) frequency responses from a 94.5MHz ZnO-on-Silicon resonator.

The effective coupling factor can be calculated by using these values in equation

(3.10):

$$k_{eff}^2 \approx \frac{C_m}{C_0} = \frac{3.6 \text{ fF}}{250 \text{ fF}} = 0.014$$

This is a moderate coupling factor considering that the maximum coupling factor for in-plane ZnO resonators (no substrate) can be as high as ~6% [70].



## CHAPTER 5

### THIN FILM PIEZOELECTRIC-ON-SUBSTRATE OSCILLATORS

In this chapter the application of lateral bulk acoustic thin-film piezoelectric-on-substrate (TPoS) resonators in high frequency reference oscillators is studied. High-frequency low-motional-impedance TPoS resonators are designed and fabricated in two classes of high-order and coupled-array lateral-extensional. Devices of each class are used to assemble reference oscillator circuits and the performance of the oscillators are measured and discussed. Since the motional impedance of these devices is small the transimpedance amplifier (TIA) in the oscillator loop is reduced to a single active component (one transistor) and 3 resistors, which is very power-efficient. The lowest reported power consumption is  $\sim 350\mu\text{W}$  for an oscillator operating at  $\sim 106\text{MHz}$ . A passive temperature compensation method is also utilized by including the buried oxide layer of the SOI substrate in the structural resonant body of the device, and a very small ( $-2\text{ppm}/^\circ\text{C}$ ) temperature coefficient of frequency (TCF) is obtained for an 82MHz oscillator.

#### 5.1 Introduction

Micromachined high- $Q$  frequency-selective components with small form-factor are in high demand to replace quartz crystal resonators in temperature-stable, low-phase noise oscillator applications. Significant progress has been made in developing oscillators that utilize silicon-micromachined capacitive resonators with  $Q$  values comparable to that of a quartz resonator [71,72]. However, high frequency capacitive resonators require relatively high dc polarization voltages (5-20V) for operation, which complicates the

design of the oscillator circuit in today's low-voltage CMOS processes. Moreover, the motional impedance of capacitive resonators is much larger than that of a quartz resonator, and their power handling is lower. These resonators are usually operated at low pressures (mTorr regime), which makes their packaging process costly and challenging. Also, the temperature compensation techniques demonstrated so far lose efficiency at high frequencies.

The thin-film piezoelectric-on-substrate (TPoS) resonator technology has the potential to address some of the issues mentioned above. The piezoelectric transduction provides for very small motional impedance that eliminates the need for multiple gain stages to sustain oscillation. Moreover, the use of low-loss substrate (e.g. single crystal silicon) provides for relatively high quality factor values in air. Therefore, vacuum packaging is not necessary which makes the technology more cost-competitive. Application of the substrate also improves the power handling of the resonator which directly affects the far-from-carrier phase-noise characteristic of the oscillator built based on these devices. Another important advantage of TPoS resonators over capacitive devices is that no bias voltage is necessary for their operation. This is a very attractive feature considering the low operating voltage of the modern integrated circuits.

In this chapter, TPoS-based oscillators are presented at IF to UHF frequencies. An arraying technique for TPoS resonators is introduced and evaluated in comparison with the high-order resonators. The temperature coefficient of frequency (TCF) of TPoS resonators is also shown to be reduced by incorporating the buried oxide (BOX) layer of the SOI substrate in the resonator structure. The large positive TCF of the oxide layer [73] compensates for the negative TCF of the rest of the material in the resonant structure

and enables near-zero-TCF devices, provided the thickness of the layers is adequately controlled.

## **5.2 Resonator Design**

A TPOs resonator is comprised of a thin-film piezoelectric layer sandwiched between two metallic electrodes stacked on top of a relatively thick substrate layer. The substrate layer which usually comprises a large portion of the resonant structure is chosen from low acoustic loss material such as single crystal silicon or nano-crystalline diamond (NCD). The metal electrodes are patterned to match with the strain field in a targeted resonance mode-shape. With a careful electrode design, the coupling factor is optimized, and the motional impedance of the resonator is minimized. For the resonators used in this chapter the top electrode is split into two electrically isolated electrodes. The bottom electrode covers the entire resonant structure where as it can optionally be patterned to match the shape of the top electrode.

### **5.2.1 High-Order Design**

In order to excite high-order lateral-extensional mode-shapes of a rectangular plate supported in the middle from both sides, the optimum top electrode pattern resembles an interdigitated transducer (Fig. 5.1a) [42]. This design matches the periodic strain field pattern of the structure excited in its high-order lateral-extensional resonance mode. The third-order mode-shape of a rectangular plate simulated in FEMLAB is shown in Fig. 5.2. The color code in this picture demonstrates the strain field. Bluish colors present areas under compressive strain and reddish colors are representative of the tensile strain. At resonance opposite charges are accumulated on the two electrodes because the strain polarity is changing from one finger to the other. Therefore, signal polarity is

reversed at resonance. It is worth mentioning that the same electrode pattern can also excite the fundamental resonance mode of the same structure where strain field is uniform across the whole structure. However, in the following sections we will show that the sustained oscillation resonance mode can be selected between the two modes without the need for any mode-suppression circuitry.

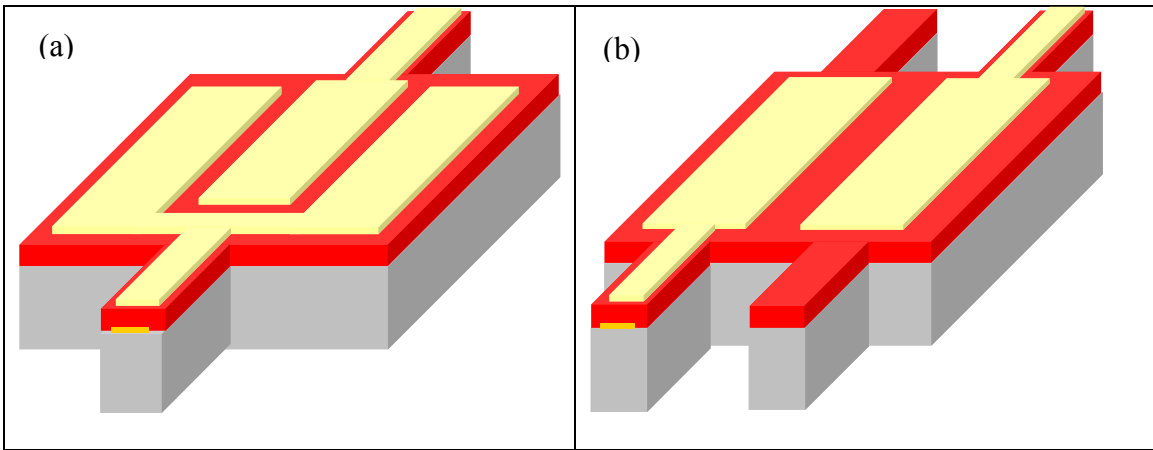


Figure 5.1: Schematic viewgraphs of (a) a third-order and (b) a two-resonator coupled array TPoS resonator.

### 5.2.2 Arrayed Design

Although the motional impedance of the high-order TPoS resonators can be improved by utilizing high-order resonators, increasing the resonance order gives rise to some issues. The wide freestanding resonant structures supported by small beams at nodal points (Fig. 5.1a) are not constrained enough to suppress excitation of unwanted resonance modes. To further decrease the impedance of the resonator either length or the resonance mode-order of the resonator is increased. This, in turn, raises the number of spurious modes that have low motional impedance and can be detected in the frequency response.

In order to solve this problem, a coupled array of individual resonators is suggested (Fig. 5.1b). Each of these resonators is supported with a separate set of support beams, which improves the rigidity of the resonant structure and consequently suppresses the vibration amplitude of the spurious modes. The motional impedance of the resulted coupled-array resonator should ideally be inversely proportional to the number of resonators existed in the array.

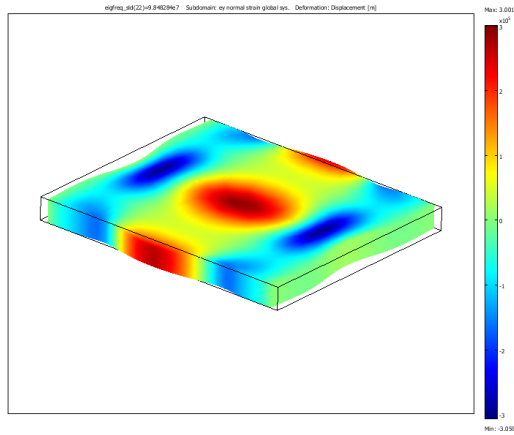


Figure 5.2: The third-order lateral extensional resonance mode-shape of a block resonator simulated in FEMLAB.

### 5.3 Frequency Response Measurement

To measure frequency response of the fabricated resonators a Karl-Suss high-frequency probe station, Cascade GSG probes, and an Agilent network analyzer (E8364) are used. A Lakeshore high-frequency vacuum probe station with heated/cooled chuck is alternatively used for carrying out the measurements in vacuum.

#### 5.3.1 High-Order versus Arrayed Design

Top-view optical viewgraphs of a third-order ZnO-on-silicon resonator and a four-resonator arrayed counterpart are shown in Fig. 5.3. These devices are fabricated on 5 $\mu\text{m}$  thick SOI substrate and the BOX layer is removed from the backside. The center-to-

center top electrode finger pitch for these devices is  $40\mu\text{m}$ . the third-order device is  $160\mu\text{m}$  long where as the arrayed resonator is only  $60\mu\text{m}$  long.

A typical measured frequency response plot of a third-order ZnO-on-silicon resonator is shown in Fig. 5.4. The wide-span (100MHz) frequency response of a 12-resonator coupled-array is demonstrated in Fig. 5.5 along with an SEM of the fabricated device.

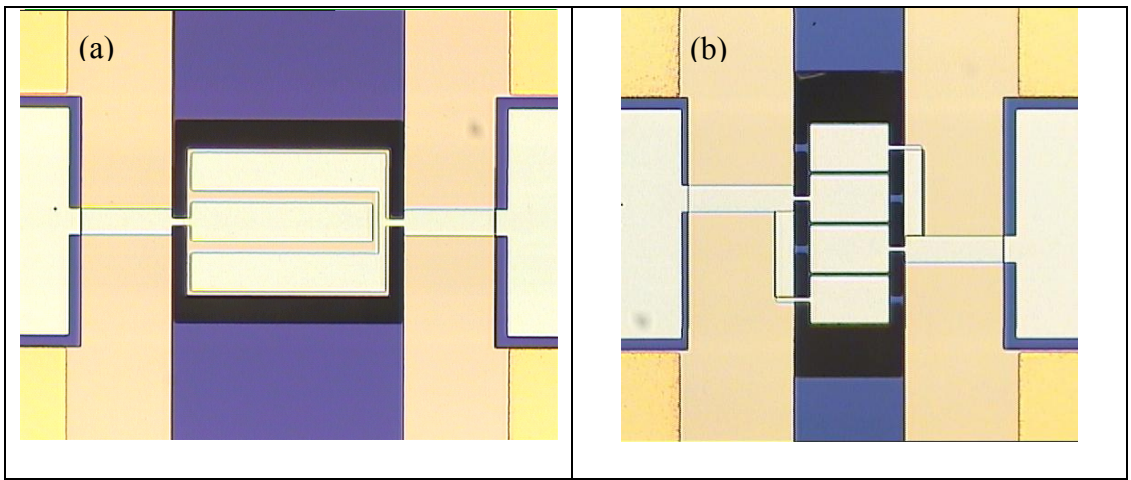


Figure 5.3: Optical viewgraphs of (a) a third-order and (b) four-resonator coupled array TPoS resonators.

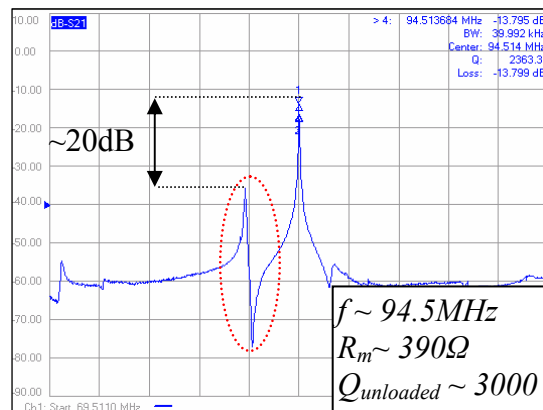


Figure 5.4: The frequency response plot of a third-order TPoS resonator.

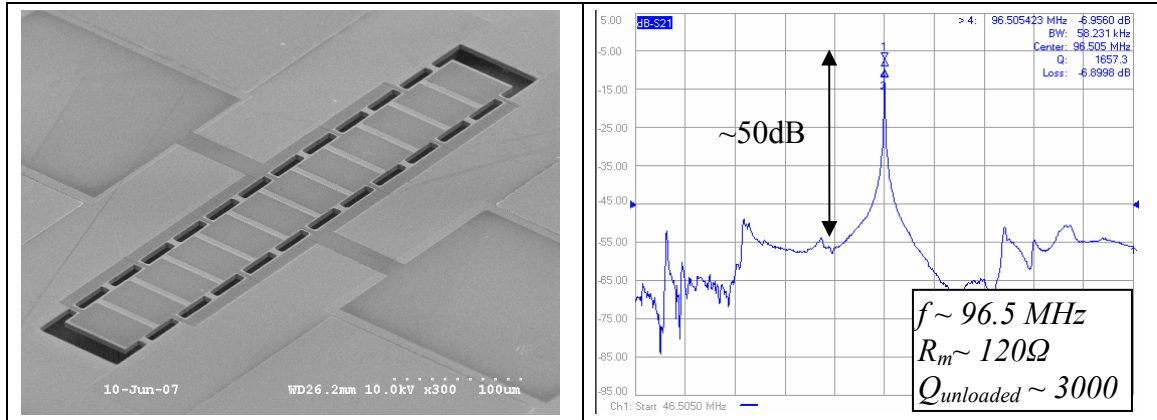


Figure 5.5: The wide-span (100MHz) frequency response and the SEM of a 12-resonator coupled array.

Unlike the third-order device there is no strong spurious resonance peaks detected in the 100MHz vicinity of the primary resonance peak. Measured frequency responses of arrayed devices with 4, 6, and 12 resonators located on the same die of a processed wafer are shown in Fig. 5.6.

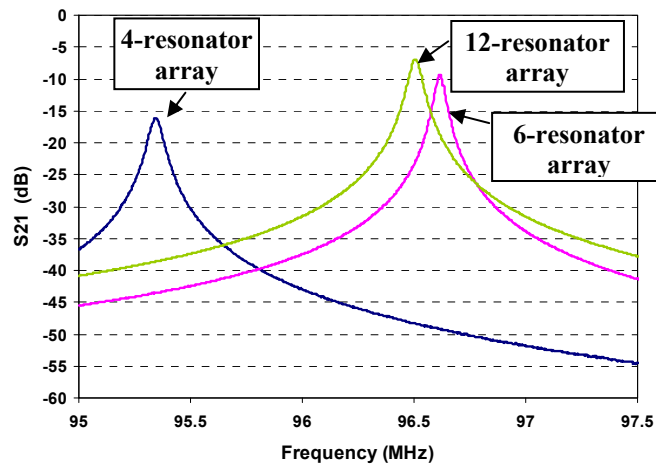


Figure 5.6: Frequency response plots of 4, 6, and 12-resonator coupled arrays.

The metal electrode finger width for the 4-resonator array is different than the other two resonators and that is the reason for observing relatively large frequency discrepancy. The motional impedances are  $\sim 550\Omega$  for the 4-resonator,  $210\Omega$  for the 6-resonator and  $110\Omega$  for the 12-resonator array. The predicted inverse proportionality of

the motional impedance with the number of resonators in the array holds with good precision for the two larger devices. These results confirm that the motional impedance of the coupled array device can be systematically decreased while avoiding spurious modes.

### 5.3.2 Temperature-Stable Resonators

A  $2\mu\text{m}$  thick SOI substrate with  $2\mu\text{m}$  of BOX layer is used as the starting substrate for the fabrication of temperature-stable resonators. For these resonators the BOX layer is etched in the ICP from the top as explained in chapter 4 and therefore, a  $\sim 2\mu\text{m}$  oxide layer is included in the stack of the resonant structure. A typical frequency response plot measured from a 12-resonator arrayed device fabricated on this substrate is shown in Fig. 5.7.

Even though the dimension of the device is the same as the device measured in Fig. 5.5, the resonance frequency is decreased from  $\sim 95\text{MHz}$  to less than  $82\text{MHz}$ . This is a direct result of including the oxide layer in the resonant structure. The elastic modulus of oxide ( $\sim 75\text{MPa}$ ) [74] is lower than the elastic modulus of silicon ( $\sim 150\text{MPa}$ ) and therefore the resonance frequency is lower.

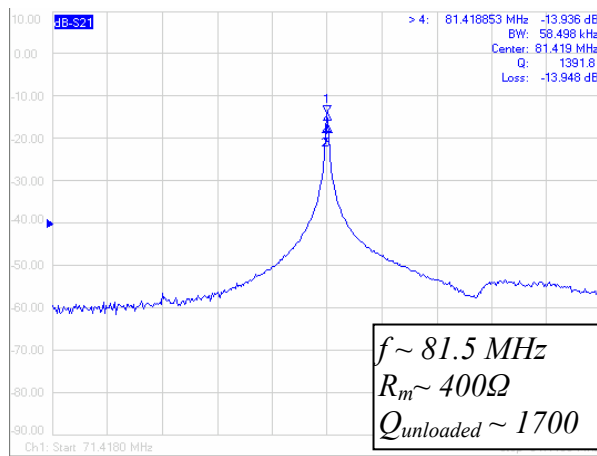


Figure 5.7: The frequency response of a temperature-compensated 12-resonator coupled array.



### 5.3.3 AlN-on-Silicon Resonators

AlN-on-silicon resonators are fabricated on a 10 $\mu$ m SOI wafer, where the thickness of the AlN layer is 1 $\mu$ m. The frequency responses measured from the same third-order resonator with 40 $\mu$ m finger pitch size is shown in Fig. 5.8. For this device the resonance frequency is increased compared to the ZnO-on-silicon counterpart. This is mostly due to the fact that the acoustic velocity in the AlN film (11400m/s) is greater than the acoustic velocity in ZnO (6400m/s) [75].

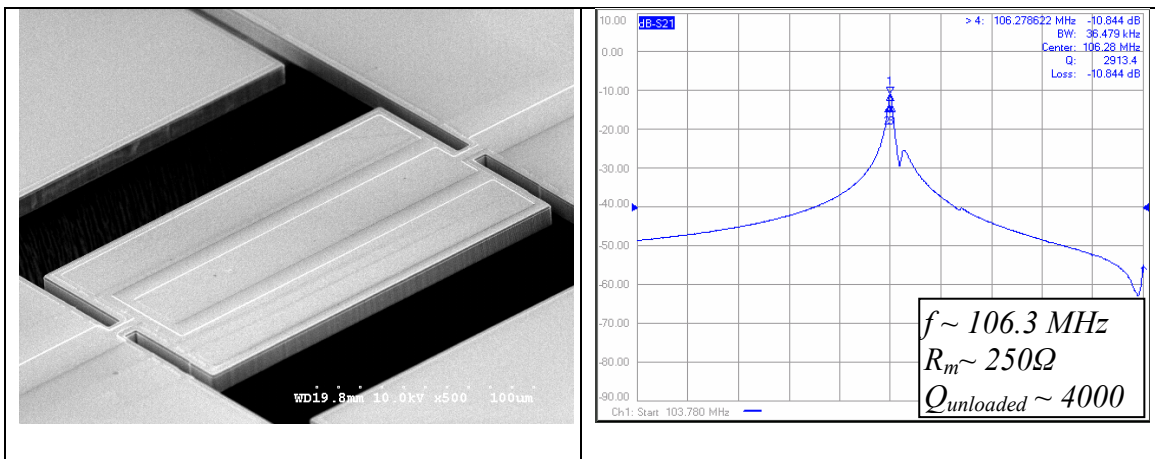


Figure 5.8: The frequency response and the SEM picture of a third-order AlN-on-silicon resonator.

As explained before the same top electrode pattern can excite the fundamental extensional mode of the rectangular plate and the response plot is shown in Fig. 5.9a. The resonance frequency ( $\sim 35.5$ ) is approximately one third of the third-order mode as expected and the motional impedance is not smaller even though the quality factor is larger. The unloaded quality factor of the resonance peak shown above is measured to be  $\sim 17000$  in vacuum (Fig. 5.9b). The motional impedance of the device is also reduced in vacuum which is inversely proportional with the increase in  $Q$ .

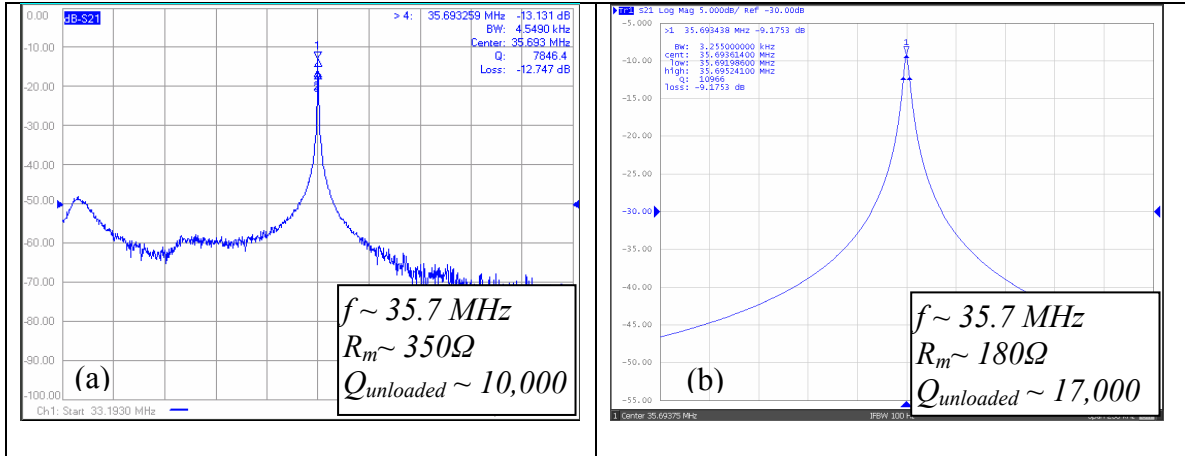


Figure 5.9: The frequency response of the third-order resonator at fundamental mode; a) in air b) in vacuum.

The motional impedance of high frequency high-order TPoS resonators can be further reduced by increasing the order number. The frequency response shown in Fig. 5.10 is measured from a 9<sup>th</sup> order 208MHz device with a 20 $\mu\text{m}$  finger pitch size. The impedance is only  $\sim 70\Omega$  and the unloaded  $Q$  is  $\sim 6000$  in air. This will result in an excellent close-to-carrier phase noise for the oscillator assembled using this device while no vacuum packaging is required.

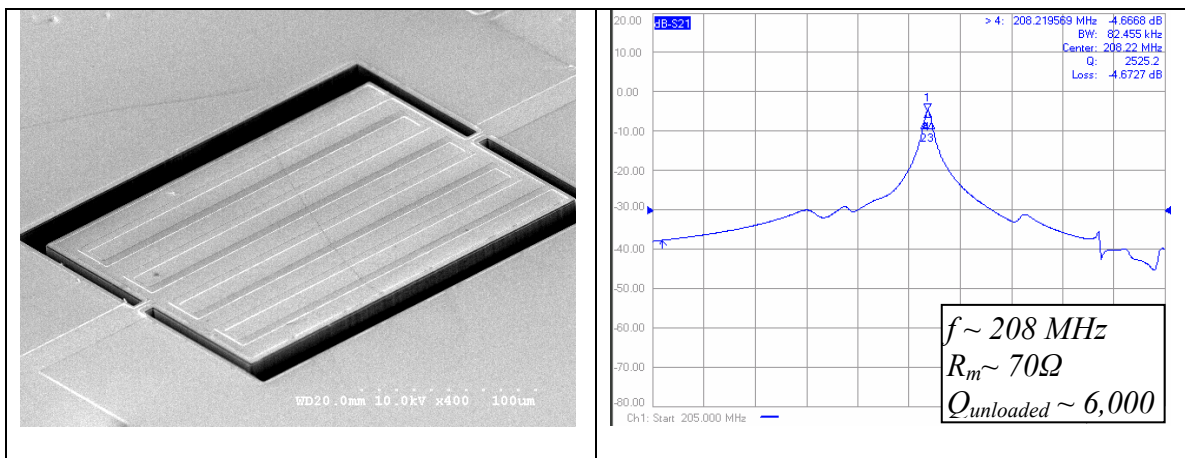


Figure 5.10: The SEM and the frequency response of a 9<sup>th</sup>-order AlN-on-silicon resonator with a 20 $\mu\text{m}$  finger pitch.

Higher frequency resonators are enabled by further reducing the top electrode finger pitch size. The resonance frequency plot shown in Fig. 5.11 is measured from a 9<sup>th</sup> order AlN-on-silicon resonator. The center frequency is at ~500MHz with measured unloaded  $Q$  of ~5800 in air. The motional impedance of the resonator is ~150 $\Omega$  which makes the device very attractive for oscillator application.

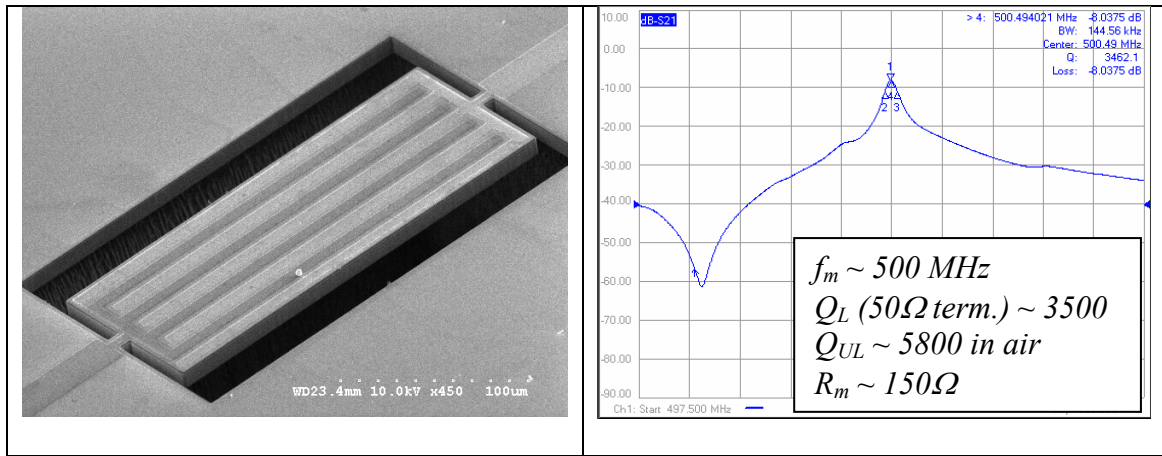


Figure 5.11: The SEM and the frequency response of high-order 500MHz AlN-on-silicon resonator.

#### 5.4 Linearity Measurement

Figure 5.12a shows the recorded frequency response of the third-order resonator (ZnO-on-silicon) with excitation source power ranging from -5dBm to 15dBm. The 1dB compression point is measured at 15dBm. For a 12-resonator device however, the power handling is significantly improved, showing only 0.2 dB compression at 15dBm of input power, as illustrated in Fig. 5.12b. This improvement can be related to the increased actuation area on the coupled array resonator (larger resonant structure).

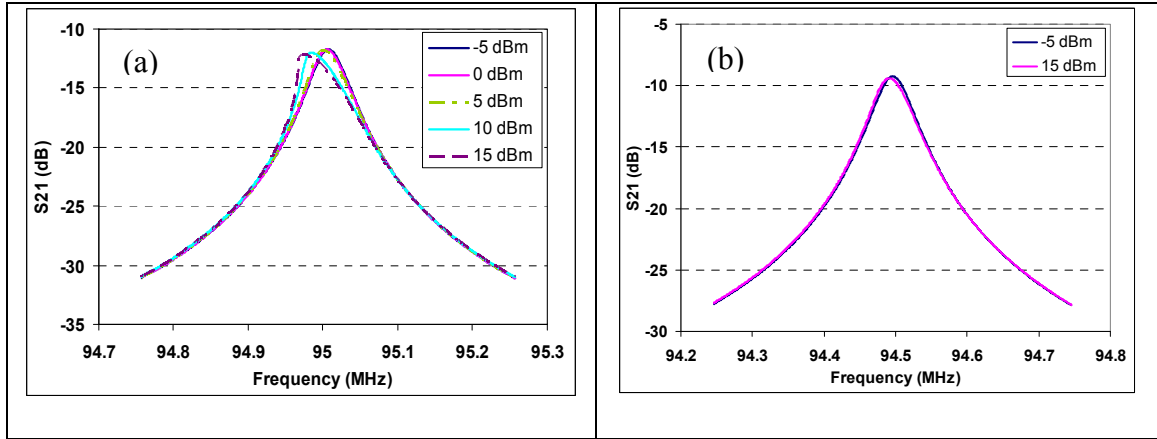


Figure 5.12: The nonlinearity measurement for a) third-order TPoS resonator and b) 12-resonator coupled array TPoS resonator.

Next set of experiments demonstrate the enhanced power handling in a TPoS resonator compared to the same device after etching the silicon layer in the stack. Figure 5.13a shows overlapped frequency response plots of an AlN-on-silicon device excited in its fundamental mode while the network analyzer output power is varied from -15dBm to 10dBm. As seen, a very minute change is observed in the resonance peak. After performing this measurement the silicon device layer is etched away from the backside in an ICP tool. Frequency responses of the device are measured again for several applied input power and overlapped in Fig. 5.13b. Measured  $Q$  is reduced to  $\sim 740$  and the resonance peak is deformed starting from  $-10$ dBm of applied power.

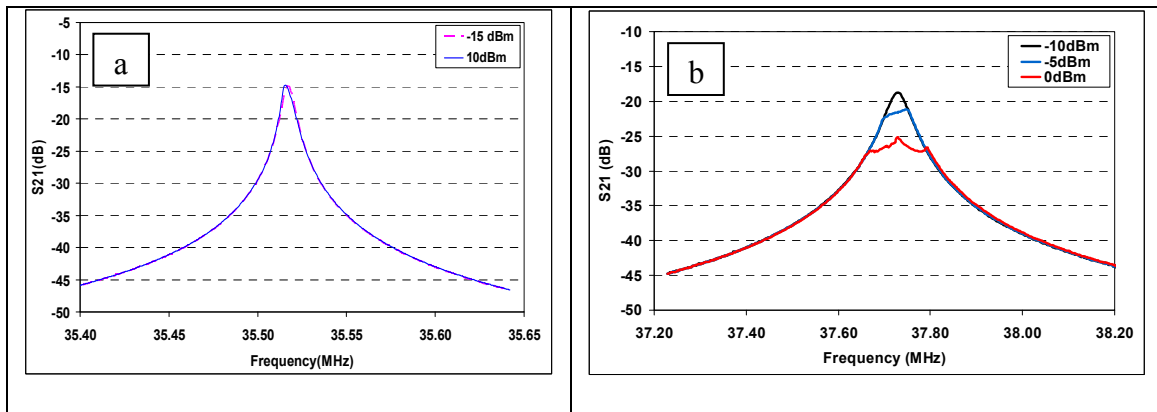


Figure 5.13: The nonlinearity measurement for an AlN-on-silicon resonator a) before, and b) after etching the structural silicon substrate.

As expected, the resonance frequency after etching the silicon layer is slightly increased, since the acoustic velocity in AlN is higher than acoustic velocity in silicon. The fact that after etching the silicon layer the resonator exhibit highly nonlinear and the measured quality factor of the resonator is reduced can clearly confirm the advantages of including the silicon substrate in a lateral-extensional resonator.

### **5.5 Oscillator Design**

The resonators presented in this chapter are utilized to make oscillators. The oscillation sustaining circuit is very simple. The low motional impedance of the resonator reduces the number of required gain stages to sustain oscillation. The excellent power handling of these devices improves the far-from-carrier phase noise of the oscillator and eliminates the need for an automatic level control (ALC) circuit. The ALC circuit is customary to operate capacitive resonators in the linear region [72] and by eliminating it total power consumption of the oscillator is further improved. In addition, the coupled array resonators are free of spurious modes, eliminating the possibility of locking to an undesired mode.

In order to sustain oscillation, the amplifier should create 180 degrees of phase-shift. This is because the output signal of the coupled-array and the high-order resonator is 180 degrees out-of-phase relative to the input signal. Therefore as shown in Fig. 5.14 the transimpedance amplifier (TIA) can be reduced to a single NPN transistor in common-emitter configuration. An emitter degeneration resistor is used to improve the linearity while maintaining sufficient voltage headroom for oscillation. The feedback resistor eliminates the need for separate biasing network and improves the overall phase-noise performance of the oscillator.

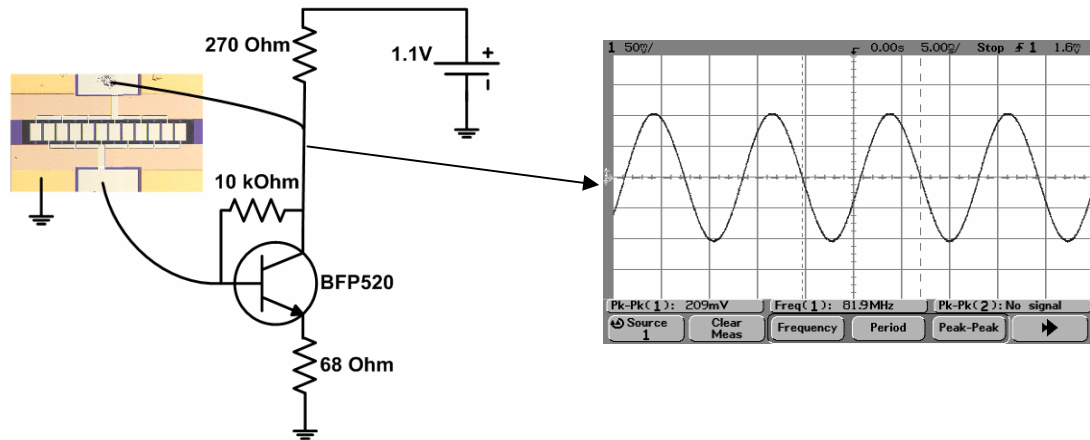


Figure 5.14: The schematic circuit diagram and output waveform of the single-transistor oscillator.

The first device utilized in the oscillation loop is the temperature-compensated 12-resonator coupled array. The phase noise of the oscillator is measured using an Agilent E5500 phase noise measurement system and is shown in Fig. 5.15 (after buffering the output signal). A close-to-carrier phase noise of  $-72\text{dBc/Hz}$  at  $1\text{kHz}$  offset and a phase noise floor of  $-137\text{dBc/Hz}$  are measured for the oscillator.

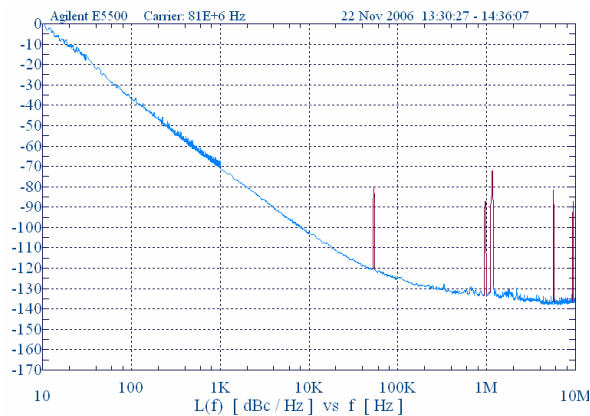


Figure 5.15: The measured phase-noise of the coupled-array temperature-stable oscillator.

The TCF of the oscillator is also measured in an environmental chamber and the result is plotted in Fig. 5.16.

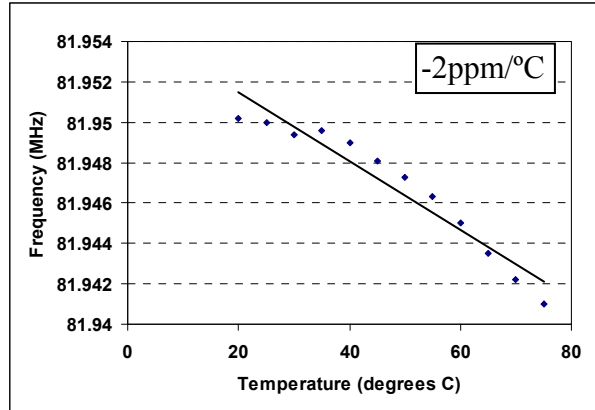


Figure 5.16: The measured TCF plot of the temperature-stable TPoS oscillator

The next oscillator is based on the third-order AlN-on-silicon resonator of Fig. 5.8. To study the effect of sustaining circuit this resonator was tested with two different circuits. One circuit is the simple single-transistor design of Fig. 5.14 and the other is an amplifier designed and fabricated in 0.18 $\mu\text{m}$  CMOS (Fig. 5.17) [76]. The sustaining amplifier consists of a transimpedance amplifier with tunable gain and two subsequent voltage amplifiers. The gain tuning is achieved by changing the resistance of an NMOS resistor. The reason behind incorporating two gain stages is to satisfy Barkhausen's phase criterion for oscillation. In addition to that, adding the second voltage gain stage helps relaxing gain constraints on the first gain stage; thereby, reducing the power consumption. Due to large power-handling of these resonators ( $> 5\text{dBm}$ ), automatic level control (ALC) is not necessary.

The measured phase noise densities of the two oscillators at the same frequency are plotted in Fig. 5.17. More than 10dBc/Hz improvement in the phase noise of the CMOS oscillator at all frequencies emphasizes the effect of the sustaining circuit and the applied signal power on the oscillator performance.

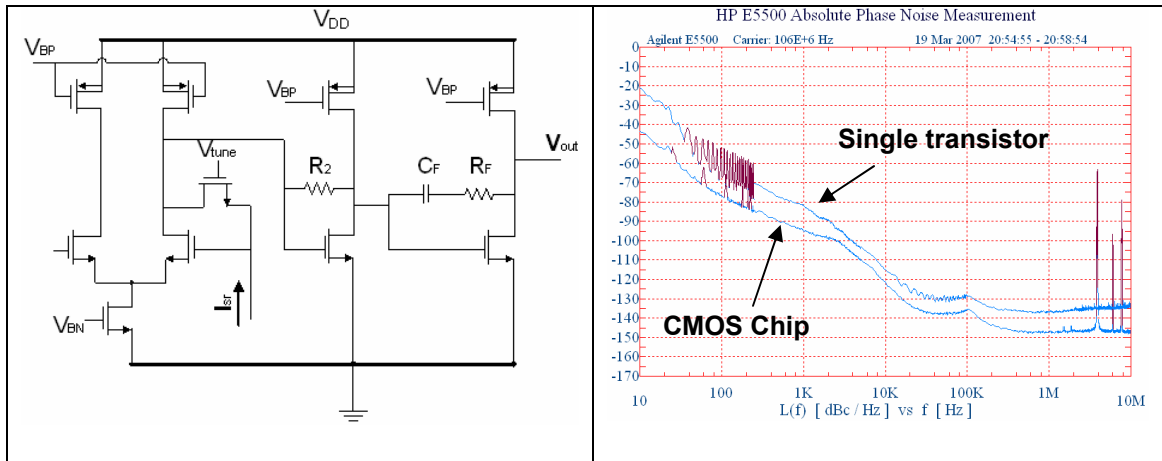


Figure 5.17: The schematic diagram of the designed CMOS TIA and the phase noise plots measured from the oscillators based on the single transistor and the CMOS amplifiers.

Finally the phase noise of an oscillator built based on the 208MHz AlN-on-silicon resonator of Fig. 5.13 is shown in Fig. 5.18. For this oscillator the above CMOS sustaining circuitry is utilized. The measured phase-noise at 1 kHz offset is  $-95\text{dBc/Hz}$  and phase-noise floor is  $-152\text{dBc/Hz}$ . Improvement in the phase-noise floor can be explained by the low motional impedance of the resonator, and improvement in close-to-carrier phase-noise can be explained by the fact that the unloaded  $Q$  of the resonator was large and the amplifier is designed to minimize the phase-noise at high frequencies.

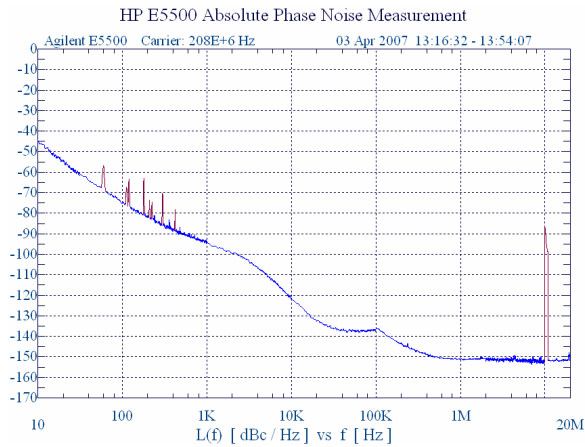


Figure 5.18: The measured phase-noise of the 208MHz oscillator.



## 5.6 Dual mode Oscillator

In this section we explore a new characteristic of high-order TPoS resonators that can be attractive for many applications such as multi-standard wireless transceivers, accurate sensors, and highly stabilized clock generators. Dual-mode excitation of quartz crystal resonators is a common practice in order to accurately compensate for environmental interferences [77]. The dual-harmonic quartz oscillators are amongst the most accurate temperature-compensated oscillators available in the market [77]. The principle of operation is based on using two different resonance modes of a single quartz plate (for example first and third harmonics [78]); since the temperature coefficient of frequency (TCF) for each mode is different, the oscillator itself can be used as a very accurate temperature sensor. However, in order to excite the crystal in two frequencies, mode-suppression circuits are required in each oscillation loop to attenuate the signal which is amplified in the other loop. It will be shown that a high-order TPoS resonator can be easily excited in two harmonic modes using a very simple scheme with minimal power consumption. This study may open new opportunities for TPoS oscillators to achieve higher level of accuracy while used as sensors and clock generators.

### 5.6.1 Operation Principle

The silicon layer in a TPoS resonator forms the main body of the resonant structure and the metal electrodes are patterned to match the strain field in a targeted resonance mode-shape. With a careful electrode design, the coupling factor is optimized, and the motional impedance of the resonator is minimized. For the resonator used in this section, the top electrode is split into two electrically isolated electrodes that resemble a three-finger interdigitated transducer (Fig. 5.1a).

This pattern is designed to match the periodic strain field pattern of a block structure excited in its third width-extensional resonance mode (Fig. 5.19a). When the resonator is excited in this mode-shape, opposite charges are accumulated on the two electrodes since the strain polarity is changing from one finger to the other. Therefore, signal phase is reversed at resonance. As mentioned before the same electrode pattern can also excite the fundamental resonance mode where strain field is uniform across the entire device (Fig. 5.19b). However, in this mode-shape the input and output signals are in-phase at resonance. This is in contrast with the operation of the other thickness-mode resonators such as quartz crystal which exhibit the same zero signal phase-shift at all modes harmonic modes.

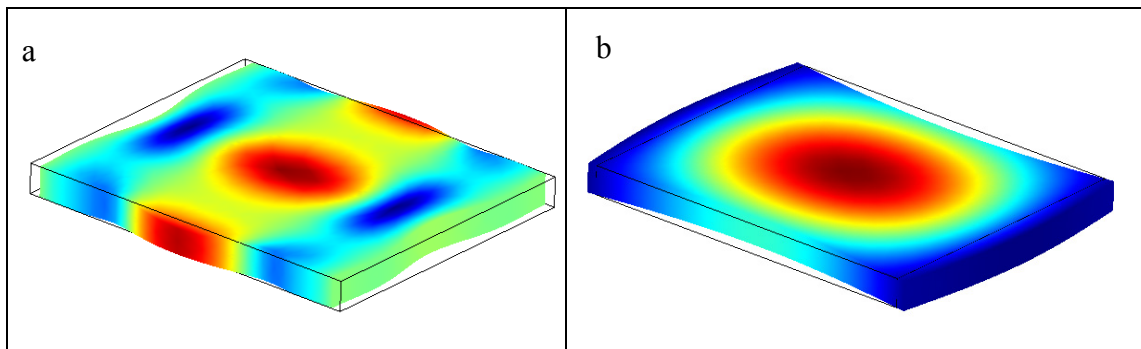


Figure 5.19: Width-extensional resonance mode-shapes of a rectangular silicon plate simulated in FEMLAB; a) third-order b) first-order.

The above-mentioned characteristic of a high-order TPoS resonator can be exploited to realize a dual-frequency oscillator with a single resonator. Fig. 5.20 shows a block diagram of the designed architecture. Each amplification stage shown in the figure introduces  $180^\circ$  of phase shift. Therefore, when only one amplification stage is included in the oscillator loop, the sustained oscillation frequency corresponds to the third-order resonance mode in which  $180^\circ$  phase-shift will be introduced by the resonator. In

contrast, if both of the amplification stages are included in the loop, the low frequency first-order mode will be sustained in which input and output signals are in-phase at resonance. In this scheme no precautions need to be taken for mode-suppression as a result of the additional phase-shift in the third harmonic.

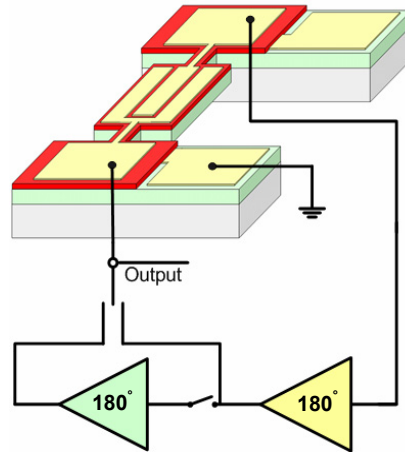


Figure 5.20: The block diagram of the architecture used to implement the dual-frequency oscillator.

### 5.6.2 Implementation and Characterization

The same resonator shown in Fig. 5.8 is used to implement the dual mode oscillator. The first- and the third-mode frequency responses of the resonator in air are presented in Fig. 5.21.

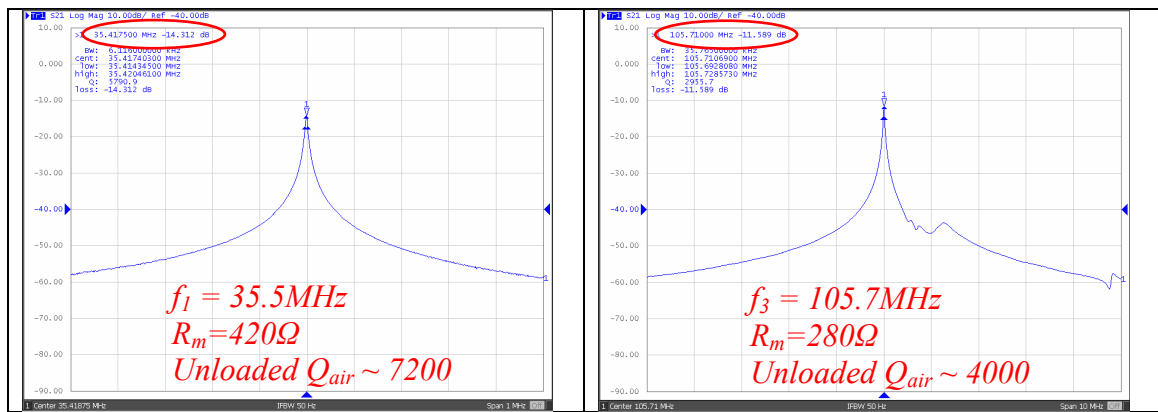


Figure 5.21: The first and the third-order frequency response of the resonator shown in the SEM of Fig. 5.8.

The measurements are repeated in vacuum and results are shown in Fig. 5.22. As expected, the measured quality factors are improved and the motional impedances are reduced, inversely proportional with the  $Q$ . However, the improvement ratio for the lower frequency mode (10100/7200) is more than what is observed for the higher frequency mode (4500/4000), which indicates that the dominant loss mechanism at higher frequencies is not air damping.

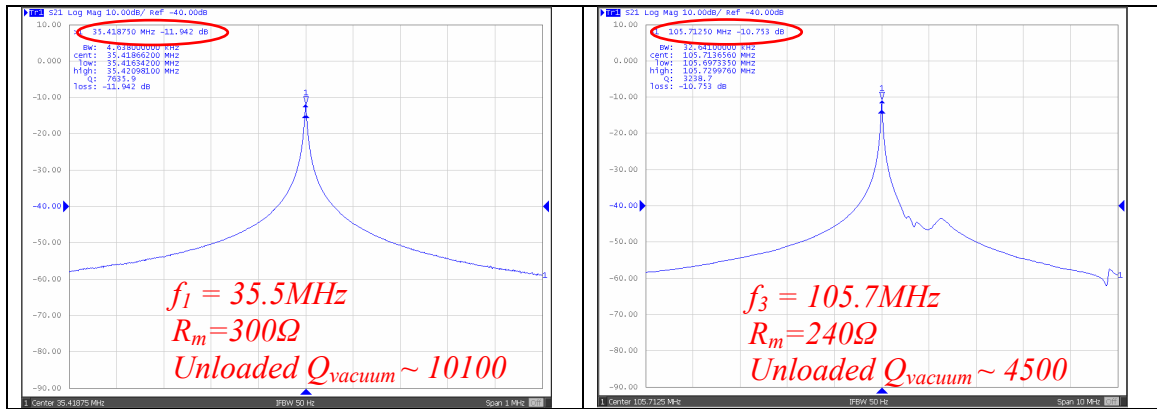


Figure 5.22: The first- and the third-order frequency response of the resonator (Fig. 5.8) in vacuum.

The frequency shift of the resonance peak with temperature for the two modes are measured and plotted as percentage normalized frequency change in Fig. 5.23. As shown, the TCF is slightly different for the two modes. This temperature characteristic is useful in a technique developed for accurate measurement of the resonator temperature [78].

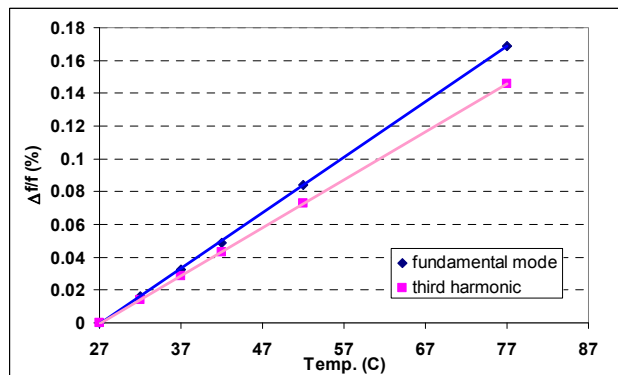


Figure 5.23: The percentage normalized frequency change with temperature for the two resonance modes. The TCF values are  $-33\text{ppm}/^\circ\text{C}$  and  $-28\text{ppm}/^\circ\text{C}$ .

### 5.6.3 Oscillator Circuit

The schematic viewgraph of the designed two-stage amplifier is shown in Fig. 5.24. The first stage is a transimpedance amplifier (TIA) comprised of a single NPN transistor ( $f_{\max} \sim 70\text{GHz}$ ) in common-emitter configuration. An emitter degeneration resistor is used to improve the linearity while maintaining sufficient voltage headroom for improved far-from-carrier phase-noise. The feedback resistor ( $10\text{k}\Omega$ ) eliminates the need for a separate biasing network and improves the overall phase-noise performance of the oscillator. The second stage is also a simple voltage amplifier comprised of a single NPN transistor in common emitter configuration. Each stage creates  $\sim 180^\circ$  of phase shift as required and the values of the resistors are carefully chosen to minimize the power consumption. The required voltage gain for the second stage is not large since the motional impedance of the low frequency resonance mode is not much larger than the high frequency resonance mode counterpart.

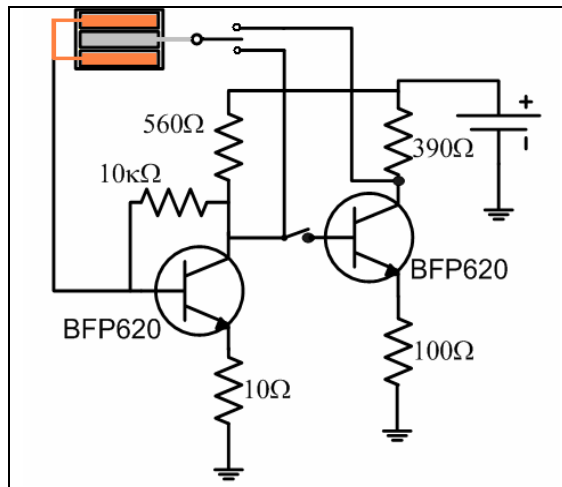


Figure 5.24: The schematic circuit of the dual-frequency oscillator

The measured waveform and phase-noise of the oscillator at the fundamental resonance frequency is shown in Fig. 5.24. The measurements are carried out with an

Agilent EE5500 phase-noise analyzer. An external 50Ω buffer is used to interface the oscillator with the measurement unit.

The oscillation at 35.5MHz in air starts with 0.86V supply voltage and 330μA of current for the two stages combined. Therefore, the power consumption of the circuit at oscillation (35.5MHz) is <math><300\mu\text{W}</math>. The phase-noise measurement is repeated in vacuum and the result is overlapped on the plot in Fig. 5.25. The oscillation starts at lower supply voltage (0.82V) in vacuum and the power consumption is reduced to 200μW. Affected by the improved quality factor of the resonator in vacuum, the close-to-carrier phase-noise is also improved by ~4dBc/Hz at 1kHz offset from the carrier unlike the far-from-carrier phase-noise which is limited by the external buffer.

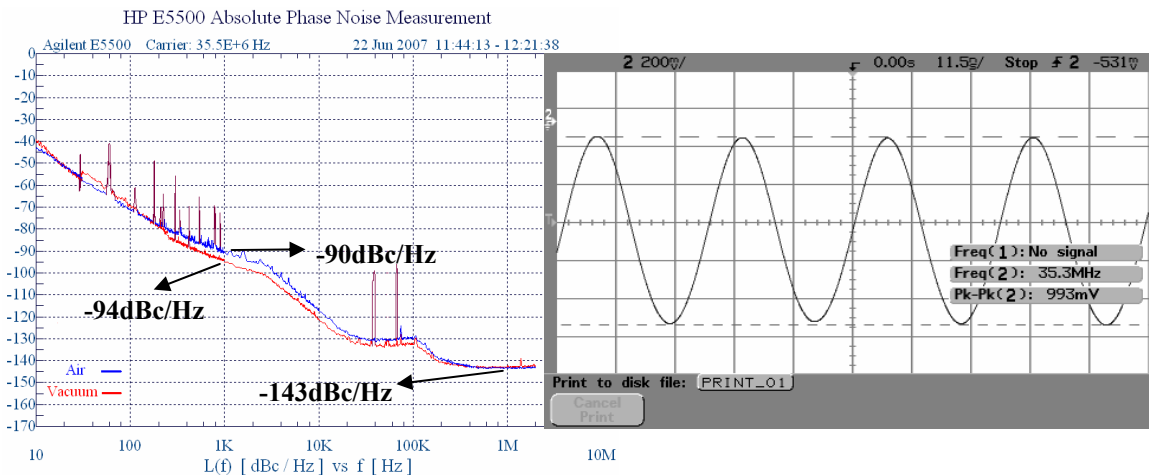


Figure 5.25: The measured waveform and phase noise for the 35MHz oscillation frequency in air and in vacuum.

When the circuit is switched to the single stage operation mode, the oscillation at 105.7MHz starts with 0.98V supply voltage and 350μA current ( $P_{\min} \sim 340\mu\text{W}$ ). The increased power consumption might seem to be counterintuitive after leaving the second amplification stage out of the oscillation loop. This is explained by the higher required

bandwidth, which demands for a larger bias current. The measured phase-noise and the waveform of the oscillator at 105.7MHz are presented in Fig. 5.26.

One important advantage of using TPoS resonators in oscillator application is that despite their small size they exhibit excellent power handling. Therefore, as opposed to the capacitive micromechanical devices [71,72], automatic level control (ALC) circuits are not required to guarantee excitation of the resonator in the linear region. Therefore, larger signal levels can be applied to the device and better far-from-carrier noise density will result while using a simple oscillator circuit with minimal power consumption in a compact solution.

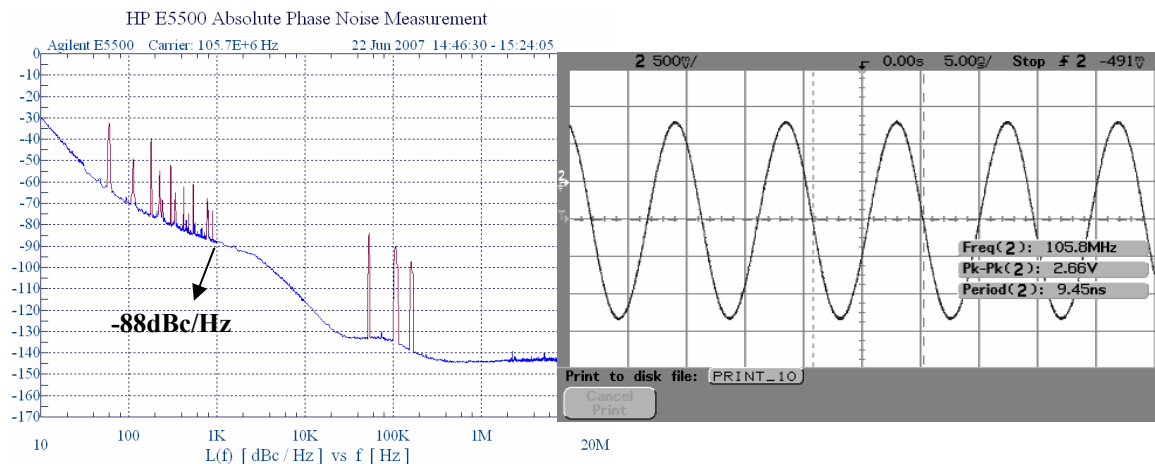


Figure 5.26: The measured waveform and phase noise for the 105.7MHz oscillation frequency in air.

## 5.7 Conclusion

In this chapter, low power reference oscillators based on thin-film piezoelectric-on-substrate (TPoS) resonators were presented at IF to UHF frequencies. Coupled-array TPoS resonators were introduced and proved to be a superior design over the high-order devices in providing the means to systematically reduce the impedance while preventing

excitation of unwanted spurious modes. Also a temperature-stable oscillator with a TCF of  $-2\text{ppm}/^\circ\text{C}$  was built by incorporating the buried oxide layer of the SOI substrate in the stack of resonant structure. Finally, a dual frequency single resonator oscillator architecture was introduced that could select between the fundamental and the high-order mode of a TPoS resonator without the need for any mode-suppression circuit.



## CHAPTER 6

### THIN FILM PIEZOELECTRIC-ON-SUBSTRATE MONOLITHIC FILTERS

Micromachined thin-film piezoelectric-on-silicon (TPoS) acoustic filters fabricated on a single suspended resonant structure are presented in this chapter. Symmetric and asymmetric resonance modes of a silicon resonant structure are piezoelectrically excited, and coupled to realize a second-order narrowband filters. High order lateral bulk acoustic resonance modes of a rectangular plate are utilized to design filters at low RF frequencies. Thickness mode filters are also realized at GHz frequencies using a new interdigitated electrode design. Device dimensions and electrode patterns effective in changing the bandwidth of lateral and thickness mode filters are identified and experimentally verified. Multiple frequency narrowband lateral mode filters fabricated on a SOI substrate with filter  $Q$  values larger than 300 and thickness mode filters with filter  $Q$  values in the range of 150 to 900 at 3.1GHz are demonstrated.

#### 6.1 Introduction

Micromachined electromechanical filters have been long desired as replacement for off-chip components commonly used in wireless transceiver architectures. The unique advantage of these on-chip components is the potential for integration with the rest of the electronics which ultimately improves the level of integrity and complexity in the next generation wireless analog signal processing units. This feature is particularly attractive in multi-band transceivers that operate over a wide frequency spectrum and require arrays of filters with large  $Q$  values and small shape-factors to fit in a compact portable package.

Developing a miniaturized micromechanical filter that meets the requirements on insertion loss (IL), selectivity and power handling all at once is a challenging task rarely accomplished in the past.

Capacitive coupled-resonator filters even though successful in providing excellent selectivity fueled by their high Q resonance peaks, usually suffer from their large IL if terminated to  $50\Omega$  [79,80]. This problem is more prominent at higher frequencies as a result of inefficient electromechanical coupling coefficient. On the other hand, piezoelectric transduction mechanism with orders of magnitude larger coupling coefficient offers a better alternative for enabling low IL filters. Today, thin-film piezoelectric bulk acoustic resonators (FBAR) are implemented in front-end transceiver circuits at GHz frequency range [16]. A number of FBAR resonators are electrically connected in a ladder configuration to provide low-loss high-order filters with a very sharp roll-off skirt. However, for these electrically coupled filters to provide adequate out-of-band rejection, the number of resonators in the coupling chain should be considerably large (between 4 to 10) [81]. Moreover, the center frequency of an FBAR filter is mostly dictated by the thickness of the deposited piezoelectric film and therefore devices fabricated on a substrate can only have close (if not the same) center frequencies. Therefore, electrically coupled FBAR filters span on a large area, and cannot offer an integrated solution for covering dispersed frequencies in a wide range, which eventually can limit their application.

Electrical isolation between input and output ports of an acoustically-coupled filter is the key to reach large isolation in a small, low-order filter. Second-order stacked thin-film piezoelectric BAW filters have been demonstrated with narrow pass-bands and

excellent isolation suitable for applications where small size is critical [82]. The principle of operation for these acoustically-coupled filters is the same as stacked crystal filters [83]. However, the fabrication process is relatively complicated in a sense that multiple precisely-controlled thin-film deposition steps are involved and thickness deviation can substantially degrade the performance of the filter. These filters also suffer from single-band operation on a chip.

In this chapter, we introduce an alternative class of acoustically-coupled piezoelectric filters called monolithic thin-film piezoelectric-on-substrate (TPoS) filters. Multiple modes of a single resonant structure are coupled in order to achieve a higher order system. The same technique has been implemented in monolithic crystal filter (MCF) technology for decades [84]. In an MCF, by properly patterning isolated metal electrodes on a single quartz plate, multiple resonance modes of the plate are coupled at low frequencies. Theoretically all different classes of resonance modes such as flexural, rotational, and extensional can be utilized to create monolithic coupled resonator filter devices. However, great majority of the MCF's have been based on coupled thickness extensional modes [84,85]. Center frequency of these filters are not usually more than a few ten's of MHz and they are limited to the thinnest crystal plate that can be reproducibly manufactured. With the emergence of thin-film technologies very high frequency (few GHz) thickness mode piezoelectric filters are demonstrated and commercialized (e.g. FBAR's). However, the technique most attractive for low-frequency crystal filters (monolithic mode coupling) have not been yet adopted for these new-generation of acoustic devices.

Our attempt is to demonstrate the potential for the same acoustic coupling techniques to be utilized in thin-film piezoelectric devices at high frequencies. Multiple-frequency filters on a single substrate can be implemented by changing the lateral geometry of the lateral-mode filters. We demonstrate slight frequency shift in thickness mode devices covering multiple adjacent channels in a single-band and substantial change in the resonance frequency in lateral mode devices for multiple-band operation of the filters fabricated on a single substrate. The bandwidth in these filters can be controlled by changing the device dimensions and electrode pattern. Preliminary guidelines for the design of monolithic thin-film piezoelectric filters are presented.

## 6.2 Design Principles

A monolithic TPoS filter is structurally the same as a two-port TPoS resonator (Fig. 6.1). The difference between a TPoS resonator and a filter is mainly in the top electrode pattern. In a TPoS filter the top electrode is properly patterned to enable excitation of dual resonance modes of a released structure. In a symmetric mode displacement in both electrodes is in-phase where as, in an asymmetric mode the developed strain field on the two electrodes is  $180^\circ$  out of phase.

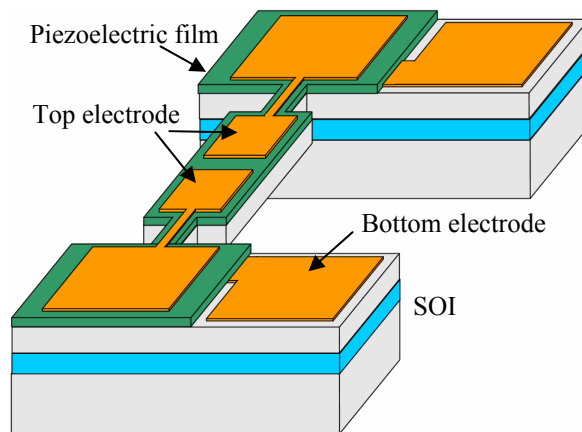


Figure 6.1: The schematic diagram of a monolithic TPoS filter.

The transfer function of this coupled-mode system is not of second order and rather is of fourth order which fits the definition of a second-order filter. Higher order filters (3<sup>rd</sup>, 4<sup>th</sup>...) can also be realized using the same concept but we will limit our discussion to second-order filters in this work.

Monolithic crystal filters have been chronically attractive for their small size, ease of fabrication, and therefore lower cost. Monolithic TPoS filters are also believed to inherit the same advantages over other types of electromechanical filters. By coupling multiple modes of a single resonant structure the need for a discrete coupling element is eliminated which simplifies both the design and fabrication process and reduces the overall area consumption. The only issues to be dealt with are design procedures for choosing the device shape and patterning the electrodes in order to control the filter bandwidth and to suppress unwanted modes.

Depending on the frequency of interest different category of resonance modes can be employed to realize monolithic TPoS filters. For LF to IF frequency band flexural resonance modes are suitable. Lateral extensional resonance modes suit IF to low RF applications and thickness extensional modes are of interest for GHz range. Simulating the resonance mode-shape of a chosen structure provides considerable insight for optimization of the electrode pattern to maximize the electromechanical coupling and consequently reduce the insertion loss of the filter. After simulating the targeted resonance mode, surface areas of the structure on which the polarity of the strain field is identical should be covered with connected pieces of metal electrode. Connecting areas with opposite polarity strain field results in charge cancellation and reduces the coupling coefficient.

Although this design method is always valid, it loses applicability very quickly when the resonant structure is a multi-layer compound stack of material and is enlarged in order to reduce the motional impedance. Finding resonance mode-shapes of large structures requires very large number of meshing elements in finite element analysis (FEA) tools which makes the method impractical. However, some intuitive design rules extracted from simulating simple structures can be loosely applied for more complicated cases. In next sub-sections two resonant mode-shapes of a simple plate are discussed to better explain some of these rules.

### **6.2.1 Lateral Mode**

We assume a rectangular silicon plate (similar to Fig. 6.1) as the resonant structure. In the first width extensional mode, the resonant body uniformly expands and contracts as seen in the mode-shape of Fig. 6.2a. However, there exists another width-extensional mode-shape where the displacement in the two halves of the structure (along the length) is out-of-phase (Fig. 6.2b). If the entire length of the structure is covered with a single metal piece (a one-port device) only the symmetrical width-extensional mode-shape can be excited. Also, if the two isolated input and output ports in a two-port device comprise of two metal stripes covering the length of the device in parallel again the asymmetric mode-shape can not be excited. On the contrary, by splitting the electrode in two isolated pieces from the middle of the device, both modes can be excited. In that case, the system transfer function is of fourth order (second-order filter).

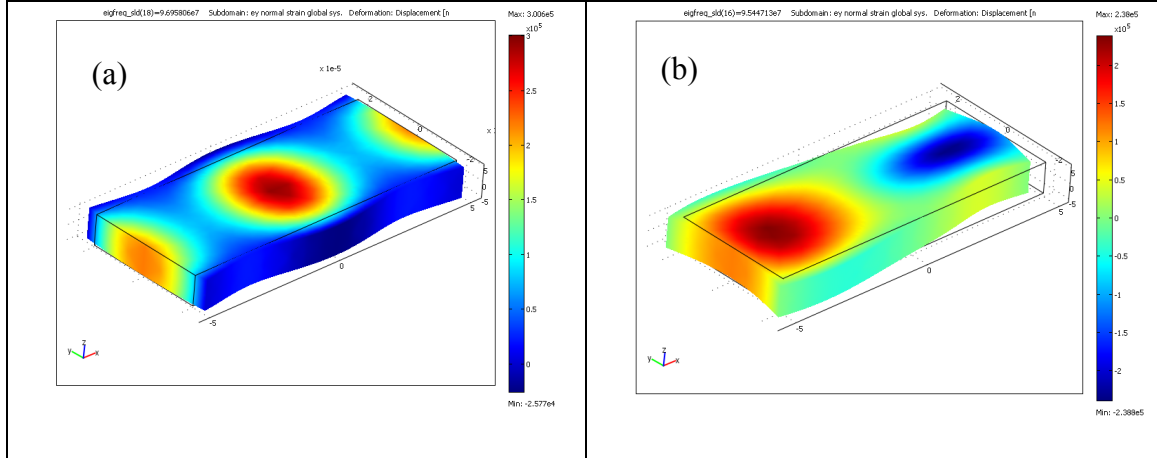


Figure 6.2: Simulated dual fundamental width-extensional resonance mode-shapes of a 40µm wide silicon plate a) symmetric and b) asymmetric.

Based on the same discussed concept, dual high-order lateral extensional modes of a plate can be excited and coupled. By increasing the mode-number (device size) the actuation area can be increased and therefore motional impedance is lowered for higher frequencies. Dual mode-shapes of a plate in third-order resonance mode are simulated in Fig. 6.3. The optimized electrode pattern for such a mode-shape is a multi-finger electrode matching the strain field and split into half from the middle (Fig. 6.3). The center-to-center finger pitch is equal to the wavelength. The same pattern can theoretically be repeated indefinitely to reduce the IL.

The critical dimension which defines the center frequency in a lateral mode monolithic filter is the width of the plate (or the finger pitch). However, the length of the device on the other hand has an interesting effect which can be employed to design the BW of the filter. It is observed in simulations that by changing the length (marked in Fig. 6.3) of the plate the frequency spacing between the dual modes will change. Therefore, the BW of a filter at a certain center frequency can be modified by changing the length of

the plate. By decreasing the length the BW will increase and this trend will be experimentally verified in the following sections.

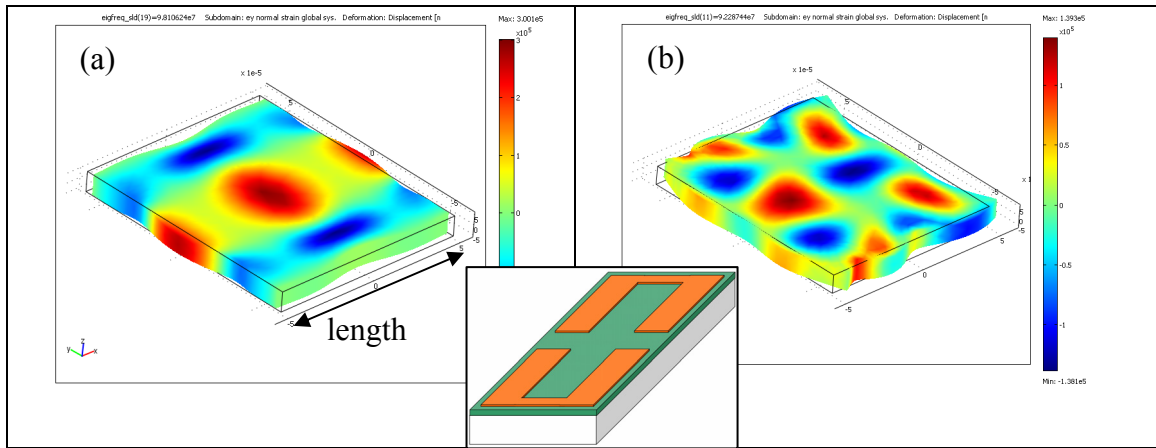


Figure 6.3: Simulated dual third-order width-extensional resonance mode-shapes of a 160 $\mu\text{m}$  wide silicon plate and the schematic viewgraph of the suggested electrode pattern.

### 6.2.2 Thickness Mode

A similar rectangular plate can be simulated in the first thickness extensional resonance mode and the mode-shape is shown in Fig. 6.4a. The simulation is performed in 2D (cross section of the plate) in order to reduce the computational complexity. As seen, this mode-shape is symmetric relative to the  $X=0$  axis. The dual asymmetric mode-shape is shown in Fig. 6.4b. Similar to the lateral mode case, in this mode-shape the strain field in the two halves of the structure is out-of-phase. Therefore, the optimized electrode pattern to excite and couple the two modes is shown in Fig. 6.4b.

One would conclude that the same electrode pattern used for a lateral mode filter can potentially excite the coupled thickness modes of the structure. Even though theoretically true in practice it was observed that the pattern employed for a lateral-mode device is not optimized for operation of a thickness mode filter. The problem is the excessive number of spurious modes excited by a simple two-piece electrode pattern. In



other words, this pattern is not efficient in constraining acoustic energy in two targeted modes on a relatively large suspended plate.

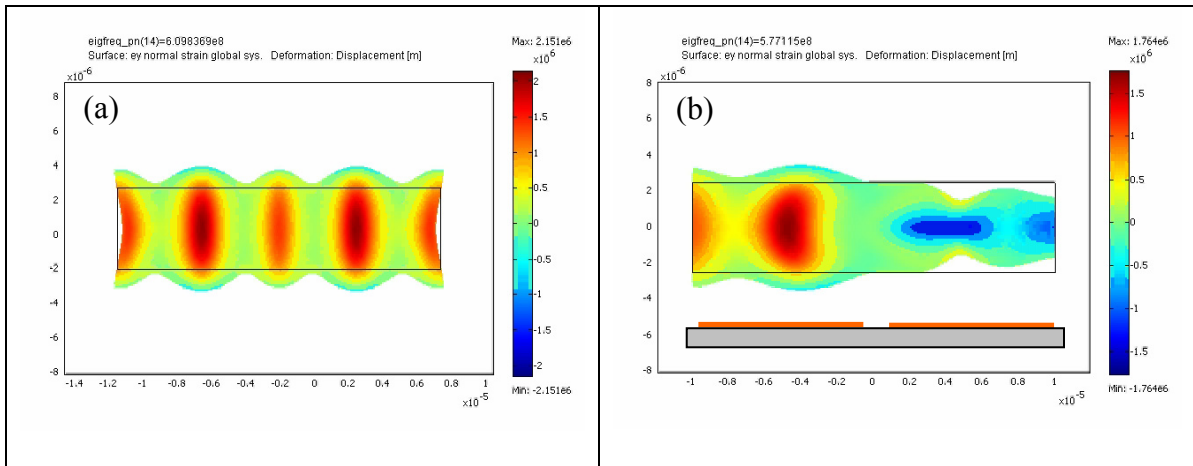


Figure 6.4: Simulated first-order dual thickness resonance mode-shapes of a silicon plate in 2D.

One alternative approach to alleviate the problem is an interdigitated pattern (Fig. 6.5). With this design, in the in-phase mode the area covered by fingers is under uniform strain field where as in the dual mode the displacement of the two finger sets is out-of-phase. The latter mode-shape resembles a high order standing acoustic wave. Using FEA analysis multiple mode-shapes from this family can be identified in a structure. These modes are different in the number of strain-alternating sections developed in the structure at resonance.

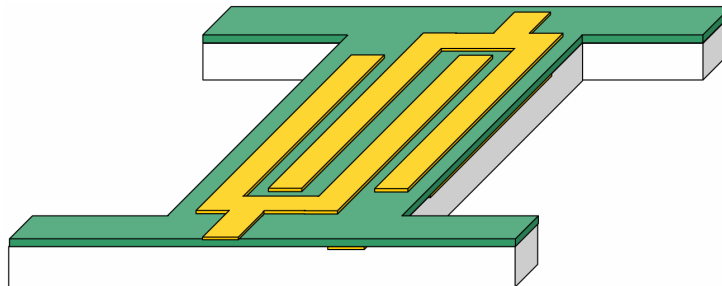


Figure 6.5: The schematic viewgraph of interdigitated electrode pattern for monolithic thickness mode TPOs filters.

One of these modes dividing the structure of Fig. 6.4 in three sections is shown in Fig 6.6. Since the resonance frequency of each of these modes is slightly different than the others, the frequency spacing or in other words the bandwidth of the second order thickness mode filter can also be designed by changing the number of fingers covering a suspended plate. From FEA simulation results, it is predicted that by increasing the number of fingers the frequency spacing between the two coupled modes increases. The legitimacy of this prediction will be evaluated by experimental measurements presented in the following section.

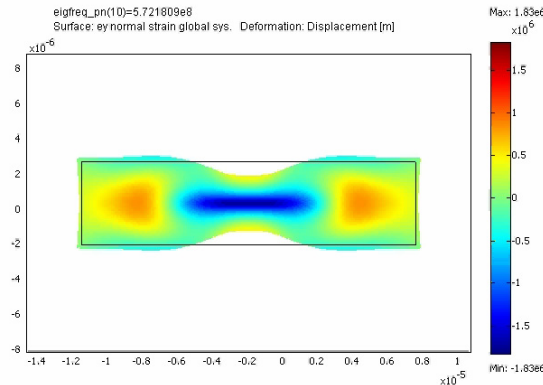


Figure 6.6: Simulated thickness resonance mode-shapes of a silicon plate in 2D with three strain-alternating sections.

In contrast with FBAR filters, in a TPoS device the strain field developed in the film and consequently, the electromechanical coupling for the fundamental thickness-mode is not usually the strongest. This is because the piezoelectric layer comprises a fraction of the structure thickness. Therefore, the mode number for which the insertion loss is the lowest depends on the thickness ratio between the piezoelectric film and the substrate. For example, in a thickness mode TPoS filter with approximately 2 to 1 thickness ratio between the silicon layer and the piezoelectric film, the third harmonic thickness-mode is more likely to have the lowest insertion loss, where as with the

thickness ratio of 1 to 1, maximum charge is developed on the electrodes for the second harmonic mode. It is also noteworthy that for a TPoS device, even mode orders can also be excited as opposed to an FBAR where only odd mode orders appear.

### 6.3 Equivalent Electrical Model

Mechanically-coupled resonator systems are represented variously in electrical domain. One common representation of these systems is shown in Fig. 6.7 [86]. Individual resonators in this circuit are modeled as series RLC tanks coupled through a coupling shunt capacitor ( $C_c$ ). This capacitor symbolizes the effect of the coupling element and increases the order of the transfer function of the system from two to four.  $R_m$ ,  $L_m$ , and  $C_m$  are the motional resistance, inductance and capacitance of the resonator and  $C_s$  is the static shunt capacitance of the input and output electrodes to ground.  $C_f$  represents the stray capacitance that passes a portion of the signal from input to the output directly.

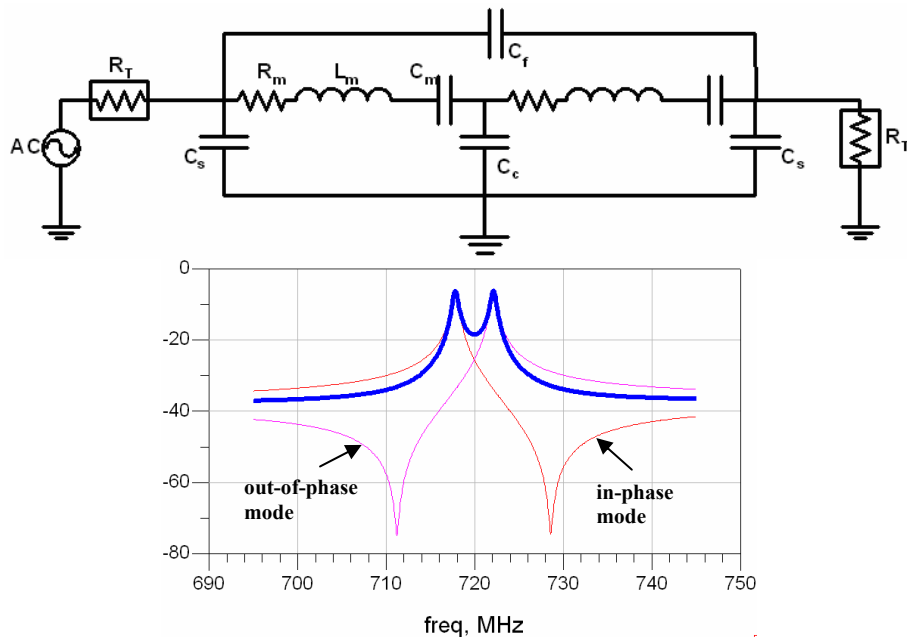


Figure 6.7: The schematic equivalent electrical model for second-order mechanically-coupled resonator filters and a typical corresponding frequency response.

In this model, it is clear that the filter insertion loss is closely related to the motional impedance of each individual resonator. However, increasing the termination load impedance ( $R_T$ ) will also improve the insertion loss and also affects the ripple in the pass-band (loading the  $Q$ ). The effect of termination load on the filter characteristic is limited by the figure of merit defined in equation 3.11. This is because increasing the termination impedance will not affect the response if the equivalent impedance of the shunt capacitor is not comparably large. In other words, if the impedance of the shunt capacitor is small then a large portion of the current will not pass through the termination impedance and therefore increasing the termination is ineffective. In most RF applications the standard termination load is fixed at  $50\Omega$  and therefore the equivalent impedance of the shunt capacitor at the frequency of operation should be large compared to  $50\Omega$  and concurrently the motional impedance should be small relative to  $50\Omega$  (Large figure of merit).

The same model seen in Fig. 6.7 can be employed for monolithic filters. However, unlike mechanically-coupled resonators no discrete coupling component is identified in a monolithic filter and rather the acoustic energy is coupled through the substrate. This may cause discrepancies between the frequency response of the electrical model and the actual device as it will be seen.

In the electrical model of Fig. 6.7 the frequency of the in-phase mode (no current passing through the coupling capacitor) is always lower than the frequency of the out-of-phase mode. This is not usually the case for a monolithic filter and therefore two notches will appear before and after the filter passband in the frequency response. In order to include this characteristic in the electrical model there are some alternatives. One is to

use an ideal transformer in the model which accounts for phase inversion in one of the modes (Fig. 6.8a) [87]. This way the frequency of the two modes can be controlled separately and if the frequency of the resonance peak in the branch with mode inversion is chosen lower than the other branch the two notches appear in the frequency response (Fig. 6.8c). The other alternative is to replace the coupling capacitor with a coupling inductor (Fig. 6.8b) [88]. The inductor will take care of the phase inversion and the notches will appear in the frequency response.

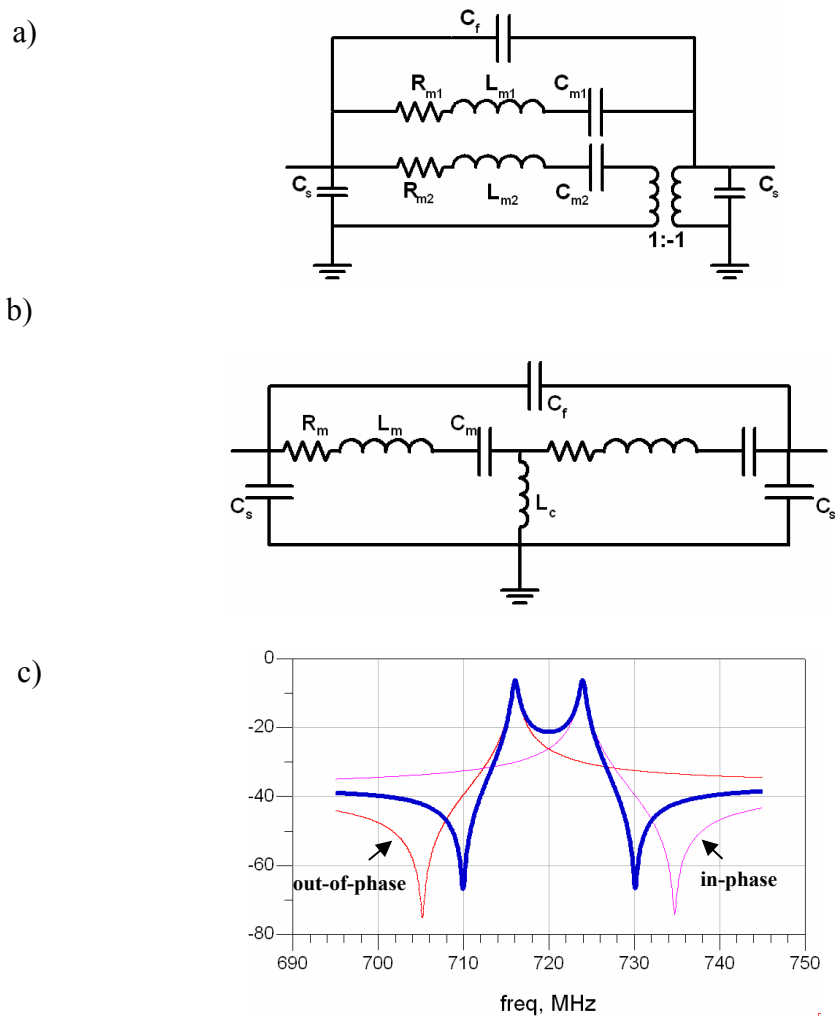


Figure 6.8: Alternative equivalent electrical models for second-order mechanically-coupled resonator filters a) with transformer b) with coupling inductor, and c) a typical corresponding frequency response.

## 6.4 Implementation and Results

Fabricated monolithic TPoS filters on a SOI substrate were tested on a Suss RF probe station using Agilent E5071B and E8364B network analyzers in atmospheric pressure. SOLT calibration was performed with GSG probes. Two-port *s*-parameter measurements were taken, and saved as frequency plot pictures and touchstone (.s2p) data files.

The first presented result is measured from a lateral mode device with center frequency of  $\sim 440$  MHz (Fig. 6.9). The center-to-center finger pitch size for this device is drawn as  $16\mu\text{m}$ . The frequency spacing between the two resonance peaks is  $\sim 1.2$  MHz which results in a filter *Q* of  $\sim 300$ . The termination impedance is set to  $500\Omega$  for this measurement and lower IL is expected by increasing the termination impedance.

Frequency response plots of Fig. 6.10 are measured from two different monolithic filters with a center frequency at  $\sim 635$  MHz. These results show how the bandwidth of a lateral monolithic filter can be designed by changing the length of the device. The finger pitch size in these two devices is  $10\mu\text{m}$ . The plot presented in Fig. 6.10a is measured from a device with a length of  $50\mu\text{m}$  and the plot in Fig. 6.10b is from a device with a length of  $35\mu\text{m}$ . As it was expected the BW of the filter is increased by reducing the length of the device. However, one should notice that by decreasing the length of the device (assuming the same number of fingers) the total area covered by electrodes (actuation area) is reduced. Therefore to design low IL filters with relatively wide BW the number of finger should be increased to keep a large actuation area.

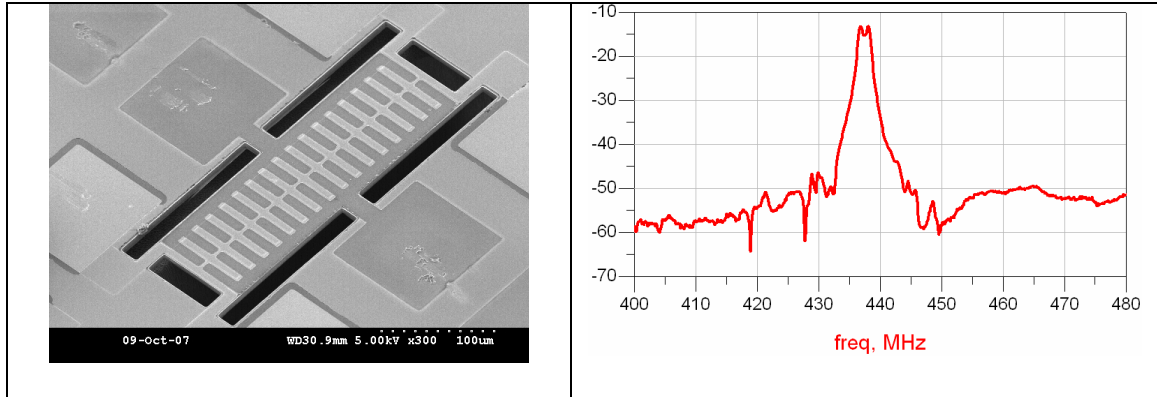


Figure 6.9: The measured frequency response and SEM picture of a monolithic lateral TPoS filter at 440MHz.

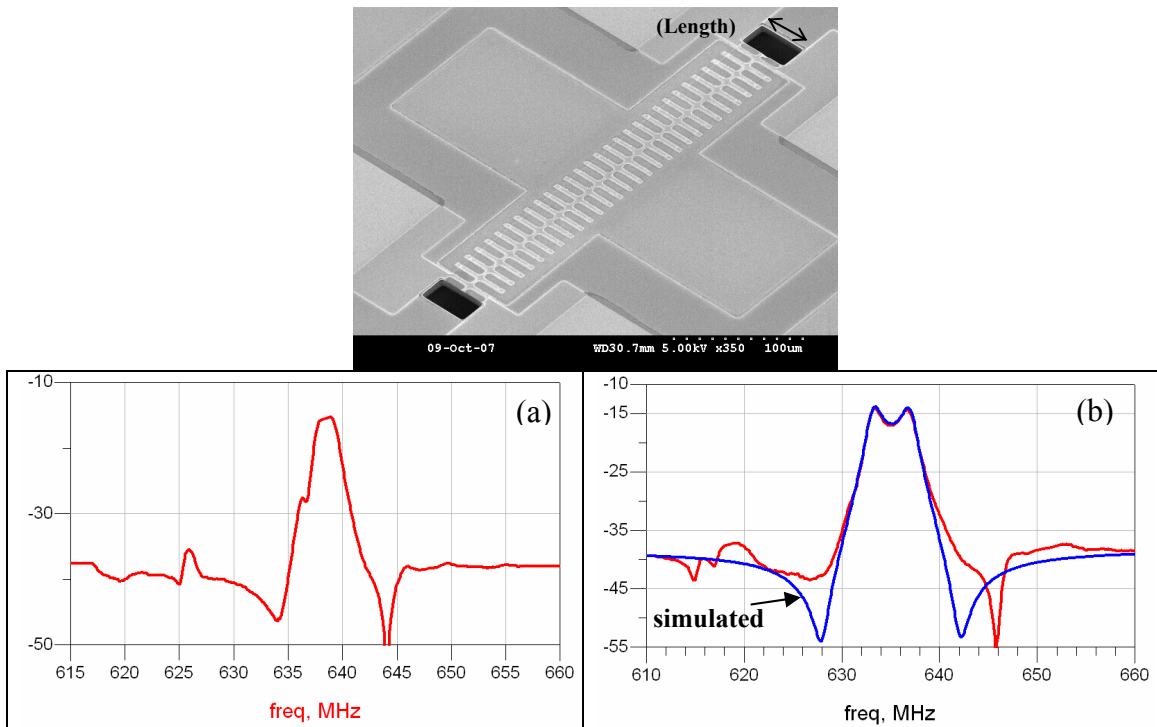


Figure 6.10: The SEM picture of a lateral TPoS filters with 10μm finger pitch and frequency response for two devices; a) 50μm long and b) 35μm long

As opposed to the frequency response plot presented in Fig. 6.9 the two notches before and after the filter passband are more prominent in the results shown in Fig. 6.10. This is because the appearance of the notches is dependent on the feedthrough impedance of the filter. For lower frequencies where the feedthrough impedance is large (the signal floor is low) the two notches almost disappear in the noise floor, where as at higher

frequencies the effect of the feedthrough capacitance is dominant. Table 6.1 summarizes the individual component values used to plot the simulated response in Fig. 6.10b. The model introduced in Fig. 6.8b is used for generating the plot and as it is seen the model can capture the filter characteristic with acceptable accuracy. To further improve the model one can include the effect of dielectric loss in the piezoelectric film by adding shunt resistances to ground in the input and output ports. Also asymmetry in the measured frequency response can be captured by including a capacitor in the inductive coupling branch [88].

TABLE 6.1: COMPONENT VALUES IN THE ELECTRICAL MODEL OF FIG. 6.8B USED FOR SIMULATION.

element	$L_m$	$C_m$	$R_m$	$L_c$	$C_s$	$C_f$
value	100uH	0.625fF	750 $\Omega$	0.6uH	0.65pF	8fF

The highest-frequency (915MHz) fabricated monolithic lateral-mode filter is shown in the optical micrograph of Fig. 6.11. The finger pitch on this device is 6 $\mu$ m and the measured frequency response is presented in Fig. 6.11 as well.

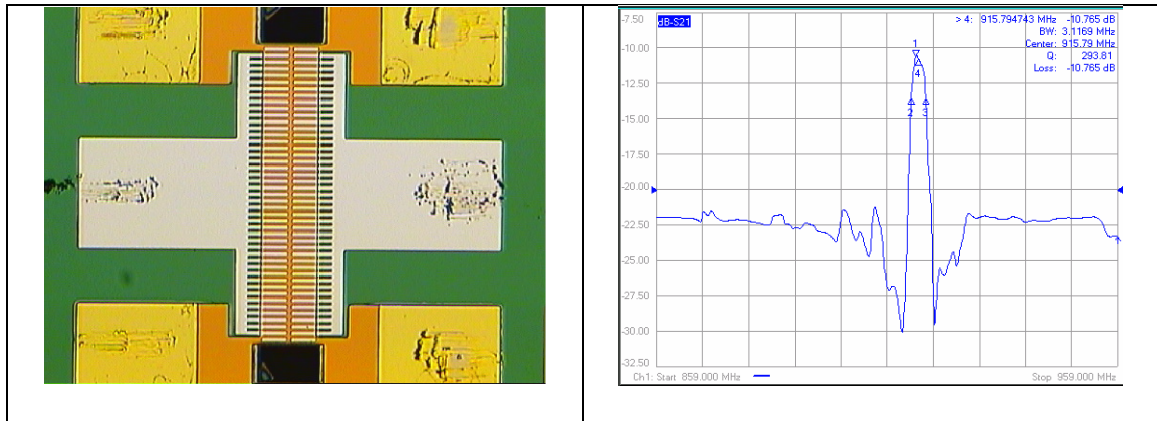


Figure 6.11: The optical micrograph and the frequency response of a 915MHz lateral TPoS filter.

Thickness mode TPoS filters are also fabricated and characterized. Results from two different monolithic TPoS filters designed for operation in a thickness extensional



mode are shown in Fig. 6.12. The thickness ratio of the silicon to the ZnO film is  $\sim 5$  and the mode number with the minimum IL were measured to be the 5<sup>th</sup> mode at  $\sim 3.5$ GHz. The overlapped measured plots are taken from adjacent devices with a various lateral dimension labeled as L on the inset SEM picture of the device.

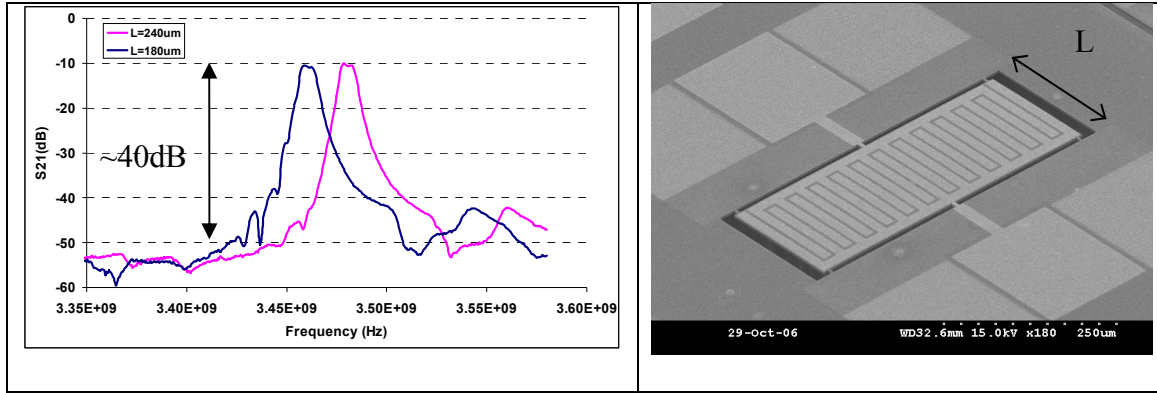


Figure 6.12: Measured frequency response plots and the SEM picture of 3.5 GHz thickness mode monolithic TPoS filters.

The frequency response plots replicate each other with a frequency offset of  $< 20$  MHz. The filter BW is  $\sim 8.5$  MHz resulting in a filter  $Q$  of  $> 400$ . The filters are inductively tuned (shunt inductors are used to cancel out the effect of shunt capacitors) and terminated to  $250 \Omega$ . The measured isolation of  $> 40$  dB is remarkably large for a second order filter consuming a small area of less than  $500 \mu\text{m} \times 250 \mu\text{m}$ .

To confirm the BW design method discussed in section 6.2.2, on the same suspended plate we have patterned the top electrode with various number of fingers and measured the frequency response for each device. Results are consistent with the trend predicted and the BW of the filters with larger number of fingers is larger. Table 6.2 summarizes the measured BW for four different filters and shows the corresponding number of fingers. Two of the frequency response plots are shown in Fig 6.13.

TABLE 6.2: BW OF THICKNESS-MODE FILTERS WITH IDENTICAL RESONANT STRUCTURE AND DIFFERENT NUMBER OF FINGERS.

# of fingers	9	11	13	15
BW(MHz)	4	9	15	22
Filter Q	875	333	206	140

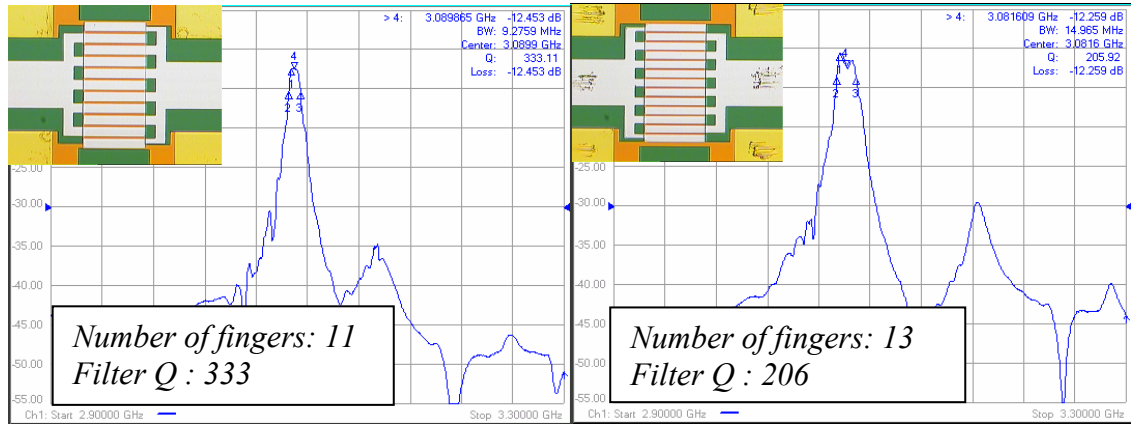


Figure 6.13: Measured frequency response plots and optical viewgraphs of two thickness mode monolithic TPOs filters with different number of fingers.

## 6.5 Conclusion

Monolithic thin-film ZnO-on-silicon filters are designed and fabricated utilizing lateral and thickness extensional resonance modes of a free-standing composite structure. By changing the lateral dimension of these filters both coarse and fine frequency offset is achievable in laterally-excited and thickness mode devices. The BW of a TPOs filter can also be designed by changing the device dimension and the electrode pattern. Single-chip multi-band narrow BW filters with large out-of-band rejection are fabricated using a simple and low-temperature process in a small foot-print, suitable for channel-select filtering in new generation wireless communication equipment. Narrow BW lateral mode filters at low RF range and thickness mode filters with  $Q$  values in the range of 150 to  $\sim$ 900 were demonstrated.

# **CHAPTER 7**

## **THIN FILM PIEZOELECTRIC-ON-DIAMOND RESONATORS AND FILTERS**

In this chapter thin-film piezoelectric-on-diamond composite bulk acoustic resonators are introduced. These resonators benefit from the large elastic modulus of the nano-crystalline diamond to increase the resonance frequency. More than  $1.8\times$  increase in the resonance frequency is measured for devices fabricated on  $2\mu\text{m}$  thick diamond compared to the same size devices made on  $6\mu\text{m}$  thick silicon on insulator substrate. Application of these resonators in monolithic filters and mass sensors are demonstrated

### **7.1 Introduction**

Nano-crystalline diamond (NCD) is an emerging material with growing applications in MEMS, driven by its superior mechanical properties such as high acoustic velocity, low acoustic loss, chemical stability, and very low wear rate. The use of polycrystalline diamond as an acoustic media for surface acoustic wave (SAW) devices has proven unparalleled in increasing the frequency of operation while relaxing requirement on the lithographic resolution [89]. Capacitively transduced diamond disk resonators have also been showcased at GHz frequencies, increasing the resonance frequency by a factor of  $\sim 2$  compared to the same size resonators made of polysilicon [90]. However, very high motional impedance of these capacitive devices limits their system-level applications as they are required to interface with low impedance radio frequency (RF) electronics. A resonator with high impedance introduces excessive loss if

used in a filter and requires multiple gain stages to sustain oscillation in an oscillator circuit, increasing the power consumption and design complexity.

As discussed in previous chapter the large electro-mechanical coupling coefficient in a TPoS resonator can potentially provide orders of magnitude lower motional impedance compared to a capacitive resonator at the same frequency. The underlying structural material in these devices improves the energy density, structural integrity, and for the most part defines the resonance frequency.

In this chapter, silicon is replaced with NCD to further increase the resonance frequency of the device and relax the requirements on lithographically-defined feature sizes of the resonator at high resonance frequencies. The temperature coefficient of frequency of diamond is relatively low ( $-12\text{ppm}/^\circ\text{C}$ ) [90], adding more value to its application as a substrate. A thin layer of oxide with a large positive TCF ( $\sim 85\text{ppm}/^\circ\text{C}$ ) [91] can be used as a passive temperature compensation technique. Although, lower acoustic velocity of the oxide film decreases the resonance frequency, it is offset by very large acoustic velocity of diamond. Therefore, both resonance frequency and temperature stability of thin-film piezoelectric-on-diamond (TPoD) resonators are superior to devices made from other structural materials such as silicon or pure piezoelectric [92].

One common application for resonators is in gravimeters. Quartz crystal microbalance (QCM) mass sensors have found many applications in chemical and biological sensors [93]. However, their relatively large size can limit the extent in which QCM sensors are used in microsystems to detect small traces of chemical or biochemical agents. Specifically, in applications for which an array of mass sensitive sensors is

required to distinguish between various types of molecules, QCM sensors fail to offer a compact and cost effective solution.

In recent years, micromachined resonant mass sensors with much smaller form-factor have attracted a lot of attention to fill in the gap for arrayed and/or implantable mass sensors. Cantilever beams [94] and thin film bulk acoustic resonators [95] are amongst the more successful realizations of micromachined mass sensors. Higher frequency of operation can potentially improve the sensitivity of these devices compared to QCM sensors, if high quality factors are maintained [96]. Sensitivity to environmental parameters (e.g., temperature) is also an issue that needs to be addressed in order to facilitate robust operation of micromachined mass sensors. Complex actuation and readout mechanism [94] is another bottleneck hindering widespread use of these devices in microsystems.

Capacitively-transduced lateral bulk acoustic resonant sensors were introduced in our group as an effort to address some of the issues associated with micromachined mass sensors [97]. These devices demonstrated relatively high  $Q$  values in air at  $\sim 12\text{MHz}$  while minimizing the change in the effective stiffness of the structure imposed by absorbed mass. However, to increase the sensitivity, the device dimension needed to be scaled down, resulting in a reduced capacitive transduction area. Therefore, motional impedance of the device will increase, which translates to high power consumption and higher phase noise when interfaced with an oscillator circuit. More importantly, small capacitive air gaps are prone to blockage and squeeze film damping when exposed to environment.

In this chapter, the TPoD structure is used for implementation of monolithic filters and  $1.5\times$  frequency increase over geometrically identical devices fabricated on SOI (chapter 6) is observed.

Also a TPoD resonator with the same resonant structure introduced in [97] is characterized as a mass sensor. The class of devices introduced in this chapter can promise extremely compact assembly of fully temperature-compensated array of mass sensors in the future.

## 7.2 Process Development

Although the fabrication process flow for TPoD resonators (Fig. 7.1) is very similar to that of TPoS resonators, processing on a thin-film NCD substrate requires development of new processing steps.

### 7.2.1 Process Flow

Two to three micrometers of nano-crystalline diamond is deposited on silicon wafers in a microwave assisted chemical vapor deposition chamber at  $800^{\circ}\text{C}$  to prepare the initial substrate. The surface roughness of the diamond film is directly related to the thickness and the grain size of the nano-crystalline diamond.

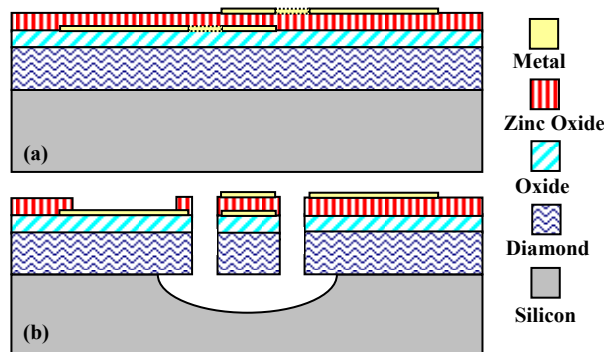


Figure 7.1: Schematic process flow for the fabrication of TPoD resonators; a) stack development b) etch and release.

This roughness imposes a major challenge in our technology by reducing the ZnO piezoelectric coefficient as a result of scattering the crystallographic orientation of the grains. To address this problem, a thin ( $<1\mu\text{m}$ ) buffer oxide layer is deposited in a plasma enhanced chemical vapor deposition (PECVD) tool and polished back to less than  $0.5\mu\text{m}$  thickness before the subsequent layers are deposited/patterned (Fig. 7.1a). This polished oxide layer has dual functionality: first, it provides a smooth surface for the deposition of high quality ZnO; second, it reduces the TCF of the resulting composite resonator structure.

The bottom metal electrodes are deposited and patterned followed by sputtering a thin ( $<0.5\mu\text{m}$ ) ZnO film. Top metal electrodes are deposited and patterned and access holes to the bottom electrodes are etched. A relatively thick ( $3\mu\text{m}$ ) PECVD oxide mask layer is deposited and patterned and the resonator structural stack is etched, layer by layer down to the silicon substrate (Fig. 7.1b). ZnO is wet-etched in diluted acetic acid solution; the buffer oxide and the diamond layers are dry etched in an inductively coupled plasma (ICP) tool. Oxygen plasma is used to etch the diamond layer. The final release step is performed by isotropically etching silicon in ICP using  $\text{SF}_6$  gas. For wide structures silicon layer is etched away from the backside, the same way it was performed in the SOI process. Finally, the residue of the oxide mask layer is removed in ICP.

### **7.2.1 ZnO Sputtering**

As discussed in chapters two and three the quality of c-axis oriented ZnO film has a significant effect on the performance of the fabricated resonator, specifically on its motional resistance ( $R_m$ ), through the effective piezoelectric coefficient ( $d_{31}$ ):

$$R_m \propto \frac{I}{d_{31}^2}. \quad (7.1)$$

The properties of the substrate and its surface have a dominant effect on the quality of the sputtered ZnO film [98,99]. As seen in the SEM view of Fig. 7.2a, the surface roughness of the polycrystalline diamond is directly projected to the sputtered ZnO, and scatters the columnar grain structure. The polished surface of an oxide layer deposited on top of the diamond layer compensates for the surface roughness and significantly improves the quality of the sputtered ZnO (Fig. 7.2b).

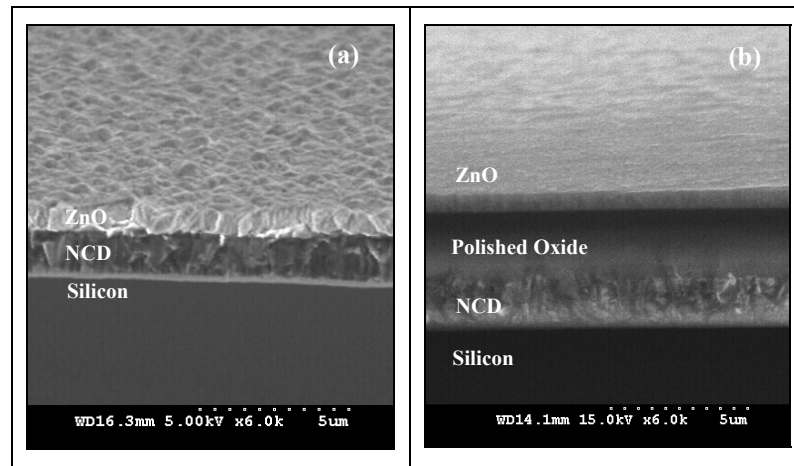


Figure 7.2: SEM pictures comparing the morphology of sputtered ZnO a) directly on NC diamond and b) on polished oxide coated NC diamond.

To analyze the properties of the sputtered ZnO, x-ray diffraction (XRD) has been used. In Fig. 7.3 measured  $2\theta$  XRD curves from ZnO samples sputtered on polished oxide and diamond substrates at different temperatures are compared. The best quality ZnO is obtained by sputtering on polished oxide at elevated temperature ( $350^{\circ}\text{C}$ ), which confirms the effect of the surface roughness and the sputtering temperature on the grain orientation.



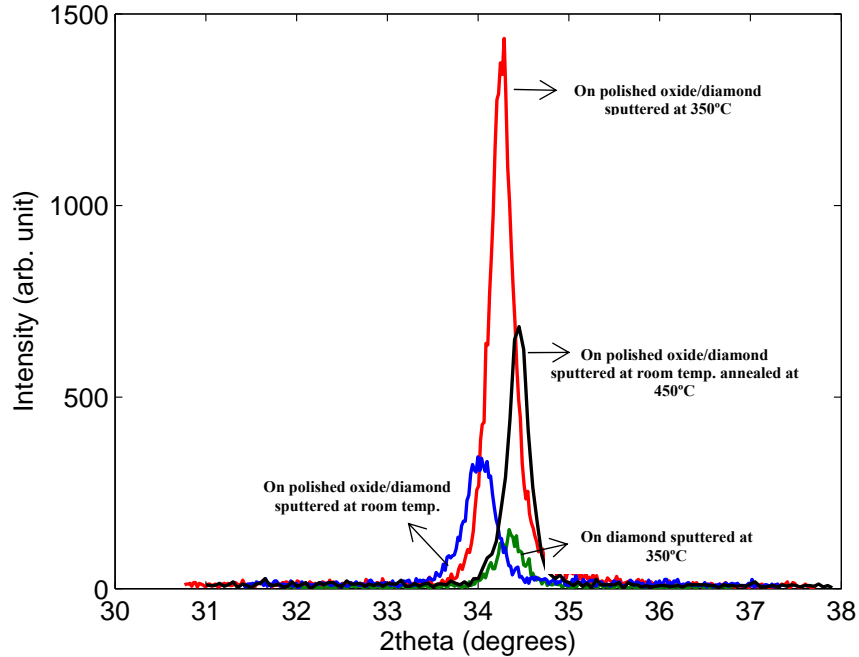


Figure 7.3: XRD  $2\theta$  plots measured from ZnO sputtered samples on different substrates with various sputtering parameters.

### 7.3 Resonator Design and Fabrication

In this work, the resonator structure is a rectangular plate excited in its lateral extensional mode. The top electrodes are patterned to form an array of interdigitated fingers. This results in a two-port resonator configuration resonating in a high order lateral mode. Increasing the transduction area (number of fingers) in this design reduces the motional resistance of the device, making it suitable for RF applications []. Smaller finger pitch increases the frequency of operation. The SEM of Fig. 7.4a is a fabricated 15<sup>th</sup> order TPOD resonator with a finger pitch size of 10 $\mu\text{m}$ . A cross-section SEM view of the composite stack is shown in Fig. 7.4b.

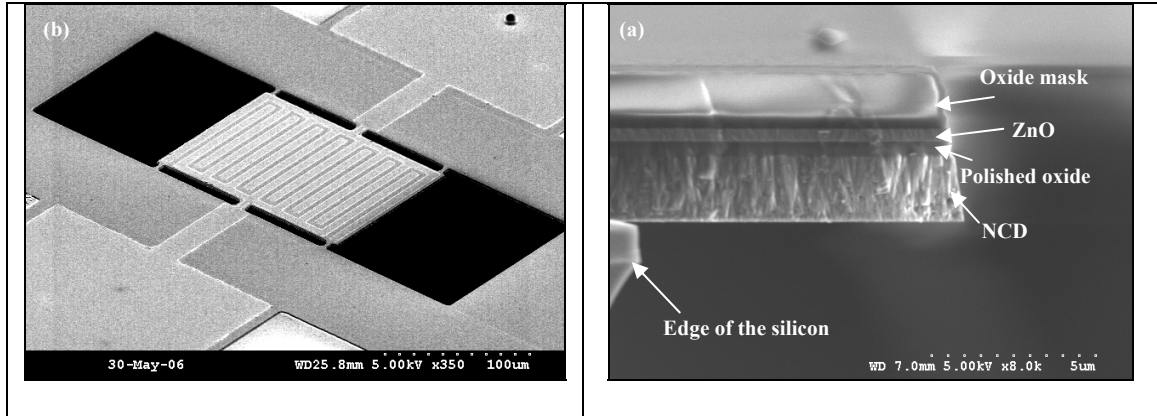


Figure 7.4: a) The SEM of a fabricated TPoD resonator; and b) The cross-sectional view of the etched composite stack.

## 7.4 Effect of Oxide

The frequency of operation and the resonance mode-shape are functions of relative thicknesses of all the layers comprising the resonant structure. The fundamental resonance mode-shape for a structure with  $L=5\mu\text{m}$  and  $W=2\mu\text{m}$  consisting of a  $2\mu\text{m}$  thick diamond layer, a  $0.5\mu\text{m}$  thick oxide layer and a  $0.5\mu\text{m}$  thick ZnO layer is simulated in FEMLAB. The result is presented in Fig. 7.5a. The mode-shape for an identical resonator but without the oxide layer is shown in Fig. 7.5b (ZnO layer is directly deposited on diamond).

The Young's modulus of the diamond was assumed to be  $1000\text{GPa}$  in these simulations. As seen in the simulated results, the oxide layer reduces the resonance frequency from  $1.4\text{GHz}$  to  $1.2\text{GHz}$  and also affects the resonance mode-shape. The displacement field in the device with buffer oxide layer quickly fades out from the ZnO layer toward the diamond film, and out-of-plane components are considerably prominent compared to the case without oxide. This can cause charge cancellation sites to develop across electrodes, and increases the effective motional impedance of the resonator.

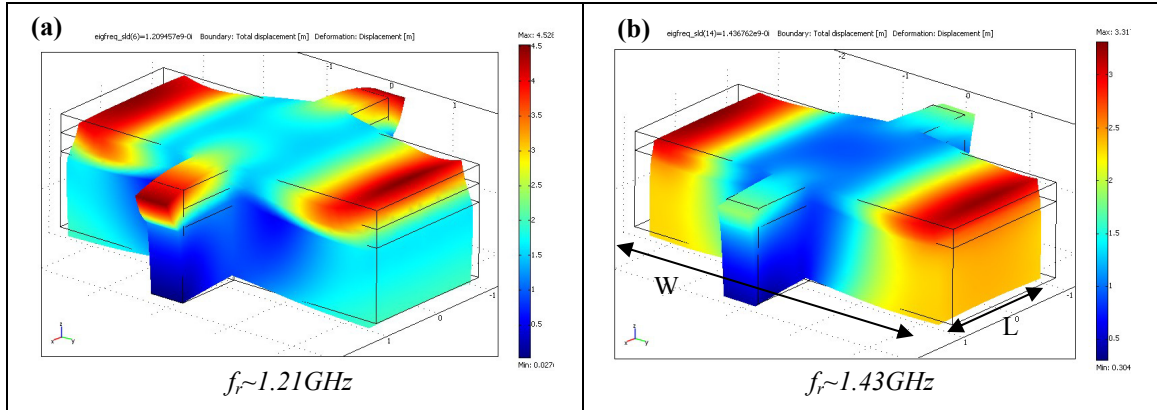


Figure 7.5: Width-extensional resonance mode-shapes of a  $5\mu\text{m}$  wide structure comprising a) diamond, oxide and ZnO layers; and b) diamond and ZnO layers (no oxide).

### 7.5 TPoD Resonator Measurement Results

Fabricated devices are connected to a network analyzer on a high frequency probe station using ground-signal-ground (GSG) microprobes. A typical measured frequency response plot for a device with  $40\mu\text{m}$  finger pitch excited in its third harmonic mode is shown in Fig. 7.6.

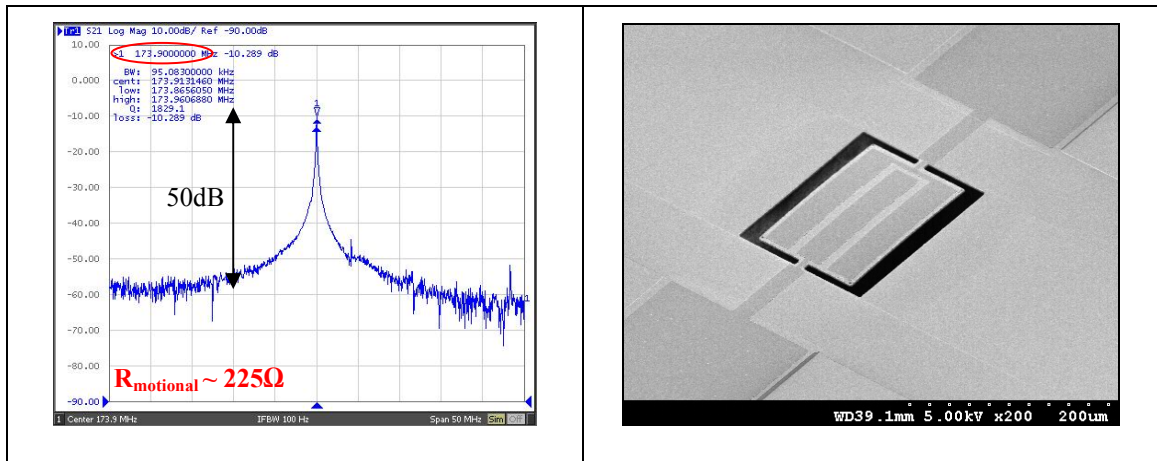


Figure 7.6: The frequency response plot and the SEM picture of a third-order TPoD resonator with a  $40\mu\text{m}$  finger pitch.

The measured resonance frequency is  $\sim 1.8\times$  higher than that of an identical design fabricated on a  $6\mu\text{m}$ -thick SOI substrate. The same trend of frequency increase was observed for devices with smaller finger pitch. Measured resonance frequencies and

quality factors from TPoS and TPoD resonators with various finger pitches are summarized in Table 7.1.

TABLE 7.1. SUMMARY OF THE MEASURED RESONANCE FREQUENCY AND THE QUALITY FACTOR FOR TPoS AND TPoD RESONATORS WITH VARIOUS FINGER PITCHES.

Finger Pitch( $\mu\text{m}$ )	Silicon		Diamond		Frequency ratio
	f(MHz)	Q	f(MHz)	Q	
40	95	3000	174	1800	1.8
20	186	1800	306	3000	1.6
10	370	1000	565	1300	1.5
5	640	800	1230	700	1.9

Since the thickness of the deposited NCD is not uniform across the wafer, different frequency ratios are observed for devices located at different spots on the wafer. The highest measured resonance frequency for each finger size is included in Table 7.1. Frequency response plots for TPoD devices presented in Table 1 are shown in Fig. 7.7.

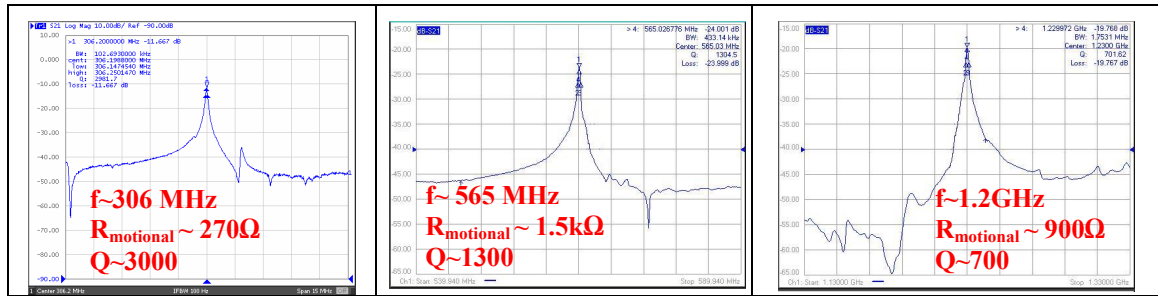


Figure 7.7: The frequency response plots measured from TPoD resonators with a 20, 10 and 5 $\mu\text{m}$  finger pitch.

The motional impedance of the 1.2GHz resonator is less than 1k $\Omega$ . This is a very small impedance compared to the reported values from capacitively transduced resonators in the same range of frequency [90]. It is expected that the motional resistance of the device is further reduced by thinning down or removing the interlayer buffer oxide in the resonator structure, and by optimizing the resonator dimensions for a clean mode-shape.

The temperature coefficient of frequency for a device with a 40 $\mu\text{m}$  finger pitch and a resonance frequency of ~155MHz is measured in a temperature and humidity

control chamber. The TCF plot is shown in Fig. 7.8. The TCF of this device was measured to be remarkably low ( $-2\text{ppm}/^\circ\text{C}$ ). By precisely controlling the oxide thickness, the overall TCF of these devices can potentially be engineered to a near zero value.

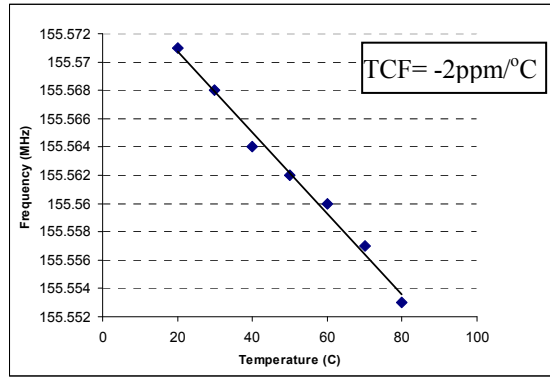


Figure 7.8: The TCF curve for a TPoD resonator with  $40\mu\text{m}$  finger pitch resonating at 155MHz.

## 7.6 Monolithic TPoD Filters

The NCD substrate was also used for fabrication of monolithic filters. The first resonant structure designed for filter application was a long and thin block consisting of a stack of ZnO on polished silicon dioxide on polycrystalline diamond. The targeted resonance mode of operation was the width-flexural mode. Incorporating two sets of isolated electrodes and separating them enables excitation of the dual flexural modes presented in Fig. 7.9. FEMLAB simulation results indicate a frequency spacing of 430kHz between the two modes at a center frequency of  $\sim 81\text{MHz}$  for a  $200\mu\text{m}$  long,  $20\mu\text{m}$  wide block consisting of a  $2\mu\text{m}$  diamond layer,  $0.5\mu\text{m}$  of oxide, and  $0.5\mu\text{m}$  of ZnO. The metal electrode is assumed to be a  $0.1\mu\text{m}$  layer of Pt (top plus bottom) and the electroded regions are  $14\mu\text{m}$  apart from each other. Block resonators with the same structural specifications in different lengths have been fabricated using a process flow briefly described before.

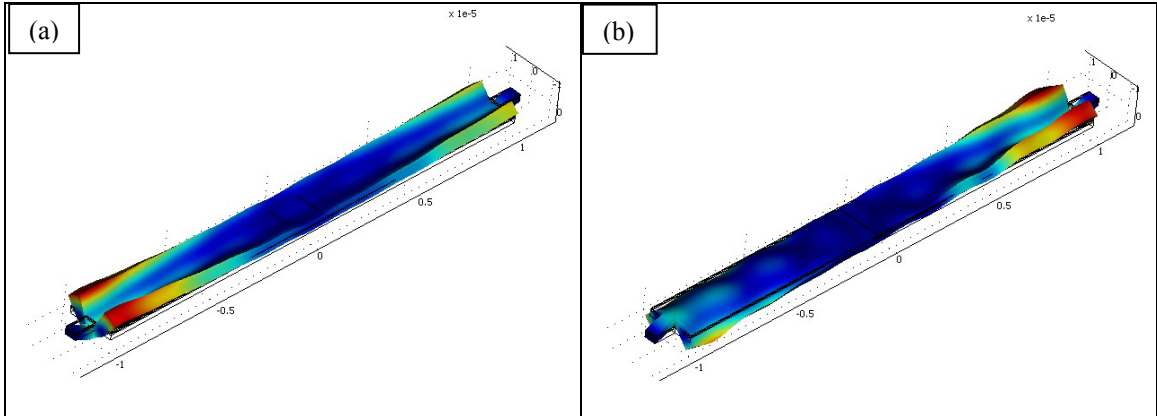


Figure 7.9: Simulated dual width-flexural mode-shapes in a monolithic ZnO-on-diamond micromachined filter: a) in-phase b) out-of-phase.

The SEM of Fig. 7.10 shows a 400 $\mu$ m long fabricated device with 14 $\mu$ m distance between the electrodes.

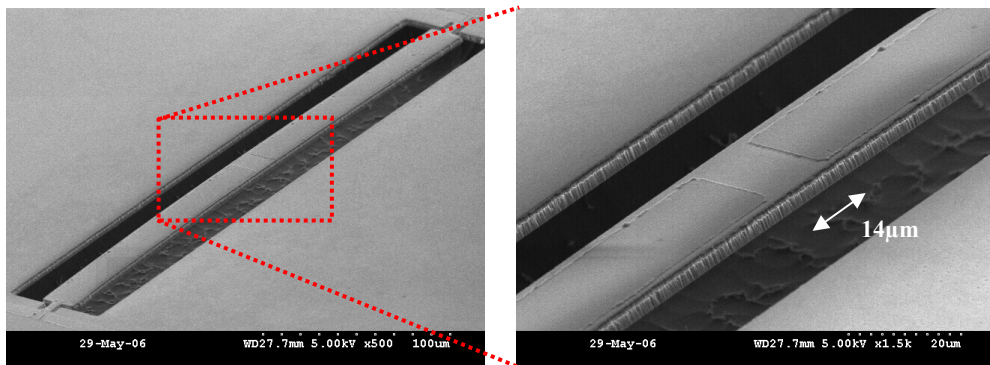


Figure 7.10: The SEM of a 400 $\mu$ m long, 20 $\mu$ m wide ZnO-on-diamond monolithic flexural TPOD filter

The frequency responses of Fig. 7.11 are measured from the device shown above operated in air. The center frequency is  $\sim$ 78MHz and the filter BW is  $\sim$ 570kHz.

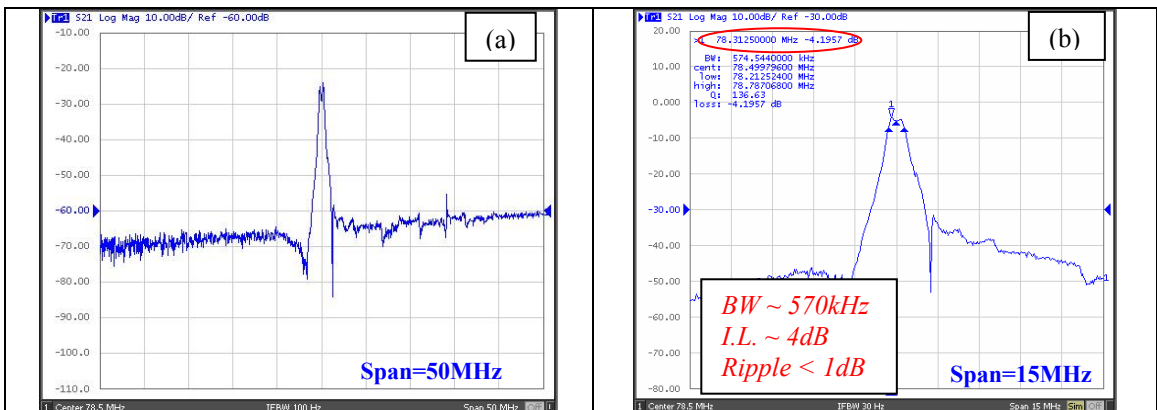


Figure 7.11: The frequency response of the device shown in Figure. 7.8 terminated with a) 50 $\Omega$  and b) 500 $\Omega$ .

Lateral-extensional resonance modes were targeted for higher frequency filters presented below. The crystalline grain size on the substrate used for these devices was smaller compared to the substrate used earlier. Therefore, the surface roughness was reduced to tens of nanometer and direct deposition of ZnO on the diamond surface was experimented again.

XRD rocking curves measured from a ZnO film sputtered on polished oxide and a film directly sputtered on the extra-fine grain NCD film are compared in Fig. 7.12. This time as opposed to the ZnO film deposited on the rough diamond layer, the rocking curve peak is detectable while deposited directly on the diamond. However, the FWHM angle is larger which is indicative of the wider angular distribution of c-plane crystal orientation around the surface normal.

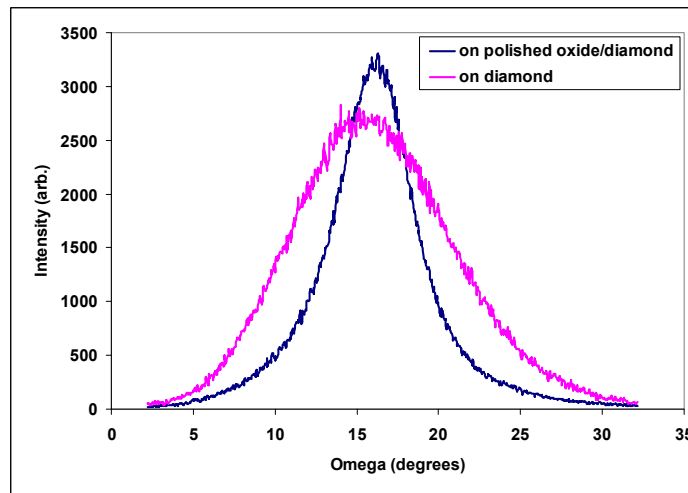


Figure 7.12: Overlapped rocking curves measured from ZnO sputtered directly on diamond with extra fine grains and on a buffer polished oxide layer.

The polished buffer oxide layer is preferably avoided for two important reasons; first is the low acoustic velocity of the oxide layer, which reduces the effect of diamond on increasing the operation frequency, and second is the effect of the oxide layer on the excited mode-shapes.

To study the effect of the buffer layer on the monolithic diamond filters one half of a wafer covered with a  $\sim 0.5\mu\text{m}$  polished oxide layer was masked with photoresist and dipped in buffered oxide etching (BOE) solution. After this step the photoresist was removed and the rest of the fabrication process flow was carried out on the wafer regularly. Consequently, half of the devices on the wafer had the oxide layer in their structure, where as the other half do not.

In the SEM pictures of Fig 7.13 the surface roughness of the ZnO sputtered on the polished oxide and sputtered directly on diamond are compared.

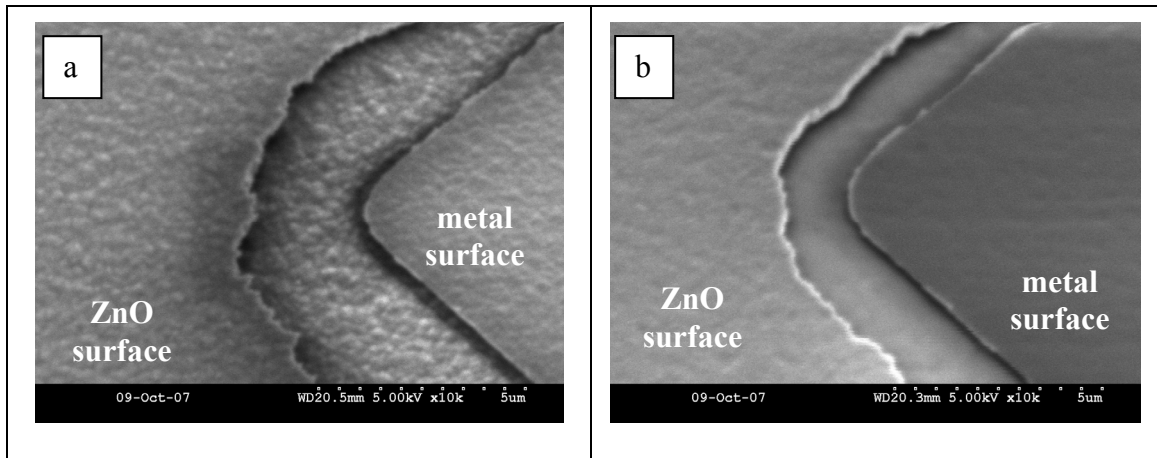


Figure 7.13: SEM pictures comparing surface topography of the ZnO and the metal layers deposited on; a) extra fine diamond b) polished oxide-covered diamond

In Fig 7.14 frequency response plots measured from the same monolithic filter with and without the oxide in the structure are presented. The device structure is the same as the device presented in the SEM picture of Fig. 6.9. It is readily clear how the oxide layer affects the response. The resonance frequency is higher compared to the device fabricated on silicon in both cases. However, the improvement ratio is relatively small when the oxide layer is present (490/440) and larger without the oxide (680/440).



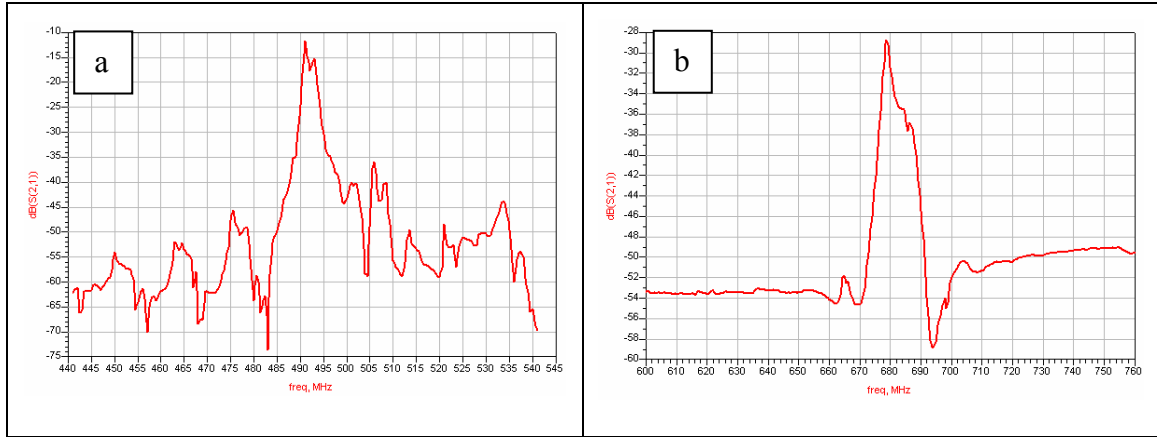


Figure 7.14: Frequency responses measured from TPoD filters with the same geometries as the device in SEM of Fig. 6.9; a) with and b) without the polished oxide in the stack

On the other hand, the insertion loss of the filter is much larger for the device fabricated directly on the diamond substrate which can be directly correlated to the quality of the ZnO sputtered on diamond. At the same time number of spurious modes excited on the device with oxide is significantly larger.

The same improvement in resonance frequency was observed on the TPoD filters with the same size as the one presented in the SEM picture of Fig. 6.10. A typical frequency response measured from a device without polished oxide in the stack is presented in Fig. 7.15. The measured center frequency is increased with a (900/640) ratio.

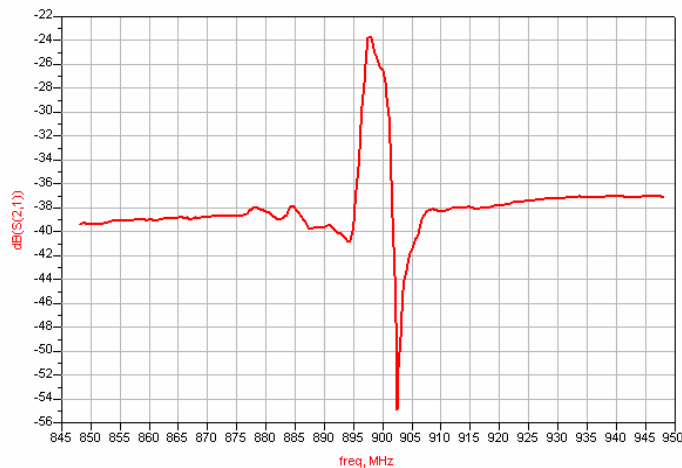


Figure 7.15: The frequency response of a TPoD monolithic filter with the same size as the device shown in the SEM of Fig. 6.10.

## 7.7 ZnO-on-Diamond Resonant Mass Sensors

As shown in Fig. 7.16, the resonant structure consists of a central block and two annexed sensing platforms attached to it via separation beams. This design is utilized to minimize the change in the effective stiffness of the resonator when an extra mass is absorbed to the sensing platform [97].

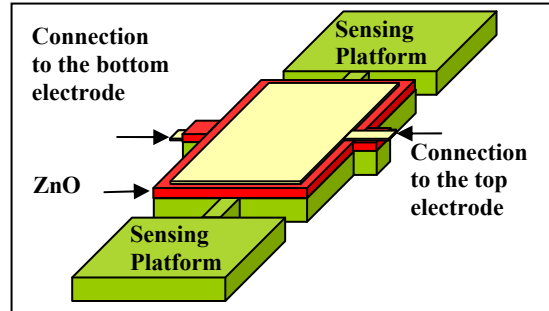


Figure 7.16: The piezoelectrically-transduced lateral resonant mass sensor.

The structural material (polycrystalline diamond in this case) is coated with a thin piezoelectric layer (ZnO). The piezoelectric layer covering the central block is sandwiched between two metal electrodes. The top electrode can be split into two separate electrodes for two-port operation of the device. However, by doing so, the available actuation/sense area is reduced to half, increasing the motional impedance of the resonator. The ZnO layer can be either removed or kept intact on the sensing platform depending on the application and the receptor coating.

An alternating electrical field applied across the ZnO layer introduces an in-plane strain field through the  $d_{31}$  piezoelectric coefficient of ZnO. When the frequency of the applied electrical signal matches the lateral bulk-extensional resonance mode of the structure, the vibration amplitude and the current passing through the electrodes are maximized.

When some amount of mass ( $\Delta M$ ) is absorbed to the sensing platform the change in the frequency can be approximated by Sauerbrey equation (assuming  $\Delta K/K_{eff} \ll \Delta M/M_{eff}$ ) [100]:

$$\Delta f \cong -\frac{\Delta M}{2 M_{eff}} \cdot f_c . \quad (7.2)$$

In other word, sensitivity of the sensor can be written as:

$$S = \frac{\Delta f}{\Delta M} = -\frac{f_c}{2 M_{eff}} . \quad (7.3)$$

By increasing the stiffness of the resonator structural material (using diamond) while reducing the effective mass, the natural frequency and hence the sensitivity of the device are increased. However, this may not result in a better mass detection resolution since other factors such as  $Q$  of the resonator and electrical noise of the interface circuit will also contribute to the overall resolution of the sensor [96]. Improvement in the mass resolution can only be claimed after performing a system-level measurement, where an oscillator circuit is included.

### 7.7.1 Simulation Results

The first length-extensional resonance mode of a device with  $70\mu\text{m}$  long central-block and  $30\mu\text{m}$  long sensing platform is shown in Fig. 7.17 (simulated in FEMLAB).

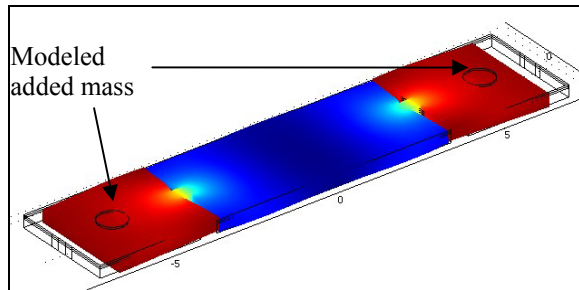


Figure 7.17: Length-extensional mode-shapes of a device with  $70\mu\text{m}$  long central block and two  $30\mu\text{m}$  long sensing platforms.

A resonance frequency of 36MHz is predicted for a structure consisting of diamond/oxide/ZnO with 2.5/0.5/0.5 $\mu\text{m}$  thicknesses, respectively. As seen in the mode-shape, the separation beams undergo the highest deformation in the structure and the two ends of the sensing platforms mostly experience a translational motion, which minimizes change in the stiffness induced by the absorbed mass. Moreover, the maximum vibration amplitude occurs on the sensing platform, which helps improving the mass sensitivity.

To predict the sensitivity of the sensor, an extra piece of mass in the shape of a thin (0.5 $\mu\text{m}$ ) cylinder with a radius of 4 $\mu\text{m}$  was added on top of the sensing platform. The density of the material (which the cylinder is made of) was altered gradually and resonance frequency was simulated each time. A mass sensitivity of 1100Hz/pg is predicted for the length-extensional resonance mode of the devices. In the next section, the predicted frequency change as a function of added mass is compared to the measurement results.

### **7.7.2 Experimental Results**

Frequency response of the fabricated resonators is measured using an E5071B Agilent network analyzer after wirebonding the device to a custom-made printed circuit board (PCB). Extra mass in the shape of a cylinder (made of Pt) is then deposited on the device sensing platform using a focused ion beam (FIB) tool. By using FIB, desirable amount of mass can be deposited on the device without damaging its functionality. This is a relatively accurate method for characterizing the sensitivity of mass sensors while the device is not yet coated by receptor material.

Figure 7.18 shows an SEM of a fabricated device after deposition of Pt on the sensing platforms. Platinum deposition is performed on four devices. The radius of the platinum cylinder is kept constant for all devices and the thickness is increased from 100 to 150, 200, and 300nm. The amount of the added mass is calculated by multiplying the approximate cylinder volume with the density of material. Since the deposited material by FIB is not 100% Pt and contains a large amount of Carbon and other materials (~50%) [101], we used density of platinum for half of the volume and assumed that the rest of the volume is filled with carbon.

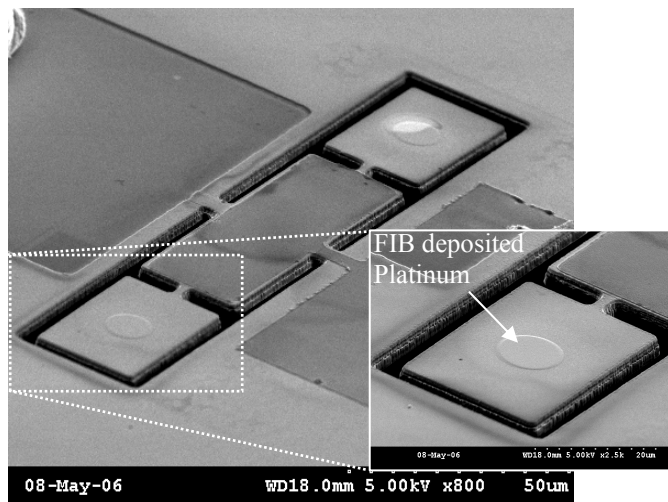


Figure 7.18: The SEM of the TPoD resonant mass sensor after FIB Platinum deposition.

After deposition of platinum, devices are wirebonded again and the resonance frequency is measured. Figure 7.19 shows the measured frequency response of a device with 70 $\mu$ m long central block and 30 $\mu$ m long sensing platform, (a) before, and (b) after ~48pg platinum deposition.

The resonance frequency is reduced by ~65kHz after Pt deposition. The motional impedance of the devices was measured to be in 20k $\Omega$  range with quality factor values >3500 at ~40MHz in air (before Pt deposition). Measured quality factors after deposition

of Pt were lower compared to the values before deposition. This could be caused by deposition of a very thin layer of metal-organic contamination on the device surfaces in the FIB chamber.

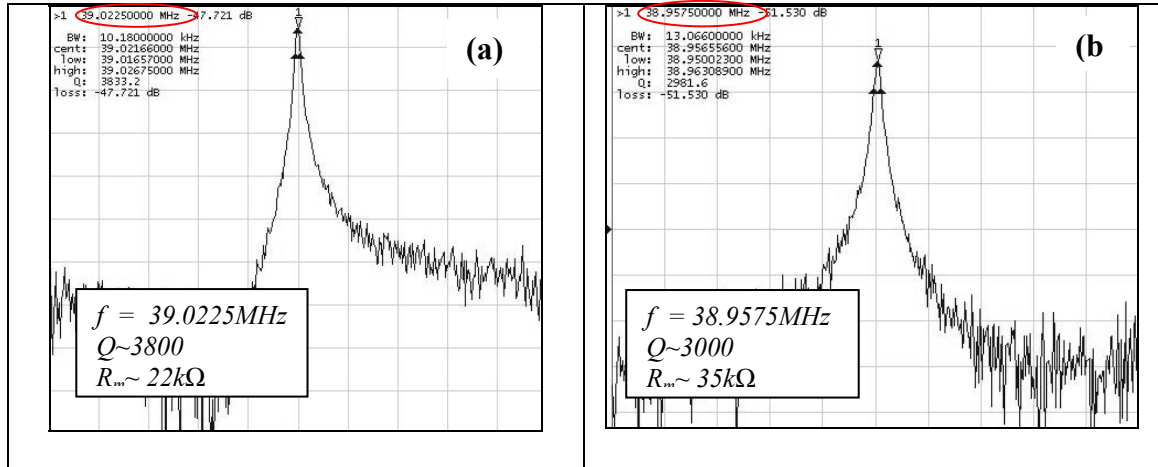


Figure 7.19: Resonance responses of the lateral-extensional resonant mass sensor, (a) before, and (b) after ~48pg platinum deposition.

The frequency change as a function of the mass deposited on the device is compared to the theoretical values predicted by FEMLAB in Fig. 7.20. Sensitivity of ~1kHz/pg is measured for the 39MHz devices, which is in good agreement with the simulated values.

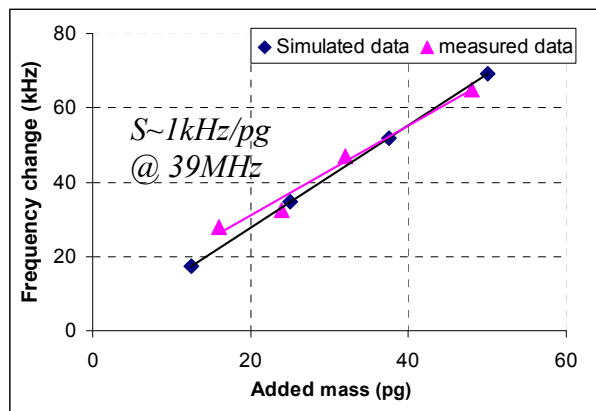


Figure 7.20: Comparison between the simulated and measured sensitivity of the TPoD mass sensor.

The TCF for these devices is measured using a temperature/humidity control chamber. Devices with thicker oxide exhibited lower TCF values (and lower resonance frequencies as well). The resulted data points for a resonator with a resonance frequency of ~39MHz are plotted in Fig. 7.21, showing a TCF value of ~-6ppm/°C for the device.

In order to further reduce the motional impedance of the resonant mass sensor the width of the device can be increased, which has very little contribution in the resonance frequency while it increases the electrode area and lowers the impedance.

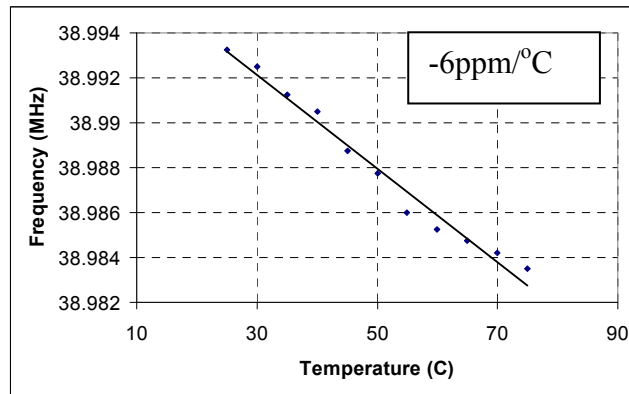


Figure 7.21: The measured TCF for a ZnO-on-diamond mass sensor.

## 7.8 Conclusion

A new class of micromachined resonators called the thin-film piezoelectric-on-diamond (TPoD) was introduced. Large electromechanical coupling of the piezoelectric transduction mechanism combined with high acoustic velocity and low acoustic loss of nanocrystalline diamond structure gives TPoD resonators an edge compared to other available technologies. Application of these resonator in monolithic filters and mass sensors were demonstrated and a significant frequency enhancement ( $>1.5\times$ ) compared to TPoS devices fabricated on SOI substrate was observed.

## CHAPTER 8

### CONCLUSION AND FUTURE DIRECTION

In this dissertation thin-film piezoelectric-on-substrate (TPoS) technology were introduced as a platform for implementation of high  $Q$ , highly linear, and low motional impedance resonators that can be utilized in many applications such as low-noise stable clock generators, narrow bandwidth analog filters, and resonant sensors. Our contribution in this thesis can be summarized as follows:

#### 8.1 High-Frequency TPoS Resonators on SOI

In this work SOI substrate was mostly used as the starting substrate to fabricate TPoS resonators. Novel lateral bulk acoustic resonant structures such as high-order and coupled-arrayed resonators were designed, fabricated and tested in order to expand the useful range of the operation frequency. Very low motional impedance high  $Q$  resonators at frequencies up to  $\sim 500\text{MHz}$  were demonstrated which can serve the clock generating needs of existing high frequency electronic devices and also open room for new applications to emerge.

It was demonstrated that the inclusion of the silicon substrate in the resonant structure improves the linearity and quality factor of the piezoelectric resonators which in turn enhances the phase noise characteristic of the oscillators built based on these devices. The low motional impedance of these resonators, on the other hand, simplifies the required sustaining amplifier for oscillator application and significantly reduces the power consumption. Simple single transistor oscillators were assembled at high frequencies which consumed less than  $300\mu\text{W}$  of power.



Moreover, it was noticed that the signal phase is inverted at the high-order resonance mode of a two-port high-order lateral-extensional TPoS resonator. This unique feature was explored for realization of a dual frequency oscillator where a two-stage amplifier could select between the fundamental and the higher order resonance modes of the structure by alternatively introduce  $0^\circ$  and  $180^\circ$  phase-shift across the amplification path.

## **8.2 Monolithic TPoS filters**

High frequency lateral-extensional monolithic filters were introduced in this dissertation for the first time. A monolithic filter is a coupled-mode resonant system implemented on a single resonant structure. Thickness-mode monolithic quartz crystal filters have been commercially available for many years but this technique has never been applied to thin-film resonator technology and especially not for lateral-mode devices. Using the lateral-extensional mode will provide the means for compact implementation of multiple-frequency monolithic filters on a single substrate which is attractive for applications in which, arrays of filters at various center frequencies are required. Although, TPoS structure was used as the platform to implement these filters the technique introduced in this work can be applied to any other type of micromachined resonant device. Thickness-modes monolithic TPoS filters were also demonstrated. These filters exhibit operation frequencies up to a few GHz.

By changing the lateral dimension of these filters both coarse and fine frequency offset was achieved in laterally-excited and thickness mode devices. The BW of a monolithic thickness-mode TPoS filter was also alternated by changing the top electrode pattern (changing the finger pitch in an IDT design). Using this technique narrow BW

lateral mode filters at 3GHz with filter Q values in the range of 150 to 900 were demonstrated.

### **8.3 Thin-Film Piezoelectric-on-Diamond Devices**

Another new class of micromachined resonators called the thin-film piezoelectric-on-diamond (TPoD) was introduced in this dissertation. A thin layer of nanocrystalline diamond (NCD) is used in the stack of the resonant structure in order to take advantage of the high acoustic velocity of diamond. This way the resonance frequency of the thin-film piezoelectric resonator is increased while the limitation on lithographically-defined features of the resonator is relaxed. Also, the lower TCF of the diamond makes it easier for a TPoD resonator to be compensated for the frequency change with temperature, compared to the devices containing silicon in their structure.

Application of TPoD resonators in monolithic filters and mass sensors were demonstrated and significant ( $>1.5\times$ ) frequency enhancement compared to TPoS devices fabricated on SOI substrate was observed.

### **8.4 Future Research**

TPoS resonators have proved to offer immediate advantages over other existing micro-resonator technologies by providing high linearity, low motional impedance and relatively high quality factor at high frequencies. However, energy loss mechanisms limiting the quality factor of these devices are not clearly understood. By studying the dominant loss mechanism in these resonators we might find a way to improve the quality factor of these resonators and in that case the performance offered by these devices will be hard to reach by other competing technologies.

Also, the insertion loss of TPoS filters demonstrated in this work is far from perfect. The limiting factor for implementation of low-loss filters at this point is identified to be the low quality of the piezoelectric film (ZnO) used in these devices. The effective electromechanical coupling in these devices is small compared to what can be ideally achieved from ZnO (single crystal properties) and also the sputtered film is leaky. Therefore, application of commercially-available AlN thin sputtered films is recommended to study the limits for implementation of low insertion loss high frequency filters. Alternative resonant structure designs should also be attempted in order to effectively suppress the spurious modes in the frequency response plot.

The dual-mode oscillators based on a TPoS resonator can be further studied for implementation of extremely accurate temperature sensors and the self temperature-sensing method utilized in dual-harmonic quartz crystal oscillators can also be employed on these devices to assemble oven controlled temperature-stable oscillators using the resonator as the temperature sensor and the heater (by passing current through the silicon).

Using diamond as the structural material in the thin-film piezoelectric-on-substrate technology is yet to be fully explored. AlN is suggested to be used as the piezoelectric material of choice in these devices for the same advantages mentioned earlier and further because of lesser mismatch in the acoustic velocity of diamond and AlN. This way, the out-of-plane displacement of the resonator while resonating in an extensional mode is reduced and therefore the effective electromechanical coupling is improved. Alternative fabrication methods and materials should be employed to provide for a smooth surface on the NCD layer in order to promote growth of c-plane grains.

Using a thin polished AlN layer as the buffer layer to compensate for the roughness of the NCD layer would be an attractive solution for this problem.

Finally, on the mass-sensing front, alternative structural designs that minimize the effect of viscous damping on the resonator should be studied, in order to enable application of TPoS resonators in liquids. Shear in-plane resonance modes if excited in the structure can potentially fulfill the in-liquid operation criteria. Miniaturized, high  $Q$ , high frequency, low impedance, gravimetric mass-sensors that can operate in liquid are the ultimate bio-sensing devices that has been long wished for by biological researchers.

## REFERENCES

---

- [1] A.G. Manke, "Crystal oscillators in communication receivers," *IRE Transactions on Vehicular Communications*, vol.7, pp. 10- 15, Dec. 1956.
- [2] D.F. Ciccolella, L.J Labrie, "High frequency crystal units for use in selective networks and their proposed application in filters suitable for mobile radio channel selection," *Transactions of the IRE Professional Group on Vehicular Communications*, vol.3, pp. 118- 128, Jun 1953.
- [3] R. Abdolvand, H. Mirilavasani, F. Ayazi, "A low-voltage temperature-stable micromechanical piezoelectric oscillator," *International Conference on Solid-State Sensors, Actuators and Microsystems ( TRANSDUCERS'07)*, pp.53-56, 10-14 June 2007.
- [4] R. Abdolvand, G. K. Ho, J. Butler, and F. Ayazi, "ZnO-on-nanocrystalline diamond lateral bulk acoustic resonators," *Proc. 20th IEEE International Conference on Micro Electro Mechanical Systems (MEMS'07)*, Kobe, Japan, pp. 795-798, Jan. 2007.
- [5] R. Abdolvand, F. Ayazi, "Monolithic thin-film piezoelectric-on-Substrate filters," *IEEE/MTT-S International Microwave Symposium*, pp.509-512, 3-8 June 2007.
- [6] R. Abdolvand, Z. Hao, F. Ayazi, "A temperature-compensated ZnO-on-diamond resonant mass sensor," *Proc. 5<sup>th</sup> IEEE Conference on Sensors*, pp.1297-1300, Oct. 2006.
- [7] M. Hikita, T. Tabuchi, A. Sumioka, "Miniaturized SAW devices for radio communication transceivers," *IEEE Transactions on Vehicular Technology*, vol. 38, Issue 1, pp. 2-8, 1989.
- [8] C. K. Campbell, "Applications of surface acoustic and shallow bulk acoustic wave devices," *Proceedings of the IEEE*, vol.77, pp.1453-1484, Oct 1989.
- [9] J. Cohn, R. Chandler, "System improvements through use of RF crystal filters," *IEEE Transactions on Vehicular Communications*, vol.15, pp. 54- 61, Mar 1966.
- [10] A. Hajimiri, T. H. Lee, "A general theory of phase noise in electrical oscillators," *IEEE Journal of Solid-State Circuits*, vol.33, no.2, pp.179-194, Feb 1998.

- 
- [11] B. Razavi, K.F. Lee, R.H. Yan, "Design of high-speed, low-power frequency dividers and phase-locked loops in deep submicron CMOS," *IEEE Journal of Solid-State Circuits*, vol.30, pp.101-109, Feb 1995.
- [12] H. C. Nathanson, W. E. Newell, R. A. Wickstrom, and J. R. Davis, "The resonant gate transistor," *IEEE Trans. Electron Devices*, vol. ED-14, pp. 117–133, 1967.
- [13] W. C. Tang, T. C. Nguyen, and R. T. Howe, "Laterally driven polysilicon resonant microstructures," *Sensors and Actuators*, vol. 20, pp. 25–32, 1989.
- [14] F. Ayazi, S. Pourkamali, G. K. Ho, R. Abdolvand, "High-aspect-ratio SOI vibrating micromechanical resonators and filters," *Digest of IEEE International Microwave Symposium ( MTT-S)*, pp.676-679, June 2006.
- [15] C. T.-C. Nguyen, "Vibrating RF MEMS for next generation wireless applications," *Proceedings of IEEE Custom Integrated Circuits Conf.*, Orlando, FL, Oct. 2004, pp. 257-264.
- [16] R. Ruby, P. Bradley, D. Clark, D. Feld, T. Jamneala, K. Wang, "Acoustic FBAR for filters, duplexers and front end modules," *Digest of IEEE International Microwave Symposium (MTT-S)*, vol.2, pp. 931- 934 , June 2004.
- [17] S. Pourkamali, A. Hashimura, R. Abdolvand, G.K. Ho, A. Erbil, F. Ayazi, "High-Q single crystal silicon HARPSS capacitive beam resonators with self-aligned sub-100-nm transduction gaps," *Journal of Microelectromechanical Systems*, vol.12, no.4, pp. 487- 496, Aug. 2003.
- [18] Lin Yu-Wei, Lee Seungbae, Ren Zeying, C.T.C. Nguyen, "Series-resonant micromechanical resonator oscillator," *Technical Digest International IEEE Electron Devices Meeting( IEDM '03)*, pp. 39.4.1-39.4.4, 8-10 Dec. 2003.
- [19] Zhili Hao, S. Pourkamali, F. Ayazi, "VHF single-crystal silicon elliptic bulk-mode capacitive disk resonators-part I: design and modeling," *Journal of Microelectromechanical Systems*, vol.13, no.6, pp. 1043-1053, Dec. 2004.

- 
- [20] S. Pourkamali, G. K. Ho, F. Ayazi, "Low-impedance VHF and UHF capacitive silicon bulk acoustic wave resonators—Part I: concept and fabrication," *IEEE Transactions on Electron Devices*, vol.54, no.8, pp.2017-2023, Aug. 2007.
- [21] M. U. Demirci, C. T.-C. Nguyen, "Mechanically corner-coupled square microresonator array for reduced series motional resistance," *Journal of Microelectromechanical Systems*, vol.15, no.6, pp.1419-1436, Dec. 2006.
- [22] S. Pourkamali, G. K. Ho, F. Ayazi, "Low-impedance VHF and UHF capacitive silicon bulk acoustic-wave resonators—Part II: measurement and characterization," *IEEE Transactions on Electron Devices*, vol.54, no.8, pp.2024-2030, Aug. 2007.
- [23] S. A. Bhave, R. T. Howe, "Silicon nitride-on-silicon bar resonator using internal electrostatic transduction," *Digest of the 13th International Conference on Solid-State Sensors, Actuators and Microsystems (TRANSDUCERS '05)*, vol.2, pp. 2139-2142, 5-9 June 2005.
- [24] Li Yu-Wei, Li Sheng-Shian, Xie Yuan, Ren Zeying, C.T.-C. Nguyen, "Vibrating micromechanical resonators with solid dielectric capacitive transducer gaps," *Proceedings of the IEEE International Frequency Control Symposium and Exposition*, pp. 128-134, 29-31 Aug. 2005.
- [25] V. Kaajakari, A. T. Alastalo, T. Mattila, "Electrostatic transducers for micromechanical resonators: free space and solid dielectric," *IEEE Transactions on Ultrasonics, Ferroelectrics and Frequency Control*, vol.53, no.12, pp.2484-2489, December 2006.
- [26] K.M. Lakin, "Thin film resonator technology," *IEEE Transactions on Ultrasonics, Ferroelectrics and Frequency Control*, vol.52, no.5, pp. 707- 716, May 2005.
- [27] P.V. Wright, "A review of SAW resonator filter technology," *Proceedings of IEEE Ultrasonics Symposium* , pp.29-38 , Oct 1992.
- [28] P. Kirby, Qing-Xin Su, E. Komuro, M. Imura, Qi Zhang; R. Whatmore, "High frequency thin film ferroelectric acoustic resonators," *IEE Colloquium on Microwave Filters and Multiplexers (Ref. No. 2000/117)*, 2000.

- 
- [29] R. M. White, "Acoustic sensors for physical, chemical and biochemical applications," *Proceedings of the IEEE International Frequency Control Symposium*, pp.587-594, 27-29 May 1998.
- [30] T Fujii, S. Watanabe S, M. Suzuki, "Application of lead-ziconate-titanate thin-film displacement sensors for atomic-force microscope," *Journal of Vacuum Sciences and Technology B*, vol. 13, no 3, pp. 1119-1122, May 1995.
- [31] R.J. Nunamaker, "Frequency control devices for mobile communications," *Proc. 25th Ann. Freq. Cont. Symp.*, April 1971.
- [32] J. F. Rosenbaum, *Bulk Acoustic Wave Theory and Devices*, Boston: Artech House, 1988.
- [33] J. D. Larson, P. D. Bradley, S. Wartenberg, R. C. Ruby, "Modified Butterworth-Van Dyke circuit for FBAR resonators and automated measurement system," *IEEE Ultrasonics Symposium*, vol.1, pp.863-868, Oct 2000.
- [34] S. Malinowski, D. Schennberg, "HF and VHF crystal filters," *16th Annual Symposium on Frequency Control*, pp. 347- 372, 1962.
- [35] B. D'Albaret, P. Siffert, "Recent advances in UHF crystal filters," *36th Annual Symposium on Frequency Control*, pp. 405- 418, 1982.
- [36] M. Dubois, C. Billard, J. Carpentier, P. Vincent, G. Parat, C. Muller, "Above-IC FBAR technology for WCDMA and WLAN applications," *IEEE Ultrasonics Symposium*, vol.1, pp. 85- 88, 18-21 Sep. 2005.
- [37] C.T.-C. Nguyen, "Micromechanical resonators for oscillators and filters," *Proceedings of IEEE Ultrasonics Symposium*, vol.1, pp.489-499, Nov. 1995.
- [38] K. Wang; C.T.-C Nguyen, "High-order medium frequency micromechanical electronic filters," *Journal of Microelectromechanical Systems* , vol.8, no.4, pp.534-556, Dec 1999.
- [39] F.D. Bannon, J.R. Clark, C.T.-C. Nguyen, "High-Q HF microelectromechanical filters," *IEEE Journal of Solid-State Circuits*, vol.35, no.4, pp.512-526, Apr 2000.



- 
- [40] S. Pourkamali, R. Abdolvand, F. Ayazi, "A 600 kHz electrically-coupled MEMS bandpass filter," *IEEE 16<sup>th</sup> Annual International Conference on Micro Electro Mechanical Systems (MEMS'03)*, pp. 702- 705, Jan. 2003.
- [41] G. Piazza, P.J. Stephanou, M.B.J. Wijesundara, A.P. Pisano, "Single-chip multiple-frequency filters based on contour-mode aluminum nitride piezoelectric micromechanical resonators," *Digest of Technical Papers The 13th International Conference on Solid-State Sensors, Actuators and Microsystems (TRANSDUCERS'05)*, vol.2, pp. 2065- 2068, 5-9 June 2005.
- [42] G.K. Ho, R. Abdolvand, "High-order composite bulk acoustic resonators," *Proc. IEEE Micro Electro Mechanical Systems Conference, Japan*, Jan. 2007, pp. 791-794
- [43] F. S. Hickernell, "ZnO processing for bulk- and surface-wave devices," *IEEE Ultrasonics Symposium*, pp. 785-794, 1980.
- [44] C. Caliendo, A. Cimmino, P. Imperatori, E. Verona, "Optimization of the sputtering deposition parameters of highly oriented piezoelectric AlN films," *IEEE Ultrasonics Symposium*, vol.1, pp.345-348 vol.1, Oct 2000.
- [45] V. Kaajakari, T. Mattila, A. Oja, H. Seppa, "Nonlinear limits for single-crystal silicon microresonators," *Journal of Microelectromechanical Systems*, vol.13, no.5, pp. 715-724, Oct. 2004.
- [46] E. Anastassakis, A. Cantarero, and M. Cardona, "Piezo-Raman measurements and anharmonic parameters in silicon and diamond," *Phys. Rev. B*, vol. 41, issue 11, pp. 7529 – 7535, Apr. 1990.
- [47] P. Lepkowski, J. A. Majewski, G. Jurczak, "Nonlinear elasticity in III-N compounds: Ab initio calculation," *Physical Review B*, vol. 72, issue 24, Dec. 2005.
- [48] J. Nosek, "Drive level dependence of the resonant frequency in BAW quartz resonators and his modeling," *IEEE Trans. Ultrasonics, Ferroelectrics, Freq. Control*, vol. 46, pp. 823–829, July 1999.
- [49] J. B. Starr, "Squeeze-film damping in solid-state accelerometers," *Technical Digest 4<sup>th</sup> IEEE Solid-State Sensor and Actuator Workshop*, pp.44-47, 4-7 Jun 1990.

- 
- [50] Z. Hao, A. Erbil, and F. Ayazi, "An analytical model for support loss in micromachined beam resonators with In-plane flexural vibrations," *Sensors and Actuators A*, vol. 109, pp. 156-164, Dec. 2003.
- [51] C. Zener, "Internal friction in solids, I: theory of internal friction in reeds," *Phys. Rev.*, vol. 52, pp. 230-235, Aug. 1937.
- [52] R. Abdolvand, H. Johari, G. K. Ho, A. Erbil, F. Ayazi, "Quality factor in trench-refilled polysilicon beam resonators," *Journal of Microelectromechanical Systems*, vol. 15, no. 3, pp. 471-478, June 2006.
- [53] L. T. Claiborne, R. B. Hemphill, and N. G. Einspruch, "Ultrasonic attenuation in ZnO", *The Journal of the Acoustical Society of America*, vol. 45, issue 6, pp. 1352-1355, Jun 1969.
- [54] D.K. Pandey, Devraj Singh, R.R. Yadav, "Ultrasonic wave propagation in IIIrd group nitrides," *Applied Acoustics*, vol. 68, issue 7, pp. 766-777, July 2007.
- [55] R. A. Moore, J. T. Haynes, B. R. McAvoy, "High overtone bulk resonator stabilized microwave sources," *IEEE Ultrasonics Symposium*, pp. 414-424, 1981.
- [56] G. G. Sahasrabudhe, S. D. Lambade, "Study of elastic and acoustic nonlinearities in solids at room temperature," *Journal of Physics and Chemistry of Solids*, vol. 59, Issue 5, pp. 789-808, May 1998.
- [57] S. Trolier-McKinstry, P. Muralt, "Thin film piezoelectric material for MEMS," *Journal of Electroceramics*, vol. 12, No. 1-2, Jan. 2004
- [58] Tai-Ran Hsu, *MEMS Packaging*, Institution of Electrical Engineers, 2004
- [59] S. Singh, R.S. Srinivasa, S.S. Major, "Effect of substrate temperature on the structure and optical properties of ZnO thin films deposited by reactive rf magnetron sputtering," *Thin Solid Films*, vol. 515 (24), pp. 8718-8722, Oct. 2007.
- [60] K. R. Williams, K. Gupta, M. Wasilik, "Etch rates for micromachining processing-Part II," *Journal of Microelectromechanical Systems*, vol. 12, no. 6, pp. 761-778, Dec. 2003.
- [61] T. Yokoyama, T. Nishihara, S. Taniguchi, M. Iwaki, Y. Satoh, M. Ueda, T. Miyashita, "New electrode material for low-loss and high-Q FBAR filters," *IEEE Ultrasonics Symposium*, vol. 1, pp. 429-432, 23-27 Aug. 2004.

- 
- [62] S. Mishin, D. R. Marx, B. Sylvia, V. Lughi, K. L. Turner, D. R. Clarke, "Sputtered AlN thin films on Si and electrodes for MEMS resonators: relationship between surface quality microstructure and film properties," *IEEE Symposium on Ultrasonics*, vol.2, pp. 2028-2032, 5-8 Oct. 2003.
- [63] E.A. Gulbransen, W.S. Wysong, "Thin oxide films on molybdenum," *Trans. AIME Met. Div.*, vol. 175, pp. 628-647, 1948.
- [64] F. S. Hickernell, "Measurement techniques for evaluating piezoelectric thin films," *Proceedings IEEE Ultrasonics Symposium*, vol.1, pp. 235-242, 3-6 Nov 1996.
- [65] F. C. M. Van De Pol, F. R. Blom, T. J. A. Popma, "RF planar magnetron sputtered ZnO films I: structural properties," *Thin Solid Films*, no. 204, pp. 349-364, 1991.
- [66] J. G. E. Gardeniers, Z. M. Rittersma, and G. J. Burger, "Preferred orientation and piezoelectricity in sputtered ZnO films," *Journal of Applied Physics*, vol. 83, Issue 12, pp. 7844-7854, Jun 1998.
- [67] F. Laemer and A. Schilp of Robert Bosch GmbH, "Method of anisotropically etching silicon," US-Patent No. 5501893.
- [68] J. Hopkins, *et. al.* , Method and apparatus for etching a substrate, US patent No. 6,187,685.
- [69] K. M. Lakin, "Modeling of thin film resonators and filters," *IEEE MTT-S International Microwave Symposium Digest*, pp.149-152 vol.1, 1-5 Jun 1992.
- [70] K. M. Lakin, "Fundamental properties of thin film resonators," *Proceedings of the 45th Annual Symposium on Frequency Control*, pp.201-206, 29-31 May 1991.
- [71] K. Sundaresan, G. K. Ho, S. Pourkamali, F. Ayazi, "A low phase noise 100MHz silicon BAW reference oscillator," *IEEE Custom Integrated Circuits*, Sept. 2006, pp. 841-844A.
- [72] Y. Lin, S. Lee, S-S Li, Y. Xie, Z. Ren, C.T.-C. Nguyen, "Series-resonant VHF micromechanical resonator reference oscillators," *IEEE Journal of Solid-State Circuits*, vol. 39, pp. 2477- 2491, Dec 2004.
- [73] K.M. Lakin, K.T. McCarron, J.F. McDonald, "Temperature compensated bulk acoustic thin film resonators," *IEEE Ultrasonics Symposium*, vol.1, pp.855-858, Oct 2000.

- 
- [74] G. Carlotti, L. Doucet, M. Dupeux, "Elastic properties of silicon dioxide films deposited by chemical vapour deposition from tetraethylorthosilicate," *Thin Solid Films*, vol. 296, Issues 1-2, pp. 102-105, March 1997.
- [75] K.M. Lakin, "Fundamental properties of thin film resonators," *Proceedings of the 45th Annual Symposium on Frequency Control*, pp.201-206, May 1991.
- [76] H. M. Lavasani, R. Abdolvand, and F. Ayazi, "A 500MHz low phase-noise AlN-on-silicon reference oscillator," *Proc. IEEE CICC*, pp. 599-602, Sep. 2007.
- [77] J. R. Vig, "Dual-mode oscillators for clocks and sensors," *Procs. IEEE Ultrasonics Symposium*, vol.2, pp.859-868, 1999.
- [78] S. S. Schodowski, "Resonator self-temperature-sensing using a dual-harmonic-mode crystal oscillator," *Proc. of the 43rd Annual Symposium on Frequency Control*, pp.2-7, Jun. 1989.
- [79] F. Ayazi, S. Pourkamali, G.K. Ho, R. Abdolvand, "High-aspect-ratio SOI vibrating micromechanical resonators and filters," *Digest of IEEE International Microwave Symposium*, pp.676-679, June 2006.
- [80] L. Sheng-Shian, M.C. Demirci, L. Yu-Wei, R. Zeying, C.T.-C. Nguyen, "Bridged micromechanical filters," *Proceedings of the IEEE International Frequency Control Symposium and Exposition*, pp. 280-286, 23-27, Aug. 2004.
- [81] R. Aigner, S. Marksteiner, L. Elbrecht, W. Nessler, "RF-filters in mobile phone applications," *Tech. Digest TRANSDUCERS'03 Conference*, pp. 891 – 894, 2003.
- [82] K. M. Lakin, "Coupled resonator filters," *Proceedings. IEEE Ultrasonics Symposium*, vol.1, pp. 901-908, 8-11 Oct. 2002.
- [83] A. Ballato, T. Lukaszek, "A novel frequency selective device: the stacked-crystal filter,"" *27th Annual Symposium on Frequency Control*. pp. 262-276, 1973.
- [84] W. D. Beaver, "Theory and design of the monolithic crystal filter," *21st Annual Symposium on Frequency Control*, pp. 179-199, 1967.
- [85] R. G. Kinsman, "A history of crystal filters," *Proceedings of the 1998 IEEE International Frequency Control Symposium*, pp.563-570, 27-29 May 1998.

- 
- [86] Wang Kun, C.T.-C. Nguyen, "High-order medium frequency micromechanical electronic filters," *Journal of Microelectromechanical Systems*, vol.8, no.4, pp.534-556, Dec 1999.
- [87] M. Onoe, H. Jumonji, N. Kobori, "High frequency crystal filters employing multiple mode resonators vibrating in trapped energy modes," *20th Annual Symposium on Frequency Control*, pp. 266-287, 1966.
- [88] L. Dworsky, "An improved circuit model for monolithic crystal filters," *IEEE Transactions on Sonics and Ultrasonics*, vol.28, no.4, pp. 283-284, Jul 1981.
- [89] T. Uemura, et al., "Low loss diamond SAW devices by small grain size poly-crystalline diamond," *Proceedings Ultrasonics Symposium*, vol.1, pp. 431- 434, 2002.
- [90] J. Wang, J. Butler, T. Feygelson, C.T.-C. Nguyen, "1.51-GHz nanocrystalline diamond micromechanical disk resonator with material-mismatched isolating support," *International Conference on Micro Electro Mechanical Systems (MEMS'04)*, pp. 641- 644, 2004.
- [91] K. M. Lakin, K. T. McCarron, J. F. McDonald, and J. Belsick, "Temperature coefficient and ageing of BAW composite materials", *Proc. Freq. Contr. Symp.*, pp. 605–608, 2001.
- [92] G. Piazza, P. J. Stephanou, J. M. Porter, M. B. J. Wijesundara, A. P. Pisano, "Low motional resistance ring-shaped contour-mode aluminum nitride piezoelectric micromechanical resonators for UHF applications," *International Conference on Micro Electro Mechanical Systems (MEMS'05)*, pp. 20-23, 2005.
- [93] C. Lu, *Application of piezoelectric quartz crystal microbalances*, Elsevier, London, 1984.
- [94] F. M. Battiston, et al., "A chemical sensor based on a microfabricated cantilever array with simultaneous resonance-frequency and bending readout", *Sensors and Actuators B*, vol. 77, pp. 122-131, 2001.
- [95] R. Gabl, et al., "Novel integrated FBAR sensors: a universal technology platform for bio- and gas-detection", *Proc. IEEE Sensors Conf.*, vol. 2, pp. 1184 – 1188, 2003.
- [96] J. R. Vig and F. L. Walls, "A review of sensor sensitivity and stability", *Proc. of IEEE Int. Freq. Cont. Symp.*, pp. 30-33, 2000.

- 
- [97] Z. Hao, R. Abdolvand and F. Ayazi, "A high-Q length-extensional bulk-mode mass sensor with annexed sensing platforms," *Tech. Dig IEEE MEMS06 Conf.*, pp. 598-601, 2006.
- [98] F. S. Hickernell, "ZnO processing for bulk- and surface-wave devices," *Ultrasonics Symposium*, pp. 785- 794, 1980.
- [99] J. B. Lee, S. H. Kwak, H. J. Kim, "Effects of surface roughness of substrates on the *c*-axis preferred orientation of ZnO films deposited by r.f. magnetron sputtering," *Thin Solid Films*, vol. 423, issue 2, pp. 262-266, Jan. 2003.
- [100] P. Inacio, J. N. Marat-Mendes, C. J. Dias, "Development of a biosensor based on a piezoelectric film," *Proceedings. 11th International Symposium on Electrets (ISE 11)*, pp. 287-290, 2002.
- [101] T. Tao, J. S. Ro, J. Melngailis, Z. Xue, and H. D. Kaesz, "Focused ion beam induced deposition of platinum," *J. Vac. Sci. Technol. B* 8, pp. 1826-1829, 1990.

---

## VITA

Reza Abdolvand received his B.S. and M.S. degrees in electrical engineering from Sharif University of Technology, Tehran, Iran, in 1999 and 2001, respectively. He then joined the Georgia Institute of Technology, Atlanta, GA, in 2002, where he received his Ph.D. degree in the School of Electrical and Computer Engineering in 2008. He is now with the School of Electrical and Computer Engineering at Oklahoma State University as an assistant professor starting from Fall 2007. His research interests lie in the area of micro/nano-electromechanical systems with a special focus on design, fabrication, and characterization of integrated micro-resonators with applications in RF circuits and resonant sensors as well as high performance motion sensor design and fabrication.